UNIVERSITÀ DEGLI STUDI DI PARMA

*Ph.D. in Science and Technology of Innovative Materials*

XXVIII Cycle (2013-2015)

# Study of interaction between Si(O,C)Nanowires and Biological System

Supervisor: **Dr. Salvatore Iannotta**

Tutor: **Dr. Giancarlo Salviati**

Coordinator: **Prof. Enrico Dalcanale**

**Paola Lagonegro**

2016

UNIVERSITÀ DEGLI STUDI DI PARMA


**Istituto dei Materiali per l' Elettronica ed il Magnetismo**

***Ph.D. in Science and Technology of Innovative Materials***

XXVIII Cycle (2013-2015)

# Study of interaction between Si(O,C) Nanowires and Biological System

*Paola Lagonegro*

*2016*

Coordinator: **Prof. Enrico Dalcanale**

Supervisor: **Dr. Salvatore Iannotta**

Tutor: **Dr. Giancarlo Salviati**

Author: **Paola Lagonegro**

# Contents

# Abstract

Nanomedicine is a new branch of medicine, based on the potentiality and intrinsic properties of nanomaterials. Indeed, the nanomaterials ( i.e. the materials with nano and under micron size) can be suitable to different applications in biomedicine. The nanostructures can be used by taking advantage of their properties (for example superparamagnetic nanoparticles) or functionalized to deliver the drug in a specific target, thanks the ability to cross biological barriers. The size and the shape of 1D-nanostructures (nanotubes and nanowires) have an important role on the cell fate: their morphology plays a key role on the interaction between nanostructure and the biological system. For this reason the 1D nanostructure are interesting for their ability to mime the biological system. An implantable material or device must therefore integrate with the surrounding extracellular matrix (ECM), a complex network of proteins with structural and signaling properties. Innovative techniques allow the generation of complex surface patterns that can resemble the structure of the ECM, such as 1D nanostructures.

NWs based on cubic silicon carbide (3C-SiC), either bare (3C-SiC NWs) or surrounded by an amorphous shell (3C-SiC/SiO2 core/shell NWs), and silicon oxycarbide nanowires (SiOxCy NWs) can meet the chemical, mechanical and electrical requirements for tissue engineering and have a strong potential to pave the way for the development of a novel generation of implantable nano-devices.

Silicon oxycarbide shows promising physical and chemical properties as elastic modulus, bending strength and hardness, chemical durability superior to conventional silicate glasses in aggressive environments and high temperature

stability up to 1300 °C. Moreover, it can easily be engineered through functionalization and decoration with macro-molecules and nanoparticles.

Silicon carbide has been extensively studied for applications in harsh conditions, as chemical environment, high electric field and high and low temperature, owing to its high hardness, high thermal conductivity, chemical inertness and high electron mobility. Also, its cubic polytype (3C) is highly biocompatible and hemocompatible, and some prototypes of biomedical applications and biomedical devices have been already realized starting from 3C-SiC thin films.

Cubic SiC-based NWs can be used as a biomimetic biomaterial, providing a robust and novel biocompatible biological interface . We cultured in vitro A549 human lung adenocarcinoma epithelial cells and L929 murine fibroblast cells over core/shell SiC/SiO2, SiOxCy and bare 3C-SiC nanowire platforms, and analysed the cytotoxicity, by indirect and direct contact tests, the cell adhesion, and the cell proliferation. These studies showed that all the nanowires are biocompatible according to ISO 10993 standards. We evaluated the blood compatibility through the interaction of the nanowires with platelet rich plasma. The adhesion and activation of platelets on the nanowire bundles, assessed via SEM imaging and soluble P-selectin quantification, indicated that a higher platelet activation is induced by the core/shell structures compared to the bare ones. Further, platelet activation is higher with 3C-SiC/$SiO_2$ NWs and $SiO_xC_y$NWs, which therefore appear suitable in view of possible tissue regeneration. On the contrary, bare 3C-SiC NWs show a lower platelet activation and are therefore promising in view of implantable bioelectronics devices, as cardiovascular implantable devices.

The NWs properties are suitable to allow the design of a novel subretinal Micro Device (MD). This devices is based on Si NWs and PEDOT:PSS, though the well know principle of the hybrid ordered bulk heterojunction (OBHJ). The aim is to

develop a device based on a well-established photovoltaic technology and to adapt this know-how to the prosthetic field. The hybrid OBHJ allows to form a radial p–n junction on a nanowire/organic structure. In addition, the nanowires increase the light absorption by means of light scattering effects: a nanowires based p-n junction increases the light absorption up to the 80%, as previously demonstrated, overcoming the Shockley-Queisser limit of 30 % of a bulk p-n junction.

Another interesting employment of these NWs is to design of a SiC based epicardial-interacting patch based on teflon that include SiC nanowires. . Such contact patch can bridge the electric conduction across the cardiac infarct as nanowires can 'sense' the direction of the wavefront propagation on the survival cardiac tissue and transmit it to the downstream surivived regions without discontinuity. The SiC NWs are tested in terms of toxicology, biocompatibility and conductance among cardiomyocytes and myofibroblasts.

# CHAPTER 1

# Nanomedicine

## 1.1 What is nanomedicine?

The term nanomedicine finds its roots in the first years of the '90s [1] but, according to the Science Citation Index (Institute for Scientific Information, Thompson, Philadelphia, PA, USA), the term appeared only in the year 2000.

Some experts define nanomedicine very broadly as a technology that uses molecular tools and knowledge of the human body for medical diagnosis and treatment. Others, instead, prefer to focus on the original word meaning "nanomedicine" as one technique that makes use of physical effects occurring only in nanoscale objects and that exist at the interface between the molecular and macroscopic world, in which quantum mechanics still reigns. We prefer the second definition.

In detail, nanomedicine is the use of nanostructured or nanometric materials in medicine that, according to their structure, have a unique medical effects as the ability to cross biological barriers or the passive targeting of tissues. Such medical effects are not strictly limited to a size range below or close to 100 nanometers, because the same effect are verify in the structures and objects near micrometer size.[2]

Nanomedicine was born as a connection between different fields, such as bio-engineering, nanotechnologies, biotechnology and medicine, in order to find new applications. In this chapter we will report the more important

applications in nanomedicine.

The European Science Foundation (ESF) launched its forward vision on nanomedicine and provided a new definition: “Nanomedicine uses nano-sized tools for the diagnosis, prevention and treatment of disease and to gain increased understanding of the underlying complex patho-physiology of the disease. The ultimate goal is to improve the quality of human life”.

### 1.2 History of nanomedicine

The concept of nanomedicine arose with Richard Feynman, in 1959. Feyman suggested that the future of humans will be fully occupied by machines, small machines will be used to make further smaller machines, and these in turn, will be used to make even tinier machines, all the way down to the atomic level.[3]The Feynman idea, presented in the lecture, “Plenty of Room at the Bottom” in 1959, entered popular imagination in form to “nanobot” i.e. a robot vessel on the nano- or micro- scale, able to navigate through a patient’s bloodstream and effect cell-by-cell repairs. Even if, this idea is impossible or impracticable, in some measure, this vision lays the foundation of nanotechnology

Another important step of the "relationship" between biology and nanotechnology comes from the observation made by Eric Drexler in 1981. He declared that cell biology offers an existence proof and feasibility of nanotechnology. In fact, cell biology can be regarded as a source of components to be reassembled in synthetic or partially synthetic contexts, or as a source of inspiration by providing models that can be emulated using synthetic materials.

The most important impact on the study of nanotechnology in life sciences has been the use of new tools for investigating the nanoscale. Techniques such as

electron microscopes, since their introduction in the 1980s, allowed to study the properties of individual molecules and assemblies of biomolecules in conditions close to those found in nature. This has permitted the quantitative analysis of the mode of operation of biological machines such as molecular motors and ribosomes, as part of the new field of single molecule biophysics.

Nanomedicine started to grow in 2000: hybrid constructions, involving biological molecular machines integrated with artificial nanostructures (for example the “nano-propellers” produced by Carlo Montemagno), powered by the biological rotary motor F1-ATPase or applications for various schemes for artificial photosynthesis, which similarly combine functioning biological sub-cellular systems in synthetic constructs.

Nadrian Seeman, who has demonstrated the principle in 1989, had the idea of using DNA synthesised to a prescribed sequence as a building material. The idea was based onto quite complex nanoscale structures, exploiting the precise rules of base-pairing to design desired self-assembly characteristics. For many years this found no great interest in the scientific field but in the last ten years Seeman's idea, sustained by a series of new developments and facilitated by technical advances in the synthesis of DNA, allowed to greatly reduced the cost and increased the available quantities of the material. These developments showed that DNA can be used as the basis not just of nanoscale structures, but also of functional devices.

Currently several nano-products are already available for medical use. Some first generation nanomedicine device. Include Abraxane(approved by the FDA in 2005), an anticancer drug formulated as a nanoparticle, Caelyx/Doxil (approved by the FDA in 1995) another anticancer drug encapsulated in liposomes containers made from self-assembled lipid bilayers, and Cimzia (approved in 2008 by the FDA for Crohns disease, and in 2009 by the EMEA for arthritis) an antibody attached to a synthetic polymer molecule. Unfortunately

these are isolated cases, and the issues to use these product in clinic use are higher when one considers the potential therapeutic use of nucleic acids, for example, DNA fragments in gene therapy, or small RNA fragments such as siRNA (small interfering RNA). Nanomedicine has the potential to revolutionize medicine and, in this moment, absolutely needs new regulatory guideline from scientific communities.

### 1.3 Applications of nanotechnology for healthcare

Recently nanomedicine is focused on a broad range of applications and, going hand in hand with new technology and new nanomaterials, finds new fields of employment (figure 1). In this paragraph the main applications field of nanomedicine are summarized.

Drug delivery: the drug delivery technique is based on nanoscale particles/molecules that have been developed to target specific sites in the body, to improve the bioavailability and pharmacokinetics of therapeutics. Multifunctional targeted devices are capable of bypassing biological barriers to deliver multiple therapeutic agents directly to the cells and also to tissues in the microenvironment.[4]

Therapy techniques: several nanostructure themselves have unique medical properties, which show therapeutic effects in biological systems.[5]These properties can be exploited in therapeutic treatments. Indeed, several nanostructures have intrinsic properties or can be enriched with bioactive agents and can be useful to treat specific systems, for example magnetic nanoparticle or photodynamic therapy used to the cancer treatment[6].

Imaging*:* nanoparticles can be used to mark biological structure, NPs are used particularly for MRI and ultrasound scans, provide an improved contrast and favorable biodistribution. For example, superparamagnetic iron oxide

nanoparticles have been used as MRI contrast agents.[7]

Cell and Tissue Repair and replacement: damaged tissues and organs often need to be replaced by artificial substitutes. Nanotechnology offers a range of new biocompatible coatings for the implants that improves their adhesion, durability and lifespan or as a scaffold. New types of nanomaterials are being evaluated to improve interface properties for tissue replacement and regeneration. For example, nanopolymers can be used to coat devices in contact with blood (e.g. artificial hearts, catheters) to disperse clots or prevent their formation.[8]

Implantable devices*:* Nanomaterials have the capability to improve device properties or can be used to develop a new generation of electrical bio-devices, smaller and more efficient.[9]

Nanotechnology is being used to develop a potentially more powerful device to restore lost vision and hearing. One approach uses a miniature video camera attached to glasses to capture visual signals which are then transmitted to an array of electrodes placed in the eye. Another approach uses an array of electrodes at the tip of the device to solve hearing problems, with five times greater amplification than that of current devices[10]

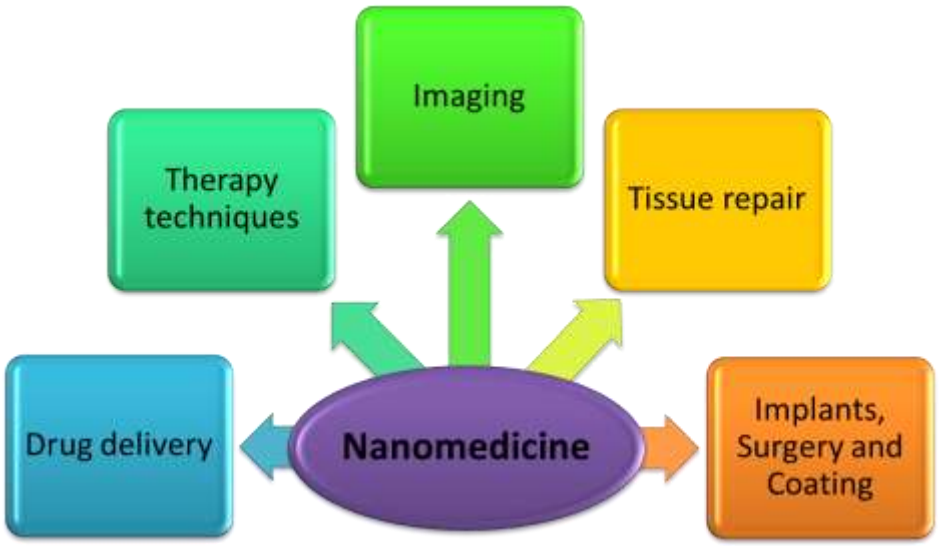


*Fig. 1: Scheme on the different applications in nanomedicine.*

**1.4 Nanowires in nanomedicine**

Several nanostructures, with different shape and dimensionality (0D: nanoparticles, 1D: nanotubes and nanowires, 2D: nanosheets) and materials, are employed in the nanotechnology. These characteristics play an important role on the cell fate. The nanostructure size and shape is the key of the interaction between nanostructure and the biological system and one dimension nanostructures find a large purpose in this field.

1D nanostructure are interesting because mime the biological system. An implantable material or device must therefore integrate with the surrounding extracellular matrix (ECM), a complex network of proteins with structural and signaling properties. Innovative techniques allow the generation of complex surface patterns that can resemble the structure of the ECM, such as 1D nanostructure.

Limiting the field of interest only to the nanotubes and nanowires in their

different chemical formulations and functionalization, several nanosystems are being studied, such as carbon nanotubes (single-walled [11] and multi-walled) graphene, metal nanowires (e.g. based on gold [12], iron oxide nanoparticles iron[13] and silver [14]) semiconducting nanowires (e.g. based on InAs[15]), and oxide nanowires (e.g. based on ZnO[16] and $TiO_2$[17], [18]). These differ considerably from both the compositional and the structural point of view, and therefore, for each kind of nanowire, the effect that it induces on cell behavior must be carefully studied.

It was demonstrated that $TiO_2$-based nanofilaments had a strong dose-dependent effect on cell proliferation and cell death [18]and $TiO_2$ nanowires induced persistent pathologic alterations in the lung tissue in mice[17]. ZnO nanowires resulted in vitro cytotoxic for human monocyte macrophages[16], and the cell viability resulted decreased on ZnO nanorods for NIH3T3 fibroblasts, human umbilical vein endothelial cells [19] and mouse macrophages[16]

Metal nanowires on the contrary proved as essentially cytocompatible. A significant antimicrobial activity of silver nanowires has been reported, against a no significant cytotoxic response [20] and a autophagy induction [21]. These results highlight that Ag nanowires are definitely different from Ag nanoparticles, which are very toxic, because of the oxidation to Ag+ salts, that have been recognized as intrinsically toxic. Iron nanowires or iron oxide based nanowires, as useful magnetic nanomaterials, may also be a good candidates for several biomedical applications due to their very low cytotoxicity in vitro[13].

The greatest research efforts have been devoted to carbon nanotubes, that can be either single-walled (SWCNTs) or multi-walled (MWCNTs). They present different structural properties due to the their different electron arrangement and a wide range of applications for therapeutic and diagnostic purposes.

Numerous studies have been performed to evaluate the effects of CNT on cells and whole body, but their toxicity is not jet well understood because of contradicting results[22]. A review focused on safety and toxicology of carbon nanotubes highlighted the role of CNT dimension, surface properties, bio-durability and corona formation as determinant factors of CNT toxicity. Recently, it was reported in literature that the potential surface degradation product, MWCNT, did not induce toxic responses on human bone marrow stromal cells, but the combination of MWCNT with lactic acid, resembling release after bulk degradation, significantly inhibited HBMC proliferation and activity. This evidence demonstrates the importance of comprehensive evaluations of novel materials for medical applications in predicting possible adverse effects during nanocomposite degradation.[23]Another study reported that MWCNT induces cytotoxicity in adenocarcinomic alveolar basal epithelial (A549) cells only at relatively high concentrations and longer exposure time. Within a relatively low dosage range (30 μg/ml) and short time period (24 h), MWCNT treatment did not induce significant cytotoxicity, cell cycle changes, apoptosis, or DNA damage [24].

The most advanced results on the NWs biocompatibility have been obtained from Si-based nanosystems, which recently showed a stability of about two weeks in biological environments:, in this thesis the biocompatibility of these class of NWs will be shown.

| **1D Nanostructure** | | **Cytotoxicity Results** |
|---|---|---|
| **Carbon nanotubes** | SWCNT and MWCNT (*Single and Multi-Walled Carbon NanoTube)* | They are toward clinical translation even if sometimes show controversial results [22] |

| | | |
|---|---|---|
| **Metal nanowires** | Gold(Au),Iron(Fe), Silver(Ag) | Contrary to nanoparticles proved to be essentially cytocompatible.[25] |
| **Semiconducting Nanowires** | Silicon-based NWs(Si, SiC(silicon carbide) ) | The most advanced results on the NWs biocompatibility have been obtained from Si-based nanosystems which recently showed a stability of about two weeks in biological environments[26] |
| | other III−V NWs | controversial results. |
| **Oxide nanowires** | ZnO(zinco-oxide), $TiO_2$titanio-oxide | controversial results.[27] |
| | $SiO_2$(silicon-oxide) | Citocompatible |

*Tab.1: Brief summary on the 1D nanostracture used in medicine and its cytotoxicity results referred on letterature .*

## 1.5 Thesis Outline

The aim of this thesis is evaluate how and if the Si(O,C) NWs are suitable to new applications in nanomedicine. To better understand the focus of this thesis the first chapter tries to define the concept of nanomedicine, its history and applications, with a particular emphasis on 1D nanostructure in biomedical applications. In the Chapter 2 the methods to the growth and characterization of Si-based NWs will be shown. The chapter 3 will be focused on the cytocompatibility and blood interaction of the nanostructure described in the second chapter, in view of future application. This concludes the first section of the thesis, with thepurpose to introducing two applications in bioengineering field.

The second section opens with the first application as Subretinal Micro Device(sMD), based on ordered bulk heterojunction (consolidated photovoltaic configuration), Si NWs and PEDOT:PSS The chapter 5 will discuss the use of SiCNws as a biocompatible connection for cardiac tissue,will show the basic idea and the preliminary in vitro results.

Finally the last chapter (chapter 6) will resume the final considerations on this thesis and will discuss the future perspectives of this new generation of materials.

**Bibliography**


[1] E. D. and C. Peterson, *Unbounding the future-The Nanotechnology Revolution*. 1991.

[2] V. Wagner, A. Dullaart, A.-K. Bock, and A. Zweck, "The emerging nanomedicine landscape.," *Nat. Biotechnol.*, vol. 24, no. 10, pp. 1211–7, Oct. 2006.

[3] A. Kumar, F. Chen, A. Mozhi, X. Zhang, Y. Zhao, X. Xue, Y. Hao, X. Zhang, P. C. Wang, and X.-J. Liang, "Innovative pharmaceutical development based on unique properties of nanoscale delivery formulation.," *Nanoscale*, vol. 5, no. 18, pp. 8307–25, Sep. 2013.

[4] J. Evans, "Five big ideas for nanotechnology.," *Nat. Med.*, vol. 15, no. 4, p. 348, Apr. 2009.

[5] V. Sanna, N. Pala, and M. Sechi, "Targeted therapy using nanotechnology: focus on cancer.," *Int. J. Nanomedicine*, vol. 9, pp. 467–83, Jan. 2014.

[6] F. Rossi, E. Bedogni, F. Bigi, T. Rimoldi, L. Cristofolini, S. Pinelli, R. Alinovi, and M. Negri, "Porphyrin conjugated SiC/SiOx nanowires for X-ray-excited photodynamic therapy," *Sci. Rep.*, pp. 1–6, 2015.

[7] L. K. Bogart, G. Pourroy, C. J. Murphy, V. Puntes, T. Pellegrino, D. Rosenblum, D. Peer, and R. Lévy, "Nanoparticles for imaging, sensing, and therapeutic intervention.," *ACS Nano*, vol. 8, no. 4, pp. 3107–22, Apr. 2014.

[8] M. J. Dalby and M. J. Biggs, "Special focus on nanoscale regeneration," Mar. 2015.

[9] F. PATOLSKY and C. LIEBER, "Nanowire nanosensors," *Mater. Today*, vol. 8, no. 4, pp. 20–28, 2005.

[10] L. Bareket-Keren and Y. Hanein, "Carbon nanotube-based multi electrode arrays for neuronal interfacing: progress and prospects.," *Front. Neural Circuits*, vol. 6, p. 122, Jan. 2012.

[11] N. W. S. Kam, Z. Liu, and H. Dai, "Functionalization of Carbon Nanotubes via Cleavable Disulfide Bonds for Efficient Intracellular Delivery of siRNA and Potent Gene Silencing," *J. Am. Chem. Soc.*, vol. 127, no. 36, pp. 12492–12493, Sep. 2005.

[12] M. Li, T. Yin, Y. Wang, F. Du, X. Zou, H. Gregersen, and G. Wang, "Study of biocompatibility of medical grade high nitrogen nickel-free austenitic stainless steel in vitro.," *Mater. Sci. Eng. C. Mater. Biol. Appl.*, vol. 43, pp. 641–8, Oct. 2014.

[13] M.-M. Song, W.-J. Song, H. Bi, J. Wang, W.-L. Wu, J. Sun, and M. Yu, "Cytotoxicity and cellular uptake of iron nanowires.," *Biomaterials*, vol. 31, no. 7, pp. 1509–17, Mar. 2010.

[14] A. Schinwald, T. Chernova, and K. Donaldson, "Use of silver nanowires

to determine thresholds for fibre length-dependent pulmonary inflammation and inhibition of macrophage migration in vitro," *Part. Fibre Toxicol.*, vol. 9, no. 1, p. 47, Jan. 2012.

[15] T. Berthing, S. Bonde, C. B. Sørensen, P. Utko, J. Nygård, and K. L. Martinez, "Intact mammalian cell function on semiconductor nanowire arrays: new perspectives for cell-based biosensing.," *Small*, vol. 7, no. 5, pp. 640–7, Mar. 2011.

[16] K. H. Müller, J. Kulkarni, M. Motskin, A. Goode, P. Winship, J. N. Skepper, M. P. Ryan, and A. E. Porter, "pH-Dependent Toxicity of High Aspect Ratio ZnO Nanowires in Macrophages Due to Intracellular Dissolution," *ACS Nano*, vol. 4, no. 11, pp. 6767–6779, Nov. 2010.

[17] E.-J. Park, G.-H. Lee, H.-W. Shim, J.-H. Kim, M.-H. Cho, and D.-W. Kim, "Comparison of toxicity of different nanorod-type TiO2 polymorphs in vivo and in vitro.," *J. Appl. Toxicol.*, vol. 34, no. 4, pp. 357–66, Apr. 2014.

[18] A. Magrez, L. Horváth, R. Smajda, V. Salicio, N. Pasquier, L. Forró, and B. Schwaller, "Cellular toxicity of TiO2-based nanofilaments.," *ACS Nano*, vol. 3, no. 8, pp. 2274–80, Aug. 2009.

[19] J. Lee, B. S. Kang, B. Hicks, T. F. Chancellor Jr., B. H. Chu, H.-T. Wang, B. G. Keselowsky, F. Ren, and T. P. Lele, "The control of cell adhesion and viability by zinc oxide nanorods," *Biomaterials*, vol. 29, no. 27, pp. 3743–3749, Sep. 2008.

[20] N. E. A. El-Gamel, "Silver(i) complexes as precursors to produce silver nanowires: structure characterization, antimicrobial activity and cell viability," *Dalt. Trans.*, vol. 42, no. 27, p. 9884, Jul. 2013.

[21] N. K. Verma, J. Conroy, P. E. Lyons, J. Coleman, M. P. O'Sullivan, H. Kornfeld, D. Kelleher, and Y. Volkov, "Autophagy induction by silver nanowires: A new aspect in the biocompatibility assessment of nanocomposite thin films," *Toxicol. Appl. Pharmacol.*, vol. 264, no. 3, pp. 451–461, Nov. 2012.

[22] Y. Zhang, S. F. Ali, E. Dervishi, Y. Xu, Z. Li, D. Casciano, and A. S. Biris, "Cytotoxicity effects of graphene and single-wall carbon nanotubes in neural phaeochromocytoma-derived PC12 cells.," *ACS Nano*, vol. 4, no. 6, pp. 3181–6, Jun. 2010.

[23] M. Obarzanek-Fojt, Y. Elbs-Glatz, E. Lizundia, L. Diener, J.-R. Sarasua, and A. Bruinink, "From implantation to degradation - are poly (l-lactide)/multiwall carbon nanotube composite materials really cytocompatible?," *Nanomedicine*, vol. 10, no. 5, pp. 1041–51, Jul. 2014.

[24] L. Zhou, W. Li, Z. Chen, E. Ju, J. Ren, and X. Qu, "Growth of hydrophilic CuS nanowires via DNA-mediated self-assembly process and their use in fabricating smart hybrid films for adjustable chemical release.," *Chemistry*, vol. 21, no. 7, pp. 2930–5, Feb. 2015.

[25] S. Centi, F. Tatini, F. Ratto, A. Gnerucci, R. Mercatelli, G. Romano, I.

Landini, S. Nobili, A. Ravalli, G. Marrazza, E. Mini, F. Fusi, and R. Pini, “In vitro assessment of antibody-conjugated gold nanorods for systemic injections.,” *J. Nanobiotechnology*, vol. 12, p. 55, Jan. 2014.

[26] A. Cacchioli, F. Ravanetti, R. Alinovi, S. Pinelli, F. Rossi, M. Negri, E. Bedogni, M. Campanini, M. Galetti, M. Goldoni, P. Lagonegro, R. Alfieri, F. Bigi, and G. Salviati, “Cytocompatibility and cellular internalization mechanisms of SiC/SiO 2 nanowires,” *Nano Lett.*, vol. 14, no. 8, pp. 4368–4375, 2014.

[27] R. J. Vandebriel and W. H. De Jong, “A review of mammalian toxicity of ZnO nanoparticles.,” *Nanotechnol. Sci. Appl.*, vol. 5, pp. 61–71, Jan. 2012.

# CHAPTER 2

# Nanowires: Growth and Characterization

Nanostructured materials, nanowires (NWs) in particular, spurred a strong research for the design and fabrication of nano-scale devices. This exciting and up-and-coming research area crosses different fields, from nanoelectronic devices (e.g. nano field-effect transistors) to nanophotonics.

The vapor–liquid–solid method (VLS) is a process to growth of one-dimensional structures, such as nanowires, by chemical vapor deposition(CVD). In the VLS mechanism the NWs growth through direct adsorption of a gas phase on to a solid surface.

Cubic silicon carbide (β-SiC or 3C-SiC) is a wide band-gap semiconductor with high hardness, high electron mobility, high thermal conductivity and high resistance to chemical attacks. These properties make of SiC NWs one of the most attractive candidates for devices operating in harsh environments such as nano-electromechanical systems and nano-sensors exploiting the SiC NWs as biocompatible nanoprobes for biological systems. In this chapter the growth, the properties and the characterization of SiC-based NWs and Si-based NWs will be showed.

## 2.1 Introduction

In last 10 years, the materials science developed new nanotechnologies, new materials and new growth methods.

The interest in nanomaterials is due to the fact that they have superior properties compared to the respective bulks. These properties allows to realize nano devices with better performance in many fields of applications.

Nanowires (NWs) open promising near-future perspectives for the design and fabrication of nano-scale devices. The main interests are in nanoelectronic devices (e.g. nano field-effect transistors), nano-electromechanical systems able to operate even in harsh environments, nano-sensors, nanomedicine and nano-probes for biological systems.

A Nanowire refers to a 1D structure with two dimensions in the nanometer range and the third (length) in the micron one. A nanowire can have characteristics radically different from the massive material counterpart, subsequently to the very high surface / volume ratio and, below certain critical dimensions, due to quantum confinement effect.

Recently, at IMEM-CNR, methods to prepare semiconducting nanostructures (nanowires) by Chemical Vapor Deposition (CVD) and Vapour Phase Epitaxy (VPE) [1,2] have been developed. The above methods exploit the Vapour Liquid Solid (VLS) mechanism, a catalytic liquid alloy phase on a substrate that rapidly adsorbs a vapor and reaches supersaturation, with the consequent formation of a crystal at the liquid–solid interface.

Nanowires can be produced with different methods, either through conventional subtractive nanofabrication processes, through additive nanomaterial growth methods or via lithography and etching. These processes can be divided in “top-down” and “bottom up” approach.

A bottom up synthesis method means that the nanostructures are synthesized

onto the substrate by stacking atoms onto each other, which gives rise to crystal planes, crystal planes further stack onto each other, resulting in the synthesis of the nanostructures.

In the top-down approach the fabrication involves sculpting or etching out crystal planes (removing crystal planes), to carve nanostructures and devices from a larger piece of material.

The NWs dimensions depend on both the material which reacts in a certain way to the effect of etching action on the materials but also by the resolution of the lithographic process. Ranging from the photolithography, main techniques used for mass production in the semiconductor industry are the electron beam lithography (EBL), flexibility and mask-less nature, very high (sub-10 nm) resolution.

In this chapter I focus on nanowires produced through "bottom-up" growth methods, in particular, the catalyst-mediated vapor–liquid–solid (VLS) process. This chapter will focuses on describing the research on the formation of silicon based semiconductor nanowires and some metal oxide nanowires

### 2.1.1 Nanowires History

Interest in nanowires was largely driven by the successful growths of 10 nm scale nanowires exploiting the VLS mechanism in the late 1990s. The history of nanometer scale nanowires is relatively recent: the first experimental demonstrations, in 1998 by Morales *et al.,*[3] employed laser ablation to generate the source vapor needed for VLS growth to obtain single-crystalline Si and Ge nanowires. Very soon the process was applied to more controllable methods such as CVD with VLS, which has become the dominant option for nanowire growth due to its simple realization and flexible and excellent control over many aspects of the synthesis process.

The history of VLS growth can be traced back to the 1960s, when Wagner[3] successfully employed this method to grow silicon microwires (whiskers), with a large size (>0.1 μm in diameter). The whiskers provided the first evidence that it was possible to scale the dimensions of semiconductors

### 2.1.2 Vapor–liquid–solid (VLS) mechanism

The typical VLS growth process (Figure x) involves the use of a metal catalyst (i.e. Au, Ag, Fe, Ni) on the substrate, obtained either by depositing a thin metal layer or by dispersion of nanoparticles. During the growth process, the metal nanoparticles are first heated up above the eutectic temperature for the target metal–semiconductor system to create a liquid metal–semiconductor eutectic alloy. With the presence of the semiconductor source material in the vapor phase, the eutectic alloy will continue to incorporate the semiconductor material through the vapor/liquid interface, ultimately resulting in supersaturation of the semiconductor material in the eutectic alloy. Further addition of the semiconductor source material into the eutectic alloy will eventually result in a nucleation event whereby the semiconductor material precipitates and creates a liquid/solid interface(Fig. 1), which is also referred to as the growth interface. Nanowire growth is thus achieved *via* the transfer of the semiconductor material from the vapor source at the vapor/liquid interface into the eutectic, followed by continued solid addition at the liquid/solid interface. In this manner, the name VLS growth accurately captures the essence of the growth process from the starting vapor source stage to the final solid crystal stage. Notably, as growth continues, the metal catalyst will remain at the tip as the nanowire elongates below the liquid/solid interface, as schematically illustrated in figure 1 and 2

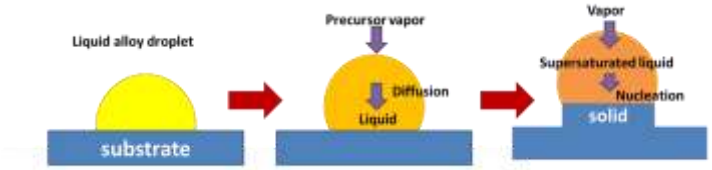


Fig.1 Enlarged view illustrating the three kinetic steps for NW growth: 1)Liquid alloy droplet formation 2) gaseous precursors decomposition at the vapor-liquid interface and diffusion through the alloy droplet 3) NW crystallization by nucleation into a step at the growing liquid-solid interface of the nanowire.

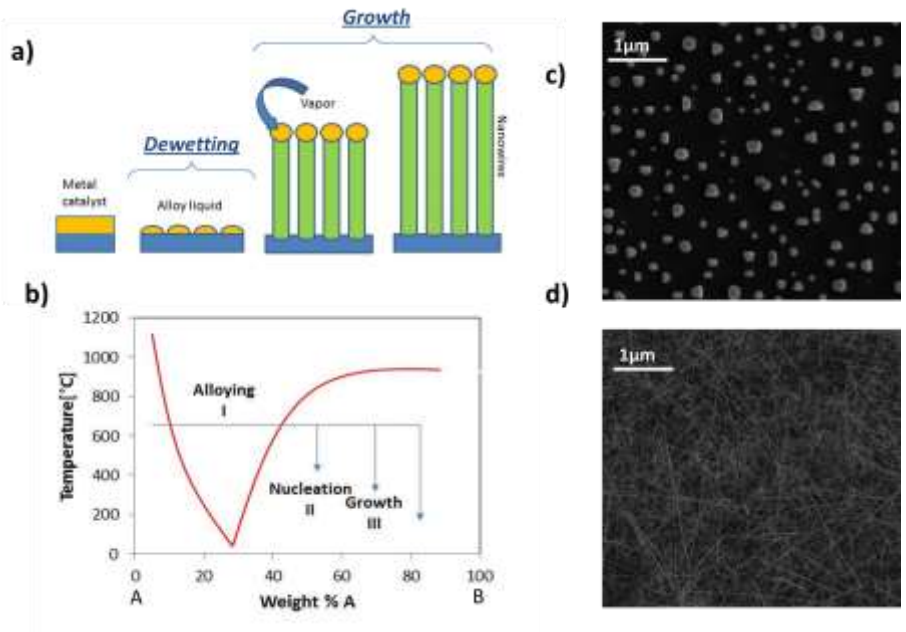


Fig. 2 a)Schematic representation of VLS process b)Binary phase diagrams for Metal-Substrate; line indicates a typical growth temperature. (c) typical SEM image of dewetting (d) typical SEM images of NWs.

The role of the metal is two-fold. Firstly, it is used to form the dewetting, small drops formed by eutectic alloy with the substrate (Fig 1, 2a,c). The sizes of alloy drops define the diameter of a growing nanowire. The eutectic

temperature is much lower than the melting temperature of its compounds, as shown in the figure 2b. Accordingly, the VLS growth of nanowires can be carried out at low-temperature.

Secondly, the metal is used as a catalyst that promotes the diffusion and the nucleation of the semiconductor gaseous precursor (Fig.1), thus selectively producing the semiconductor source material at the targeted growth sites. The use of metals can raise concerns regarding catalyst metal contamination during VLS growth.

VLS nanowire growth is typically performed in a CVD chamber such as hot-wall CVD, lamp-heated cold-wall CVD and metal–organic CVD (MOCVD) systems.

In this system the precursors are introduced in the vapor phase and/or by materials decompositions and nanowire growth take place at controlled temperatures and pressures. The flexibility of the VLS method enabled it to be used for the growth of a broad range of nanowire materials, covering group IV materials such as Si[4], Ge[5], group III–V (i.e. SiC[6], GaAs[7], GaP[8], InP[9]), II–VI materials such as ZnS[10], ZnSe[11], CdS[10], nitrides and oxide such as ZnO[12], $SiO_2$[13]. In the case of compound material nanowires, the semiconductor reactants are usually provided by metal–organic chemical vapor deposition (MOCVD) [11]

At IMEM-CNR, SCALING group has developed the preparation and characterization of semiconducting nanostructures and nanowires by CVD: SiC/$SiO_2$ core/shell, $SiO_xC$, SiC, Si NWs

The follow sections will describe the materials, the growth method and characterization of the nanowires listed above.

## 2.2 Silicon Carbide

The Silicon Carbide is known as a robust, hard material and as a high-temperature semiconductor for advanced applications.

Biomedical, environmental sciences and space exploration boards, are in need of resistant materials. Single-crystal silicon carbide (SiC) presents a high Young's modulus (370 GPa), excellent hardness (9 on the Mohs scale), low friction coefficient (0.17), and high resistance to wear and corrosion that suggests a material resistance in harsh environments such as body fluids[14,15]. For instance, SiC does not react with any known material at room temperature, the only efficient etchant being molten potassium hydroxide (KOH) at temperatures above 400ºC[16]. Moreover, single-crystal SiC is a wide energy band-gap semiconductor with gaps varying from 2.4 to 3.2 eV depending on the polytype. Hence, crystalline SiC merges excellent tribological properties to a vast sensing potentiality.

These features, together with low thermal expansion coefficient, low weight, and transparency to visible light, elevate SiC as a candidate biomaterial that could be used in a wide variety of cutting-edge applications varying from smart medical implants to environmental and space exploration biosensors. Moreover, it could be the platform of choice to investigate cell–semiconductor electronic interactions. Clearly, in many of these bioapplications, the degree of success of a material depends on its biocompatibility and on its capacity of directly interfacing cells. The capability of SiC of integrating with living tissue and safely contacting blood has been largely reported by the biomedical research community. In the cardiovascular field SiC presents a high barrier for protein (and therefore platelet) adhesion and, hence, is thromboresistant and hemocompatible[17][18].

### 2.2.1 Silicon Carbide-Materials Overview

SiC is first and foremost a material that consists of the covalent bonding of Si and C atoms, typically in biatomic layers as shown in Figure 3 . These form tetrahedrally oriented molecules of Si–C, with a very short bond length and, hence, a very high bond strength. This is the origin of the extremely high chemical and mechanical stability of SiC[19].

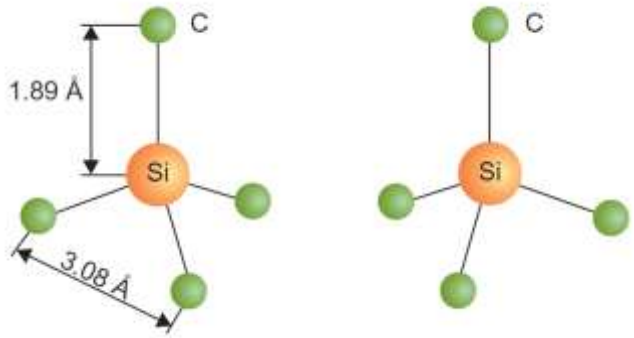


Fig. 3: All SiC crystals are formed via bilayers of C and Si, covalently bonded to form a tetrahedron. Four carbon atoms are covalently bonded with a silicon atom in the center (conversely four Si atoms are covalently bonded with a C atom as this arrangement is crystallographically identical and represents the next atomic layer in the crystal). Two types exist—one is rotated 180° around the c-axis with respect to the other, as shown. This tetrahedrally bonded molecule then forms the basic building block of all SiC materials[18]

SiC can be formed in amorphous, polycrystalline, and monocrystalline solid forms, and because of the high bond strength and high-temperature operating capabilities of SiC, synthesis of SiC materials normally requires high temperatures (>1,000 °C). The material can be grown in bulk (boule) crystal form, currently with diameters up to 150 mm (6 in.), and can be heteroepitaxially grown on Si substrates (details of how this is accomplished are provided in the next chapter).

One of the important characteristics of SiC is that the bilayers of Si and C

(Figure 4) can be stacked one upon the other in different crystal orientations: cubic, hexagonal, and rhombohedral. With more than 200 known polytypes reported in the literature, the three technologically relevant forms are one purely cubic form (β-SiC) and two hexagonal forms that actually have some cubic symmetry (α-SiC). These three polytypes are shown in Figure 5. The cubic form has the designation 3C-SiC, where the "3" delineates that 3 bilayers of Si–C are needed to form the basic structure and the "C" indicates that the crystal form is cubic. The hexagonal forms are 4H-SiC and 6H-SiC, where the "4" and "6" delineate that 4 and 6 bilayers are needed, while the "H" indicates that the crystal form is hexagonal. While interesting in their own right, these various forms of SiC actually have different applications, where the dominant power electronic device crystal of choice is 4H-SiC because of it having the highest bandgap (3.2 eV), while 6H-SiC is ideally suited for solid-state lighting (LEDs), as its lattice constant is close to the GaN family of alloys used in advanced LEDs that have enabled DVD and blue ray technology, not to mention the solid-state lighting revolution that is currently leading to dramatic reductions in power consumption worldwide.

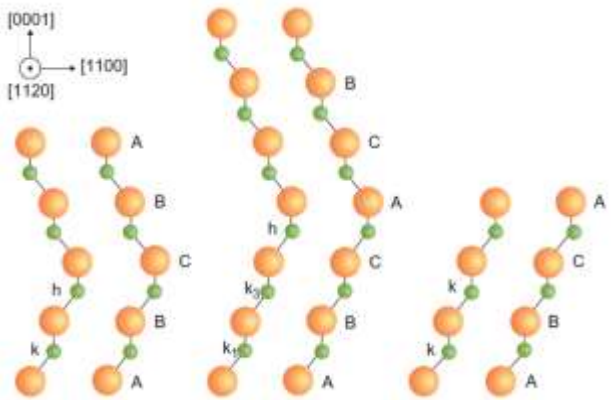


Fig. 4 Atomic stacking sequence of the three technologically relevant SiC polytypes. From left to right, 4H-SiC (ABCB), 6H-SiC (ABCACB), and 3C-SiC (ABC). The letters "k" and "h" denote crystal symmetry points that are cubic and hexagonal, respectively. [18]

Our interest is for the cubic phase because it can be grown on a silicon substrate, which has a cubic structure although with different lattice parameter. In this thesis "SiC" will thus only refer to the cubic phase.

### 2.3 Silicon based NWs and Silicon Carbide based NWs

Many of the produced SiC-based NWs are covered by an oxide layer (core-shell) and some by C-rich phases in the shell, i.e. they consist of a continuous crystalline core encapsulated in a sheath of a different crystalline or amorphous material [20].

However, for many of them, the sheath is a thin native oxide with minor influences on the physical properties and it is often removed during device fabrication.

Silicon carbide, as shown in the previous paragraph, has been extensively studied for application in harsh conditions, as chemical environment, high electric field and high and low temperature, owing to its high hardness, high thermal conductivity, chemical inertness and high electron mobility [21]. Also, its cubic polytype (3C) is highly biocompatible and hemocompatible, and some prototypes for biomedical applications and biomedical devices have been already realized starting from 3C-SiC thin films.[18]

Furthermore, SiC can be easily covered with Silicon oxide($SiO_2$). $SiO_2$ shows promising physical and chemical properties as elastic modulus, bending strength and hardness, chemical durability [22][23][24]. Moreover, it can be easily engineered through functionalization and decoration with macro-molecules and nanoparticles [25][26][27].

SiC shows promising characteristics for blood-contact applications, indeed it inhibits the platelets activation and the clotting formation.[14] Contrarily $SiO_2$

has been shown to be an ideal substrate to increase the aggregation and the activation of platelets, thereby promoting a more rapid clot formation and the acute inflammatory process.[28]

### 2.3.1 Core/Shell (SiC/SiOx) NWs

Core/shell 3C-SiC/$SiO_2$ nanowires are synthesized on silicon substrates <100> in an homemade open tube-CVD reactor using carbon monoxide (CO) as single gaseous precursor and different metals as catalyst [29]. Our process allows the control of the precursor flow and concentration over time, and the growth temperature (usually at 1100°C) can be more precisely tuned, while when using the solid precursor ($WO_3$ and graphite) CO would be released at a fixed temperature (1050°C). The process is metal-assisted. Nickel based compounds (e.g. nickel nitrate ($Ni(NO_3)_2$)) perform as the most effective catalysts, but safety standards for applications in biological environment require to minimize the employment of nickel, which can stimulate neoplastic transformations. Therefore, we recently moved toward iron catalysts (e.g. ferric nitrate ($Fe(NO_3)_3$), more suitable for biomedical applications.

The substrate preparation for the growth is performed in three steps: i) cleaning in ultrasonic bath with organic solvent; ii) etching in hydrofluoric acid (HF, aqueous solution for 120 s) to remove native surface oxide. The sample is then rinsed in deionized water and dried in nitrogen atmosphere; iii) dipping in catalyst solution and drying at 40 °C in air with controlled humidity. To obtain a uniform nanowire growth over an area of at least 10 $cm^2$, it is useful to dissolve the catalysts in ethanol and add a non-ionic surfactant (e.g. oleylamine) to enhance ethanol wetting of the silicon substrate. After the above mentioned preparation protocol, the sample is loaded in the growth chamber of an open-tube CVD system, which is purged with $N_2$ to remove

oxygen. The temperature is risen to about 1100°C and, upon reaching stabilization, CO is introduced with $N_2$ as carrier gas at a concentration of about 4%. The growth lasts for 15-30 minutes, and then the growth chamber is cooled down to room temperature in nitrogen atmosphere. During the heating phase, iron(III) nitrate undergoes a decomposition to iron(III) oxide and a de-wetting takes place, so that the catalyst forms droplets or islands on the substrate surface.

The typical morphology of the NWs over the growth substrate is that of a dense network of long interwoven fibers (see Fig. 5 left). Consistently with the VLS growth, the NW tips are clearly distinguishable and composition-sensitive techniques, as SEM imaging with backscattered electrons and TEM imaging in High-Angle Annular Dark-Field (HAADF) mode, assess the presence of high-Z elements in the tip, which is mainly composed by crystalline iron silicides/silicates. From TEM studies (Fig. 5 right), the NWs are shown to exhibit a core–shell structure, with a crystalline core, univocally identified as 3C-SiC by the crystal symmetry and the lattice spacings, wrapped by an amorphous $SiO_x$ shell, with x slightly lower than or equal to 2. The NW axis defines the growth direction, which corresponds to the <111> direction of 3C-SiC. The occurrence of planar stacking faults in the core along (111) planes and of local stacking sequences typical of 2H, 4H and 6H polytypes is observed, as commonly found in 3C-SiC whiskers.[30] The average core diameter is around 20 nm, while the shell thickness can be tuned from about 20 nm (standard) to about 100 nm depending on the growth conditions.

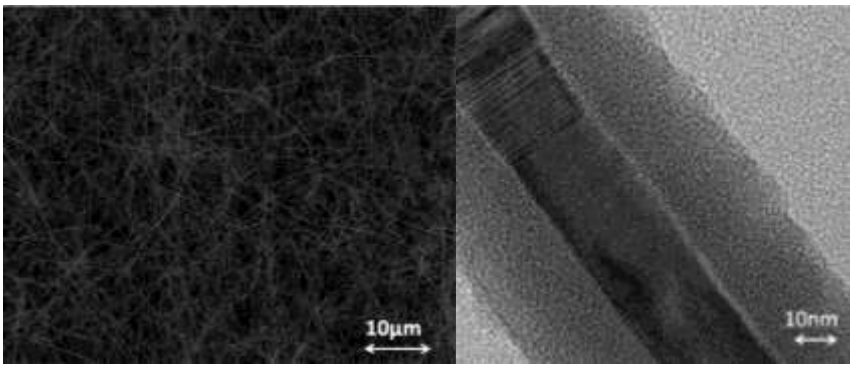


Fig. 5 Left: Typical SEM-image of SiC/SiOx core-shell NWs bundle. Right: Typical TEM image of a single SiC/SiOx NW, showing the planar defects of the SiC crystalline core.

### 2.3.2 Silicon Carbide NWs

The bare 3C-SiC NWs were obtained by chemical etching of the core shell $SiC/SiO_2$ NWs by removing of the shell. It has to be noted that a conventional HF etching does not allow a complete removal of the shell [8]. Therefore, the NWs were chemically etched using a standard RCA clean followed by a second chemical treatment with Piranha solution and final etching (HCl :H2O 2 : 1 and H2O:HF 50 : 1) [31]. The procedure allowed to obtain entirely crystalline SiC NWs with a diameter of about 20 nm(Fig.6 right)

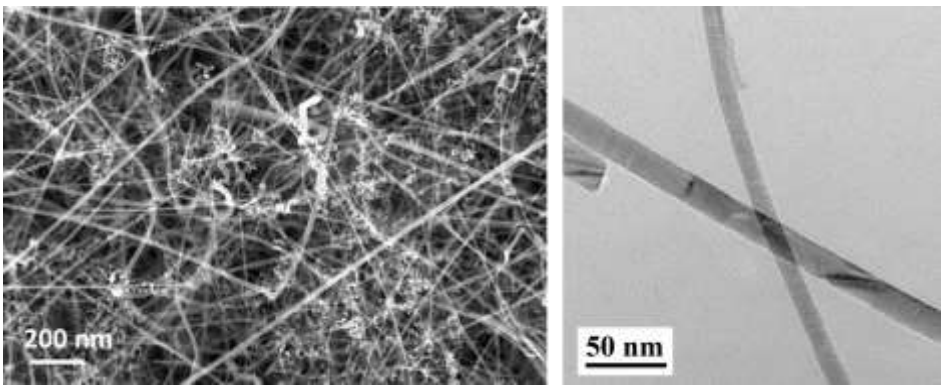


Fig. 6 Left: Typical SEM-image of SiC NWs bundle. Right: Typical TEM image of a single SiC NW, obtained by etching SiC/SiOx NWs.

### 2.3.3 Silicon NWs

Silicon nanowires (SiNWs) (Fig.7) were grown on Si (100) oriented by VPE in a home-made induction heated reactor at low pressure, by using silane($SiH_4$) as precursor, hydrogen as carrier gas and gold as catalyst. Gold catalyst, as previously discussed, forms a eutectic with the silicon at 580°C, thus permitting the VLS mechanism.

The substrate preparation with catalyst is performed in three steps: i) cleaning in ultrasonic bath with organic solvent; ii) etching in hydrofluoric acid (HF, aqueous solution for 120 s) to remove native surface oxide, rinsed in deionized water and dried in nitrogen atmosphere, iii) 2 nm of gold film are deposited by radio frequency (FR) magnetron sputtering.

The substrate is then loaded in the growth chamber, the system is purged with $H_2$ at low pressure to remove ambient air. For the VPE growth, a preheating of the gold-deposited substrate was performed in hydrogen flow in order to get catalyst dewetting at 700°C, then the temperature was set to 550°C and silane was introduced into the growth chamber.

Figure 8 shows a SEM image of the morphology of Si NWs: they appear with a semi-alignment along the (111) direction due to the homoepitaxy on a silicon substrate. From TEM studies, the NWs are shown to exhibit a crystalline structure. The absence of stacking faults confirmed the good crystalline structure.

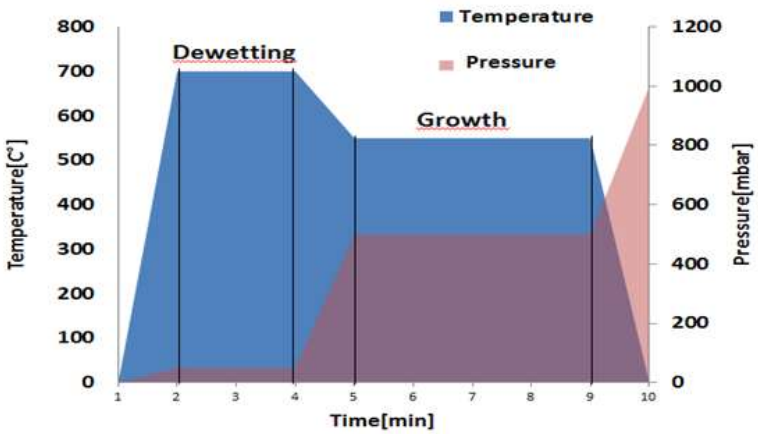


Fig. 7: The thermic and pressure curves of growth of SiNWs. The pink curve is a pressure curve and the blu curve is a termic curve both in time function.

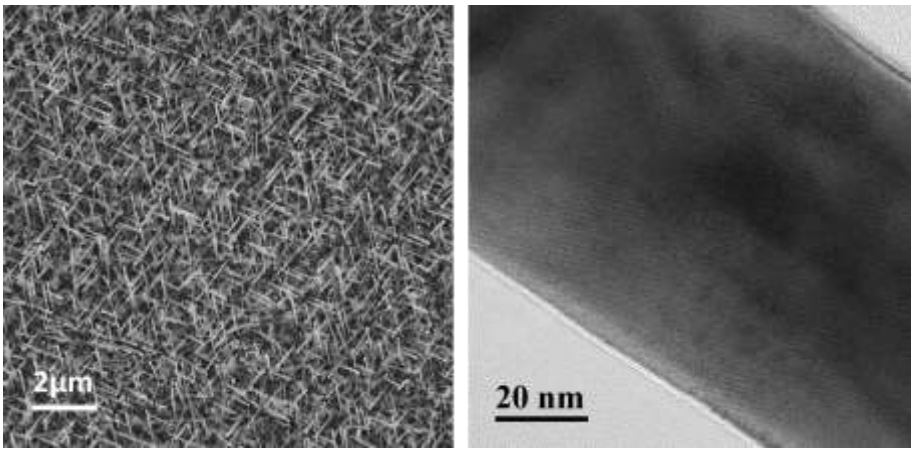


Fig. 8 Typical SEM-image of SiNWs (left), Typical TEM-image of a single SiNW (right).

### 2.3.4 $SiO_xC_y$ nanowires.

Silicon oxycarbide ($SiO_xC_y$) has been shown to have higher elastic modulus, bending strength and hardness, and chemical durability than conventional silicate glasses in aggressive environments and high temperature stability [22][23][24]. Furthermore, silicon oxycarbide has been demonstrated to increase platelet aggregation and activation, thereby promoting rapid clot formation and the onset of the acute inflammatory process, which is necessary for the creation of an adequate provisional matrix and the subsequent wound healing [28]. Moreover, $SiO_xC_y$ can be easily engineered through functionalization and decoration with macro-molecules and nanoparticles [25][26,27], which makes it an ideal platform for several experimental approaches.

SiOxCy NWs are grown by a CVD process on Si (001) and (111) substrates, with the same setup described for core shell NWs. The typical NWs, synthesized at 1050°C in open-tube configuration. In this process, carbon monoxide acts as dopant precursor, so that carbon-doped under-stoichiometric silicon dioxide NWs are obtained[20]. X-Ray Photoemission Spectroscopy (XPS) measurements indicated that carbon content was 13.4 at% (silicon 35.8 at%, oxygen 50.8 at.%) at the NW surface.

Nanowires are characterized at the IMEM CNR by scanning electron microscopy (SEM), high resolution transmission electron microscopy (HR-TEM) and high angle annular dark field imaging in scanning mode (HAADF-STEM)[32]

The morphology is shown in figure 9: the dense bundle of NWs long interwoven fibers cover the whole sample surface; The STEM-HAADF characterization (Fig. 9 center) are shown to exhibit an amorphous structure of SiOxCy and the Carbon map obtained with energy filtered TEM(figure 9 rigth) prove the presence of C inside the SiOx NWs[20]. Furthermore it is possible to

notice that NWs have a diameter of about 60 nm.

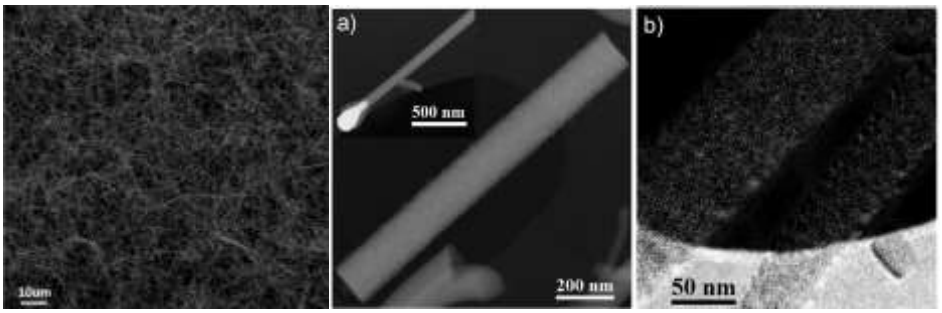


Fig. 9 Left: Typical SEM-image of a SiOx NWs bundle. Center: STEM-HAADF images of representative SiOxCy NWs. A NW tip is visible in the inset. Right: Carbon map obtained with energy filtered TEM. The map is taken on two wires lying close together across a hole of the holey-carbon support film.

In the following chapter the biocompatibility of this NWs will be evaluated in detail and in the chapter 4 and 5 two application of this kind of NWs will show.

**Bibliography**


[1] Giovanni Attolini F R F F M B G S and B E W 2010 *Nanowires* ed P Prete (InTech)

[2] Attolini G, Rossi F, Bosi M, Watts B E and Salviati G 2008 Synthesis and characterization of 3C–SiC nanowires *J. Non. Cryst. Solids* **354** 5227–9

[3] Morales A M 1998 A Laser Ablation Method for the Synthesis of Crystalline Semiconductor Nanowires *Science (80-. ).* **279** 208–11

[4] Westwater J 1997 Growth of silicon nanowires via gold/silane vapor–liquid–solid reaction *J. Vac. Sci. Technol. B Microelectron. Nanom. Struct.* **15** 554

[5] Kamins T I, Li X, Williams R S and Liu X 2004 Growth and Structure of Chemically Vapor Deposited Ge Nanowires on Si Substrates *Nano Lett.* **4** 503–6

[6] Attolini G, Rossi F, Fabbri F, Bosi M, Watts B E and Salviati G 2009 A new growth method for the synthesis of 3C–SiC nanowires *Mater. Lett.* **63** 2581–3

[7] Bao X-Y, Soci C, Susac D, Bratvold J, Aplin D P R, Wei W, Chen C-Y, Dayeh S A, Kavanagh K L and Wang D 2008 Heteroepitaxial growth of vertical GaAs nanowires on Si(111) substrates by metal-organic chemical vapor deposition. *Nano Lett.* **8** 3755–60

[8] Lin H-M, Chen Y-L, Yang J, Liu Y-C, Yin K-M, Kai J-J, Chen F-R, Chen L-C, Chen Y-F and Chen C-C 2003 Synthesis and Characterization of Core−Shell GaP@GaN and GaN@GaP Nanowires *Nano Lett.* **3** 537–41

[9] Bhunia S, Kawamura T, Watanabe Y, Fujikawa S and Tokushima K 2003 Metalorganic vapor-phase epitaxial growth and characterization of vertical InP nanowires *Appl. Phys. Lett.* **83** 3371

[10] Barrelet C J, Wu Y, Bell D C and Lieber C M 2003 Synthesis of CdS and ZnS nanowires using single-source molecular precursors. *J. Am. Chem. Soc.* **125** 11498–9

[11] Zhang X T, Liu Z, Leung Y P, Li Q and Hark S K 2003 Growth and luminescence of zinc-blende-structured ZnSe nanowires by metal-organic chemical vapor deposition *Appl. Phys. Lett.* **83** 5533

[12] Chang P-C, Fan Z, Wang D, Tseng W-Y, Chiou W-A, Hong J and Lu J G 2004 ZnO Nanowires Synthesized by Vapor Trapping CVD Method *Chem. Mater.* **16** 5133–7

[13] Park H-K, Yang B, Kim S-W, Kim G-H, Youn D-H, Kim S-H and Maeng S-L

2007 Formation of silicon oxide nanowires directly from Au/Si and Pd–Au/Si substrates *Phys. E Low-dimensional Syst. Nanostructures* **37** 158–62

[14] Monnink S H, van Boven A J, Peels H O, Tigchelaar I, de Kam P J, Crijns H J and van Oeveren W 1999 Silicon-carbide coated coronary stents have low platelet and leukocyte adhesion during platelet activation. *J. Investig. Med.* **47** 304–10

[15] Li X, Wang X, Bondokov R, Morris J, An Y H and Sudarshan T S 2005 Micro/nanoscale mechanical and tribological characterization of SiC for orthopedic applications. *J. Biomed. Mater. Res. B. Appl. Biomater.* **72** 353–61

[16] Katsuno M, Ohtani N, Takahashi J, Yashiro H and Kanaya M 1999 Mechanism of Molten KOH Etching of SiC Single Crystals: Comparative Study with Thermal Oxidation *Jpn. J. Appl. Phys.* **38** 4661–5

[17] Bolz A and Schaldach M 1990 {A}rtificial heart valves: improved blood compatibility by {PECVD} a-{S}i{C}:{H} coating. *{A}rtif {O}rgans* **14** 260–9

[18] Saddow S E 2012 Silicon Carbide Materials for Biomedical Applications *Silicon Carbide Biotechnology* (Elsevier Inc.) pp 1–15

[19] Casady J B and Johnson R W 1996 Status of silicon carbide (SiC) as a wide-bandgap semiconductor for high-temperature applications: A review *Solid. State. Electron.* **39** 1409–22

[20] Fabbri F, Rossi F, Negri M, Tatti R, Aversa L, Chander Dhanabalan S, Verucchi R, Attolini G and Salviati G 2014 Carbon-doped SiO x nanowires with a large yield of white emission. *Nanotechnology* **25** 185704

[21] Zekentes K and Rogdakis K 2011 SiC nanowires: material and devices *J. Phys. D. Appl. Phys.* **44** 133001

[22] Colombo P, Bernardo E and Biasetto L 2004 Novel Microcellular Ceramics from a Silicone Resin *J. Am. Ceram. Soc.* **87** 152–4

[23] Du P, Wang X, Lin I K and Zhang X 2012 Effects of composition and thermal annealing on the mechanical properties of silicon oxycarbide films *Sensors Actuators, A Phys.* **176** 90–8

[24] Tamayo A, Rubio J, Rubio F, Oteo J L and Riedel R 2011 Texture and micro-nanostructure of porous silicon oxycarbide glasses prepared from hybrid materials aged in different solvents *J. Eur. Ceram. Soc.* **31** 1791–801

[25] Onclin S, Ravoo B J and Reinhoudt D N 2005 Engineering silicon oxide surfaces using self-assembled monolayers. *Angew. Chem. Int. Ed. Engl.*

**44** 6282–304

[26] Fabbri F, Rossi F, Melucci M, Manet I, Attolini G, Favaretto L, Zambianchi M and Salviati G 2012 Optical properties of hybrid T3Pyr/SiO2/3C-SiC nanowires. *Nanoscale Res. Lett.* **7** 680

[27] Rossi F, Bedogni E, Bigi F, Rimoldi T, Cristofolini L, Pinelli S, Alinovi R and Negri M 2015 Porphyrin conjugated SiC/SiOx nanowires for X-ray-excited photodynamic therapy *Sci. Rep.* 1–6

[28] Zhuo R, Colombo P, Pantano C and Vogler E A 2005 Silicon oxycarbide glasses for blood-contact applications *Acta Biomater.* **1** 583–9

[29] Negri M, Dhanabalan S C, Attolini G, Lagonegro P, Campanini M, Bosi M, Fabbri F and Salviati G 2014 Tuning the radial structure of core-shell silicon carbide nanowires *CrystEngComm*

[30] Seo W-S, Koumoto K and Aria S 2004 Morphology and Stacking Faults of β-Silicon Carbide Whisker Synthesized by Carbothermal Reduction *J. Am. Ceram. Soc.* **83** 2584–92

[31] Fabbri F, Rossi F, Lagonegro P, Negri M, Ponraj J S, Bosi M, Attolini G and Salviati G 2014 3C–SiC nanowires luminescent enhancement by coating with a conformal oxides layer *J. Phys. D. Appl. Phys.* **47** 394006

[32] Rossi F, Fabbri F, Attolini G, Bosi M, Watts B E and Salviati G 2010 TEM and SEM-CL Studies of SiC Nanowires *Mater. Sci. Forum* **645-648** 387–90

# CHAPTER 3

# Nanowires and biocompatibility

**3.1 Introduction**

Nanotechnology has paved the way to the investigation and development of innovative systems with unique properties and applications in several fields, from sensoristics to nanomedicine. For health care applications, the ability to tailor material properties to clinical needs allows to design new nanosystems with enhanced performance for diagnostics, imaging, oncotherapy, regeneration medicine and drug delivery.

The following methods, procedure and cells were selected ad-hoc for each Nws based on their future applications.

The following paragraphs will focus on the different methods to evaluate the cytocompatibility of NWs

To evaluate the biocompatibility of Si(O,C) NWs, we decided to studied the effect of NWs on the biological system varying the parameters in view of future application. The evaluation of biocompatibility was conducted both on the NWs platforms (NWs with substrate) that with NWs detached of substrate.

### 3.1.1 State of Art: 1D nanostructure and Cytotoxicity

The current material research on nano/bio-medical applications aims at developing multifunctional nanomaterials as vehicles for drug delivery[1], intracellular probes, electrical- and fluorescence-based platforms [2] etc. Any innovative nano/bio-material in contact with animal and human cells and tissues must be cytocompatibile, and, to maximize the treatment efficacy, it must be internalized into the target cells[3]. Given these requirements, the significance of the ultrastructural study of the uptake process and the analysis of the interaction between nanomaterials and intracellular components is of clear importance. Among 1D nanostructures (nanotubes and nanowires), it has been assessed that some classes of materials, such as crystalline oxide nanowires (e.g. ZnO,[4] and $TiO_2$[5], are cyto-static or induce cell death, while other, as metal nanowires (e.g., based on gold,[6] iron,[7] and silver [8]), are essentially cytocompatible. Contradictory results, highlighting the variability due to dimension, surface properties, bio-durability, dose and exposure time, have been reported for carbon nanotubes [9] (single-walled and multiwalled) and semiconducting nanowires (e.g. silicon[10] and other III–V nanowires [11]). Given the lack of previous *in vitro* and *in vivo* data about cytocompatibility or cytotoxicity of Si based nanowires, we recently started a study about the interaction of these NWs with different cell lines. To perform the experiments the NWs were mechanically removed from the substrate through a mechanical process, so that the ultra-long NW fibers were broken up in short segments below 5 microns, and suspended in cell culture media for cell incubation. The NW behavior in water and in cell culture media was first studied by Dynamic Light Scattering (DLS) and Z potential measurements on diluted suspensions. The size distribution estimated by DLS was peaked around

900 nm, but showed tails down to 200 nm and up to 5 microns, in good agreement with the NW segment length measured by SEM on the dry product. The Z potential values were –(37 ± 3) mV in water, (12 ± 2) mV in RPMI 1640 medium, and +(2 ± 3) mV in a RPMISV medium. These values indicated that the material in water has a negative surface charge, likely related to O terminating the NW shell surface, and a good stability. The modification of the Z potential in cell culture media, where it becomes smaller and eventually changes sign, suggested that the medium components (e.g. proteins) interact with the NWs and likely cover their surface causing a different charge compensation. Nanowires (NWs) based on cubic silicon carbide (3C-SiC) have a strong potential to pave the way for the development of a novel generation of implantable nano-devices, chemically inert and compatible in biological environment. Indeed, 3C-SiC is a proved bio- and hemo-compatible material, and some prototypes for biomedical devices have been successfully realized by micromachining of thin films. The combination of 3C-SiC with silicon dioxide in core/shell structures (core/shell 3C-SiC/$SiO_2$ NWs) opens more ways to engineer the surface via functionalization and decoration with macro-molecules and nanoparticles. The potential use of core/shell NWs in nanomedicine is driven by the presence of the amorphous shell, because it can modify the material behavior in biological environment. For instance, for blood-contact applications, silicon oxide could induce a stronger aggregation and activation of platelets, thus promoting clot formation and acute inflammatory processes. Further, a peculiar feature of the core/shell NWs is their optical emission: the oxide shell enhances the core luminescence when the nanosystem is excited by highly energetic sources, as electron beams or X-Rays. This property opens the possibility to exploit 3C-SiC/$SiO_x$ NWs as radiation resistant scintillation nanostructures, which can be properly

functionalized to play an active role for new oncotherapies, e.g. X-Ray excited photodynamic therapy, in nanomedicine.

### 3.1.2 UP-TAKE

The plasma membrane is a selectively permeable membrane that defines the boundary and maintains the essential intracellular environment of the cell. Small and nonpolar molecules such as $O_2$ and $CO_2$ can readily diffuse across the lipid bilayer, however, polar molecules such as ions and larger nanomaterials are incapable of crossing the plasma membrane on their own. Under natural conditions, important ions and nanometer-sized proteins are transported across the lipid bilayer through specialized membrane-transport protein channels.[12] Most other nanoscale macromolecules and molecular assemblies are internalized through endocytosis (the process of uptake of macromolecules into cells by enclosing them in membrane vesicles, see Figure 1 and Table 1) upon contact with the cell membrane. These endocytosed nanomaterials are confined in endolysosomes (membrane bound vesicles) and are incapable of reaching the cytosol.[13] This endocytic fate of nanomaterials has been shown by various precedents in literature. As an example, 3.4-nm gold nanoparticles have been shown to be taken up by macrophages via a mechanism involving pinocytosis as indicated by atomic force microscopy (AFM) measurements.[14] In this study, transmission electron microscopy (TEM) and confocal microscopy images confirmed that 24 h after internalization, the nanoparticles were found in lysosomal bodies arranged in a perinuclear fashion. Endocytic fate is not limited to gold nanoparticles but has also been observed for iron oxide nanoparticles[15]–[18] and fullerenes.[19] While qualitative observations show that in most cases nanomaterials are contained within vesicular structures and cannot breach cell membrane

barriers, the kinetics, amount, and mechanism of uptake vary depending on numerous factors in the study such as purity of the nanomaterial, nanomaterial–cell incubation conditions, cell treatment, type of cell, and the type of nanomaterial.

Many applications that are conceived for synthetic and biological nanomaterials require breaching of the cell-membrane barriers to reach the cytosolic machinery or the nucleus of the cell. Transportation across cell membranes can allow for the delivery of siRNA[20] or other drugs to the cytosol[21] by utilization of a carrier that can circumvent the natural inability of these drugs to penetrate the cell membrane. The safe and efficient localization of nanomaterials into the cytosol may be critical in other applications such as phototherapy[22], [23] and intracellular imaging[24] as well. However, crossing cell membranes is inherently challenging due to the nature of the lipid bilayer and, from an evolutionary point of view, to protect the cellular function. Many nanomaterials have nonetheless demonstrated an ability to successfully penetrate cell membranes. Among natural systems, this ability has been observed in cell-penetrating peptides (CPPs) or cell-fusogenic peptides (such as those found on viruses) that are efficient at penetrating cell membranes without forming overt pores in lipid bilayers.[8], [25]–[27] Among synthetic nanomaterials, with the exception of very small molecules (such as metal clusters)[28] or needle-shaped materials (e.g., chemically functionalized carbon nanotubes), only cationic nanoparticles (metallic, quantum dots (QDs), and dendrimers)[29] are capable of penetrating cell membranes. However, in the process, they create pores in the cell membranes that can lead to cellular toxicity by destroying the delicate concentration balance of intracellular versus extracellular ions, proteins, and other important macromolecules that are required to protect the integrity and the normal function of a cell.

Alternatively, different approaches have been utilized to transport nanomaterials into the cytosol of cells:

i) disruption of endosomes and entry into cells through the “sponge-effect” mechanism[30] or the usage of chloroquine,[31]

ii) direct microinjection of nanomaterials into cells[32], [33]

iii) the use of electroporation[34]

iv) conjugation of natural cell-penetrating/-fusogenic chaperons to nanomaterials.[35]

An alternate means of membrane translocation of nanoscale-sized materials can rely on intelligent surface-structure design. However, the design principles of synthetic nano-scaffolds for membrane transport are far from being comprehensively understood. Typically, nanomaterial interactions with cell membranes are dictated by the chemical functionalities on the surface in addition to their shape and size. It is also observed that among natural systems, such as CPPs, not only the type of chemical groups but their relative arrangement also plays a key role in their interaction with cell membranes. Such peptides, while ineffective at crossing the cell-membrane barrier in their random-coil conformation, display an ability to penetrate or fuse with membranes after adopting an amphipathic $\alpha$-helical structure.[36] Clearly, there is much need to understand the impact of surface properties of nanomaterials with respect to their interactions with cells and to also harness that knowledge to create smart nanosystems. In line with this effort, this paragraph will focus on the current nanostructure and effect of their surface-chemical properties on interaction with cells.

In this paragraph the effect of size and shape of nanomaterials on their interaction with cells and internalization is discussed.

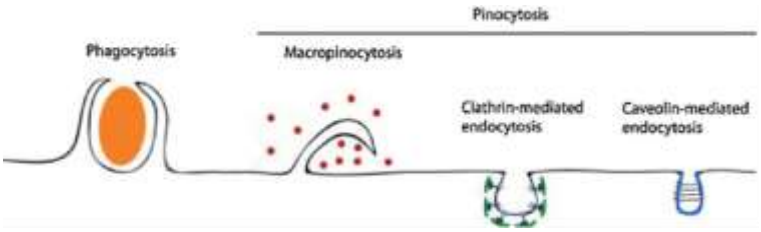


Fig.1: Major endocytic pathways. Adapted with permission from Reference [2]. Copyright 2003, Nature Publishing Group.

| *Type of endocytosis* | *Brief description* | *Size of vesicle formed* |
|---|---|---|
| **Phagocytosis** | Internalization of solid particles such as bacteria and yeast by specialized cells | Dependent on the particles being engulfed |
| **Pinocytosis** | Fluid-phase up-take molecules. Multiple pinocytic pathways are possible | (Below) |
| **Macropinocytosis** | Trapping of large fluid pockets by formayion and enclosure of membrane protrusions | > 1 µm |
| | Concentration of transmembrane receptors and bound ligands in ”coated pits” on the plasma membrane formed by the assembly of cytosolic proteins, the main assembly unit being clathrin | ≈ 120 nm |
| **Caveolae-mediated endocytosis** | Flask-shaped invaginations in the plasma membrane that mediante up-take of extracellular molecules into the cell by specific receptor binding | ≈ 50-60 nm |

Table 1: A brief description of the major endocytic pathways

The shape and size of nanoparticles has been found to greatly influence their cellular uptake. In a study by Chithrani et al., the uptake of 14-, 50-, and 74-nm gold nanoparticles was investigated in Hela cells (Figure 2).[37] It was found that the kinetics of uptake as well as the saturation concentration varied with the different-sized nanoparticles with 50-nm-size particles being the most efficient in their uptake, indicated that there might be an optimal size for efficient nanomaterial uptake into cells. The effect of nanoparticle shape on its internalization was also examined: spherical particles of similar size were taken up 500% more than rod-shaped particles, which is explained by greater membrane wrapping time required for the elongated particles. In other

studies, nanoparticle size has been shown to strongly affect the binding and activation of membrane receptors and subsequent protein expression. Examining the influence of shape and size of nanomaterials on cell interactions is crucial as this can have implications in toxicity.[36] One has to also consider that there is an inherent polydispersity within any given batch of nanoparticles, which needs to be controlled for predictable nanoparticle behavior with cells, otherwise different batches of the same nanomaterial might display different results in cell studies. Another very important factor is that even though nanoparticles display a certain size after synthesis, during the in vitro and in vivo studies they might aggregate into vastly different shapes and sizes that may dictate the outcome and interpretation of results.

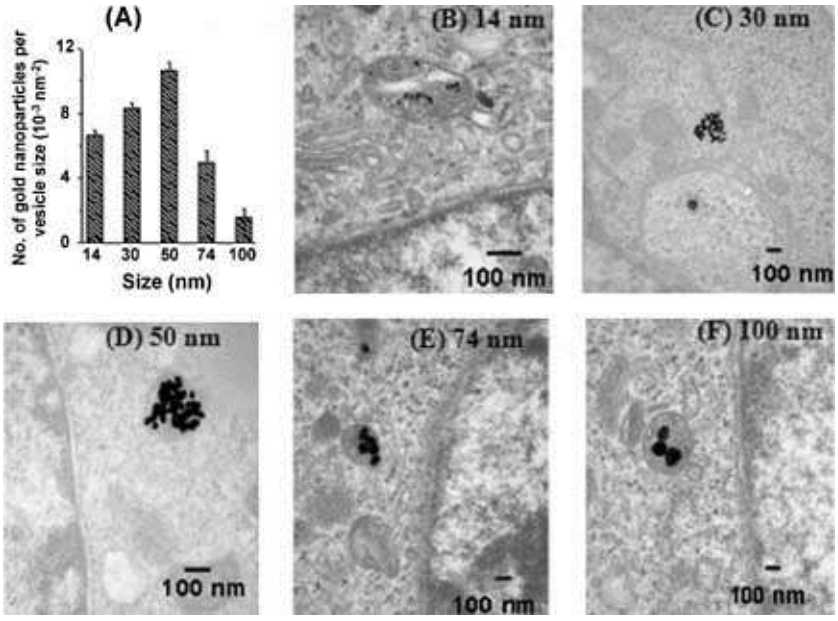


Fig. 2: TEM images of nanoparticles entrapped in vesicles within cells. A) Graph showing the number of nanoparticles per vesicle diameter versus nanoparticle size. TEM images of nanoparticles with a diameter of B) 14 nm, C) 30 nm, D) 50 nm, E) 74 nm, and F) 100 nm within vesicles. Reproduced with permission from Reference [37]. Copyright 2006, American Chemical Society.

### 3.2 In-vitro cytocompatibility of SiC-based nanowires

#### 3.2.1 SiC/$SiO_2$ NWs

We analyzed how the NWs often removing from the Si substrate a substrate affect cell viability, morphology and cell cycle progression, and specifically investigated oxidative stress, autophagy, and cellular uptake (internalization, compartmentalization, and cellular physical parameters). As representative cellular models, we selected a normal cell line (human-derm fibroblasts, HuDe, as non-cancer control cells) and three human cancer cell lines: lung adenocarcinoma alveolar basal epithelial cells (A549), breast cancer cells (MCF-7), and the monocytic cell line derived from acute monocytic leukemia (THP-1). The choice of the A549 and MCF-7 models was based on the evaluation of high incidence tumors which could be induced with standard protocols in nude mice for future *in vivo* studies. The additional THP-1 model was tested for its macrophage activity, which provides an insight into specific internalization pathways.

To inspect the midterm (up to 72 h) effects of the core/shell 3C-SiC/$SiO_2$ nanowires on the selected cellular models, the cell viability was monitored as a function of NW concentration in the range 1−100 μg/mL. Figure 3 shows the percentage of viable cells, as estimated by trypan blue exclusion and crystal violet staining assays, normalized to control untreated cells. The viability assays prove that only at the highest concentrations tested, i.e. 50 and 100 μg/mL, the cell proliferation starts to show a small downward trend. The effect is slightly cellular dependent, being the decrease highly significant ($p < 0.01$) for A549 cells and significant ($p < 0.05$) for THP-1 and HUDE cells, whereas for MCF-7 the cell viability is almost not affected by the treatment with

nanowires.

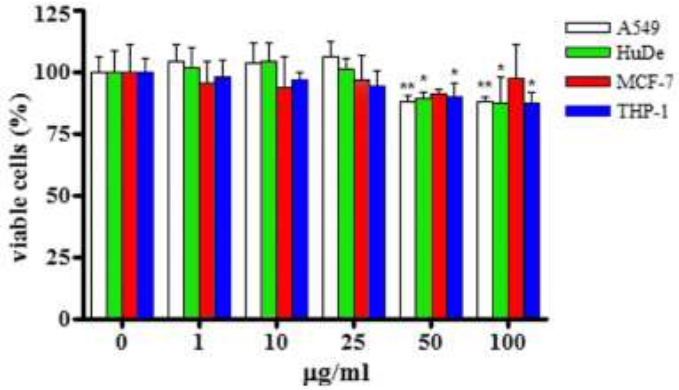


Fig. 3 : Cell viability assays in cells exposed to NWs from 1 to 100 µg/mL for 72 h. Values are normalized to controls. The figure shows the mean (±SD) of at least three separate experiments, each carried out in eight replicates. Significantly different from untreated control: *= $p < 0.05$; ** = $p < 0.01$.

The analysis of the cell cycle progression shows that the NWs do not induce any perturbation, in all the cellular models(Fig 4). Further, no sub-$G_0/G_1$ peak, corresponding to apoptotic cells, is detected in the cytograms. The NWs do not induce apoptosis, as proved also by morphological analyses (absence of changes typical of cell apoptotic death, including nuclear condensation and apoptotic bodies) and by the lack of increase of Annexin-V FITC/Propidium Iodide (PI) stained cells and of caspase-3 activation.

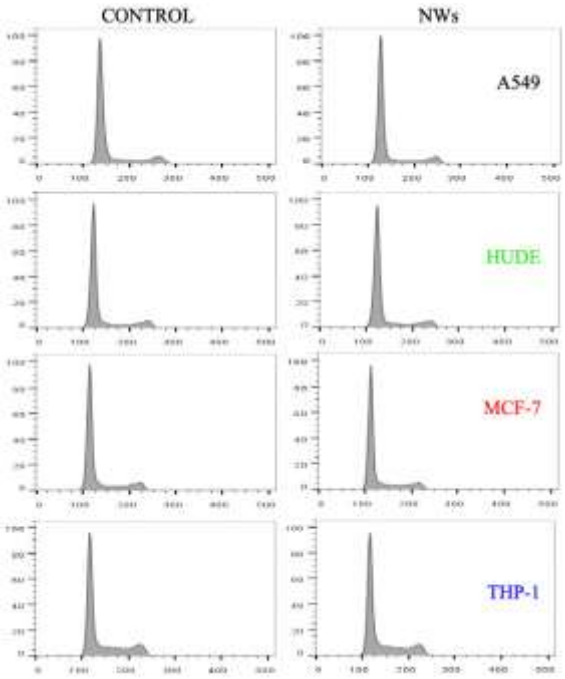


Fig. 4: Monoparametric DNA analysis of the cellular cycle distribution (after 24h, treatment with NWs 50 µg/ml). The different peaks correspond to G0/G1, S and G2/M phases.

Oxidative stress was evaluated through quantification of Reactive Oxygen Species (ROS), Thiobarbituric Acid Reactive Substances (TBARS) and carbonyl groups levels(Fig.5). Though NWs did not induce any ROS production in THP-1 and MCF-7 models, the intracellular ROS resulted significantly ($p < 0.05$) and highly significantly ($p < 0.01$) increased after the first hour of treatment compared to control untreated cells in A549 and HuDe models. However, basal levels tended to be restored after a few hours and the recovery was complete after 24 h. As assessed by TBARS and carbonyl groups, the persistent intracellular presence of NWs caused, following 4 h incubation, oxidation of proteins and lipid peroxidation of membranes. The increase of carbonyl groups was significant ($p < 0.05$) only at the higher concentration tested (50 µg/mL), in A549, HuDe and MCF-7 exposed cells. As for lipid peroxidation, the TBARS values were higher after treatment with NWs in all the cellular models. A dose-

dependent increase was observed in A549 and MCF-7, highly significant ($p < 0.001$) only for exposure to 50 µg/mL. In HuDe and THP-1 cultures, strong effects ($p < 0.001$) were detected also at the lowest concentration (10 µg/mL). These results indicate that the intracellular presence of NWs induced the same molecular events, i.e. oxidation of proteins and peroxidation of membrane lipids, in all the cell lines, but to a different extent. These effects are late and may be limited by the activation of protection systems, so NWs do not elicit cytotoxic activity leading to irreversible cellular damages or death. The antioxidant status of the cells was examined over time by measuring the glutathione contents, and no depletion of GSH was evidenced during the whole experimental period.

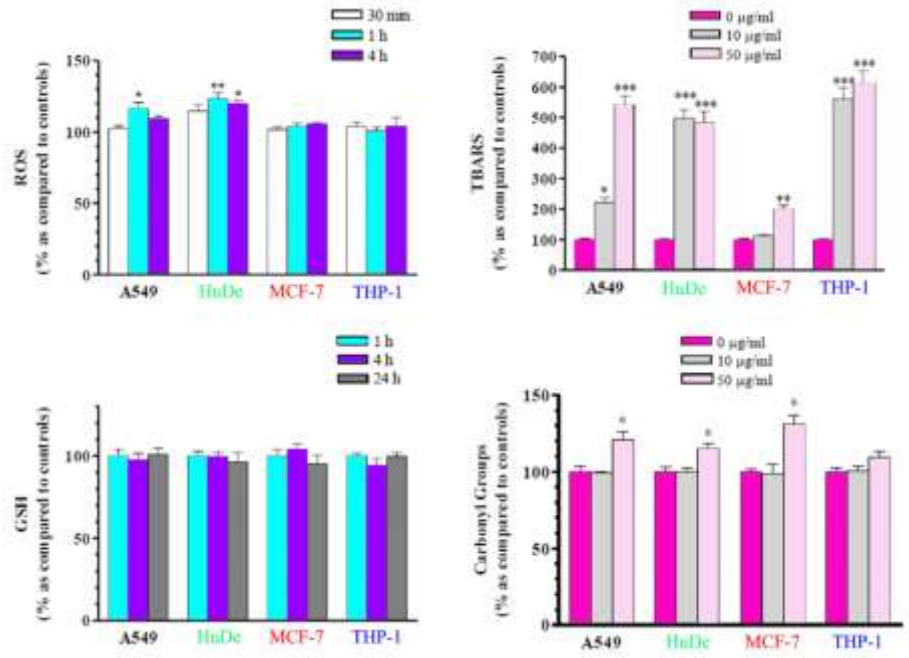


Fig. 5: Effects of NWs exposure on ROS, TBARS, Carbonyl Groups and GSH. Values (percentage vs control = (sample value/control value) × 100) are mean ± SD of three separate experiments, each carried out in triplicate. Significantly different from untreated control: * = $p < 0.05$; ** = $p < 0.01$; *** = $p < 0.001$.

Because many biomedical applications (e.g. biological sensing, drug delivery, electrophysiological experiments etc.) require a biological interaction on a time scale of at least several days, we also tested the long-term (10 days) NWs citocompatibility on the three adherent cellular lines (A549, MCF-7, and HuDe). Following recent literature protocols, a clonogenic assay was performed. Fig 6 shows the colony forming ability of the cells exposed to the NWs, at the concentration of 10 and 50 µg/mL, for 10 days. No significant reduction is observed, confirming that even on a time scale of 10 days the core/shell 3C-SiC/$SiO_2$ NWs do not elicit cytotoxic activity.

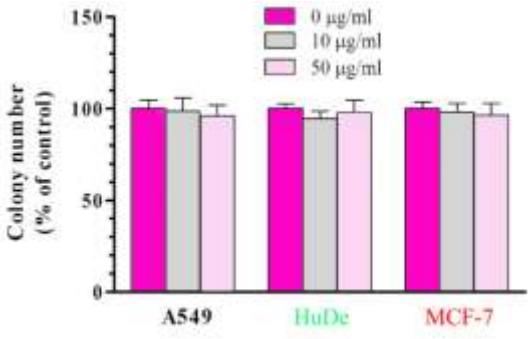


Fig. 6: Effects of long-term exposure to NWs, evaluated by clonogenic assay. The hystograms (means ± SD) report the colony forming ability of A549, HuDe, and MCF-7 cells treated for 10 days with NWs at the concentration of 10 and 50 mg/mL, compared to control cells.

Flow cytometry revealed modifications of physical parameters correlated with the NW uptake(Fig.7). As proved in literature,[38], [39] the side scatter (SSC) value is a reliable indicator of the presence of nanoparticles and fibers inside the cells. An increase of the SSC was detected during cell incubation with SiC/$SiO_2$ NWs (50 µg/mL), in particular for the A549 cellular model (mean SSC ratio (treated/control) statistically increased at 4 h ($p < 0.05$) and 24 h ($p < 0.001$)). When the NW concentration was varied, the mean SSC ratio exhibited a dose-dependent behavior, confirming that this parameter changes with the quantity of NWs internalized in cells.

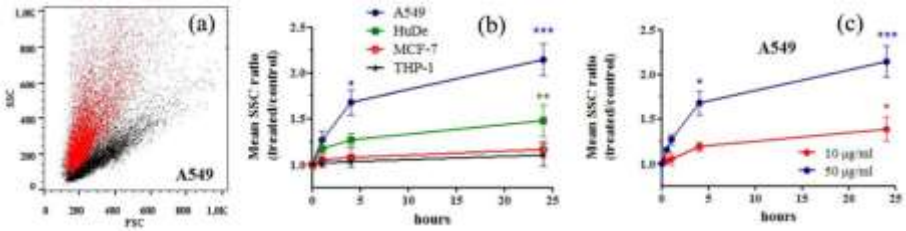


Fig.7: Flow cytometry analysis of side scatter (SSC) versus forward scatter (FSC) in A549 cells. Unexposed cells were scanned as controls and compared to cells exposed to NWs @ 50 µg/ml for 24h. Representative cytograms are displayed. (b) Influence of the incubation time on side scatter for the different cell lines. (c) Change of the SSC parameter over 24 h in A549 cells treated with NWs @ 10 or 50 µg/mL. The curves indicate that uptake is fast and uptake rate is similar at the two doses. Data are expressed as Mean SSC ratio (treated/control) + SD. Significantly different from untreated control: *= ($p<0.05$); **=($p<0.01$); ***=($p<0.001$).

No major alterations in cell morphology between cells treated with NWs and their controls were observed by scanning electron microscopy analysis. In particular, no morphological alteration related to cellular suffering and programmed cell death, such as membrane blebs and rounded apoptotic bodies, was detected. However, cellular spreading resulted higher in cells treated with the NWs, compared to controls, and cytoplasmic protrusions, in particular lamellopodia and filopodia, were detected as the structures of contact between the cell membrane and extracellular clusters of NWs. Single NWs, partly internalized inside the cells, were also detectable

TEM studies confirmed that the NWs did not induce shape/size changes nor alterations of the nucleus/cytoplasm ratio. Clear pictures of NW internalization were obtained(Fig.8). As show previously, the cellular uptake of a nanomaterial can occur by three main mechanisms: receptor-mediated endocytosis, pinocytosis, and phagocytosis.[7] In our samples, contacts

between the plasma membrane and individual nanowires or small groups of nanowires were frequent at both the concentrations of 10 and 50 μg/ml. In the proximity of NWs, the plasma membrane presented cytoplasmic protrusions, characteristics of the process of endocytosis, which will expand to encompass the nanowires in small vesicles. Analyzing the morphology of these protrusions, three types of macropinocytosis process, such as lamellopodia-like, circular ruffles, and blebs, were identified. In detail, the lamellopodia-like appears as a thin and long cytoplasmic evagination that surrounds the nanowire from one single side in the vicinity of the membrane, the structure circular ruffle is constituted by two symmetrical protrusions whose ends approach incorporating the nanowire and the structure in blebs is recognizable by the bulging circular end.

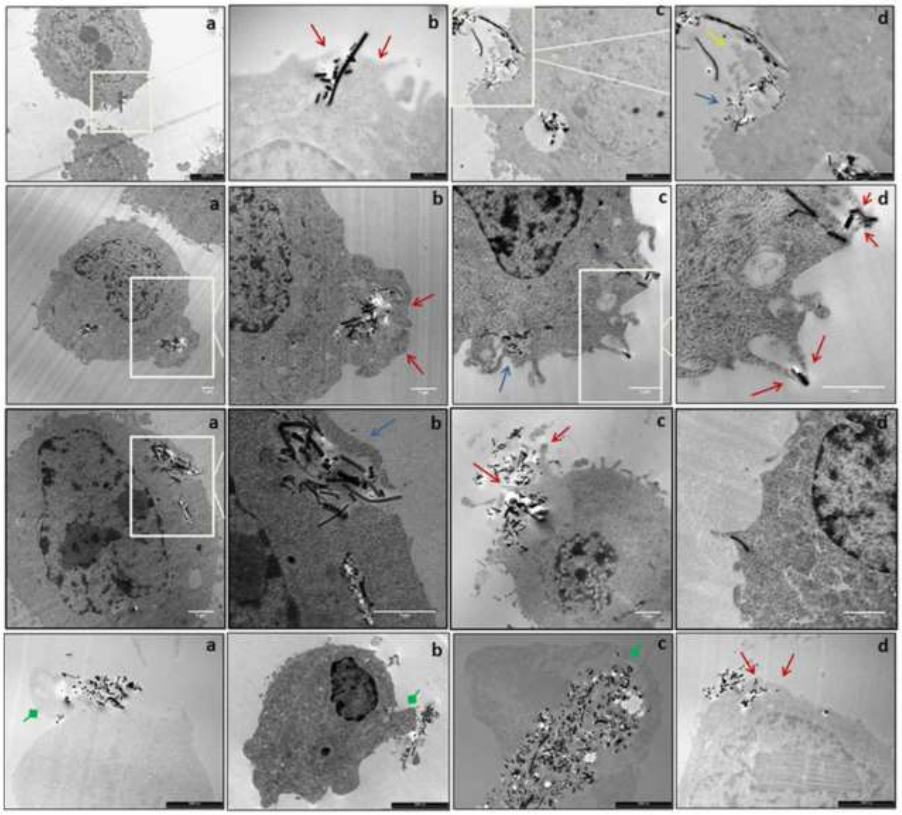

Fig.8: NWs internalization analyzed by TEM in A549 cells (first line), MCF-7 cells (second line), HuDe cells (third line) and THP-1 cells (fourth line). The red arrows indicate macropinocytosis with circular ruffles, the blue arrows indicate lamellopodia-like macropinocytosis, and the yellow arrows indicate blebs macropinocytosis. Pseudopodia engulfing NWs at an early (fourth line, a-b) and late (fourth line, c) stage of the phagocytosis process are indicated by green arrows with square heads. A NW directly penetrating the cell membrane is visible in the micrograph d of the third line. [40]

The THP-1 cells showed, in addition to the micropinocytosis, a specific pathway for the internalization of NWs: phagocytosis. This particular mechanism, exclusive of macrophage-like cells, has been observed at different stages : in the initial phase cells emit visible pseudopodia, which subsequently surround agglomerates of several nanowires in order to incorporate them into a single

vacuole(Fig.9). The analysis of cellular vesicular transport (Fig.9) showed single or small groups of NWs in small vesicles, predominantly localized in the vicinity of the plasma membrane, whereas clusters of NWs are compartmentalized in round big vesicles with a perinuclear localization. The larger vesicles are presumably engaged on compartmentalization function, whereas the smaller vesicles are used for the vesicular transport. Further, individual nanowires are occasionally seen trapped in the cytoplasm and not included in vesicular structures. However, it must be stressed that the NWs are never inside the nucleus nor in contact with the nuclear envelope.

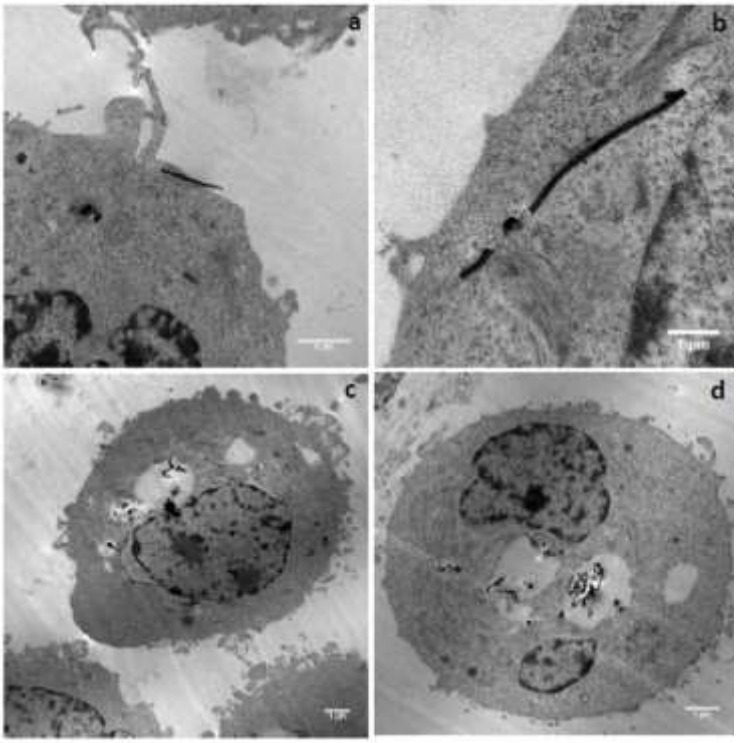


Fig. 9 SEM micrographs showing cases of NWs that penetrate directly the cell membrane (a) and are trapped in the cytoplasm (b) and the vesicles intracellular compartmentalization of NWs (c-d). [40]

### 3.2.2 3C-SiC Nanowires

As with $SiC/SiO_2$ Nws we analyzed how NWs affected cell viability, morphology and cell cycle progression, and specifically investigated oxidative stress, autophagy, and cellular uptake (internalization, compartmentalization, and cellular physical parameters). As representative cellular models, we selected a cardiac muscle cell line, designated HL-1, from the AT-1 mouse atrial cardiomyocyte tumor lineage. HL-1 cells can be serially passaged, yet they maintain the ability to contract and retain differentiated cardiac morphological, biochemical, and electrophysiological properties. Ultrastructural characteristics typical of embryonic atrial cardiac muscle cells were found consistently in the cultured HL-1 cells. The choice of the HL-1 models was based on the possible future application. These NWs were investigated because they are the base materials of a cardiac Patch(see chapter 5) and could provide important information for future *in vivo* studies.

To evaluate the effects of the 3C-SiC nanowires on the selected cellular model, cell viability was monitored as a function of NW concentration in the range 1−50 μg/mL after 24h and 48h. Fig 10 shows the percentage of viable cells, as estimated by trypan blue exclusion and crystal violet staining assays, normalized to control untreated cells. Viability assays prove that only at the highest concentrations tested, i.e. 50 μg/mL, cell proliferation starts to show a small downward trend. The effect is significant ($p < 0.05$) for HL-1.

We observed cell death, lysis, apoptosis, but only a slight drop of ATP for 48 hours after treatment with 50 mg / ml. This concentration also had an antiproliferative effect, with reduction in the number of cells starting from 24h.

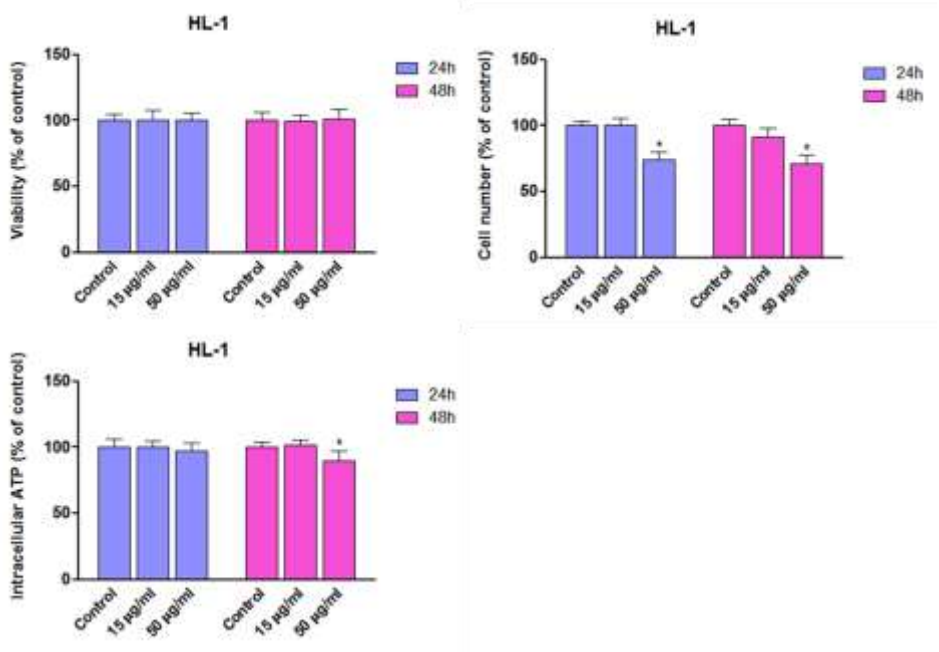


Fig. 10: Cell viability assays in cells exposed to SiC NWs from 1 to 50 µg/mL for 24 and 48 h. Values are normalized to controls. The figure shows the mean (±SD) of at least three separate experiments, each carried out in eight replicates. Significantly different from untreated control: *= $p < 0.05$;

The analysis of the cell cycle progression shows that the NWs do not induce any perturbation, in all the cellular models (Figura 10). Further, no sub-$G_0/G_1$ peak, corresponding to apoptotic cells, is detected in the cytograms.

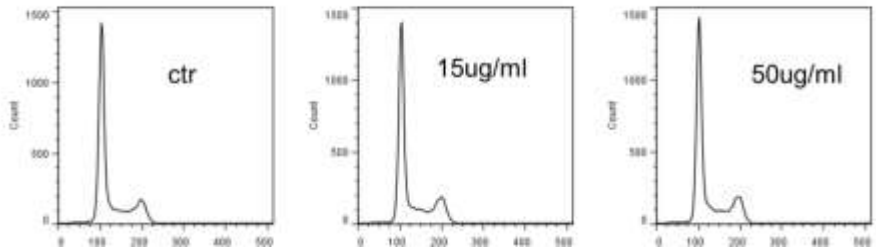


Fig. 11 Monoparametric DNA analysis of the cellular cycle distribution (after 24h, treatment with NWs 15 µg/ml and 50 µg/ml). The different peaks correspond to $G_0/G_1$, S and $G_2/M$ phases

As showed previously the side scatter (SSC) value is a reliable indicator of the presence of nanoparticles and fibers inside the cells. Significant differences between the SSC value with NWs and without were not detected. (Figure 12) The data confirmed that the cells do not uptake NWs(up to 24h).

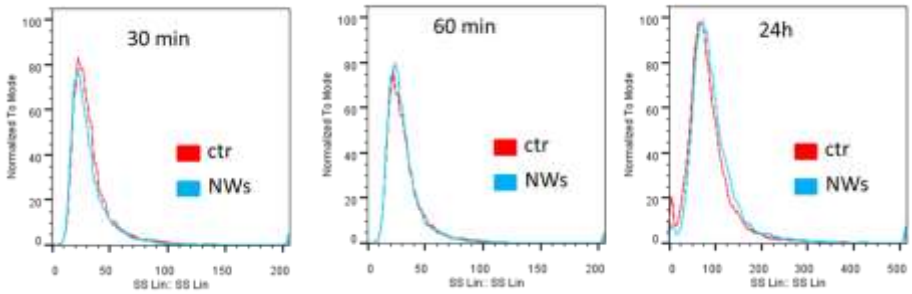


Figure 12: Side scatter (SSC) in HL-1 cells. Unexposed cells were scanned as controls and compared to cells exposed to NWs @ 50 µg/ml for different time. (a) 30 min(b)60min(c)24h. The SSC parameter over 24 h in HL-1 cells treated with NWs @ 50 µg/mL and in Ctr are comparable. The curves indicate that there aren't uptake.

Oxidative stress was evaluated by Thiobarbituric Acid Reactive Substances (TBARS).

Reactive oxygen species generation was not detected up to 60 min and with up to 50 ug/ml. The T-BARS were evaluated to 24h(Figure 14). No significantly

differences, between 0 µg/ml and 15 µg/ml, were detected; only a concentration up to 50 µg/ml caused a slight lipid peroxidation. The effects were quite negligible and were noticeable only to concentrations higher than those we used.

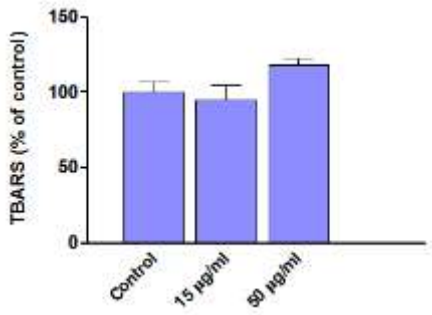


Fig. 14: The graph shows oxidative stress evaluation by T-BARS after 24h(Figure 14).

### 3.3 NWs platform: Biocompatibility evaluation

We analyzed the effect of NWs with Si substrate on cell viability, adhesion and morphology. As representative cellular models, we selected two different cell lines, the A549 human adenocarcinoma alveolar basal epithelial cells and L929 mouse fibroblast cells (NCTC clone 929 of strain L, derived from a C3H/An male mouse) were purchased from American Type Culture Collection (ATCC, Manassas, VA, USA) and cultured in DMEM. All media were supplemented with 10% FBS, penicillin (100 U/ml), streptomycin (100 µg/ml) and L-Glutamine (2 mM) and the cells were incubated at 37°C and 5% CO2 in a water saturated atmosphere.

L929 mouse fibroblasts are one of the standard cell lines specified in ISO 10993-5 for cytotoxicity tests, and is also recommended by the American Society for Quality Control. In this thesis we extended the analysis to A549 human lung adenocarcinoma epithelial cells, which are widely used for in vitro toxicity experiments.

#### 3.3.1 ISO 10993 Biocompatibility guide line

ISO (the International Organization for Standardization) is a worldwide federation of national standards bodies (ISO member bodies).

ISO 10993 consists of the following parts, under the general title *Biological evaluation of medical devices*:

- *Part 1: Evaluation and testing within a risk management process*
- *Part 2: Animal welfare requirements*
- *Part 3: Tests for genotoxicity, carcinogenicity and reproductive toxicity*

- *Part 4: Selection of tests for interactions with blood*
- *Part 5: Tests for* in vitro *cytotoxicity*
- *Part 6: Tests for local effects after implantation*
- *Part 7: Ethylene oxide sterilization residuals*
- *Part 9: Framework for identification and quantification of potential degradation products*
- *Part 10: Tests for irritation and skin sensitization*
- *Part 11: Tests for systemic toxicity*
- *Part 12: Sample preparation and reference materials*
- *Part 13: Identification and quantification of degradation products from polymeric medical devices*
- *Part 14: Identification and quantification of degradation products from ceramics*
- *Part 15: Identification and quantification of degradation products from metals and alloys*
- *Part 16: Toxicokinetic study design for degradation products and leachables*
- *Part 17: Establishment of allowable limits for leachable substances*
- *Part 18: Chemical characterization of materials*
- *Part 19: Physico-chemical, morphological and topographical characterization of materials* [Technical Specification]
- *Part 20: Principles and methods for immunotoxicology testing of medical devices* [Technical Specification]

#### 3.3.1.1 Section 5-Cytotoxicity Test

ISO 10993-5 describes test methods to assess the in vitro cytotoxicity of medical devices.

These methods specify the incubation of cultured cells in contact with a device and/or extracts of a device either directly or through diffusion.

These methods are designed to determine the biological response of mammalian and/or fibroblast cells in vitro using appropriate biological parameters.

As stated in ISO 10993-5 guidelines “an important quality issue of materials for medical devices having direct or indirect contact with the body tissue is the biocompatibility”. Any biomaterial promising for *in-vivo* implanting has to be analyzed for biocompatibility evaluation with specific *in-vitro* tests, starting from cytotoxicity tests. L929 mouse fibroblasts are the standard cell line for cytotoxicity tests, as recommended by American Society for Quality Control. In our work we extend the analysis to A549 human lung adenocarcinoma epithelial cells, which are widely used for *in-vitro* toxicity experiments.

### 3.3.2.1 SiC/SiO2 NWs and SiC NWs

The indirect contact test, showed in figure 15, allowed to exclude the release of any cytotoxic agents for all the NW structures. Fig.16 shows the histograms of cell viability for cells cultured with contaminated, i.e. left in contact with the NW samples for 24h or 10 days, medium. The bars are normalized to control cells. For both L929 and A549 cells, the CellTiter-Glo and MTT viability assays are in very good agreement with each other and attest a viability greater than 95% not affected by any toxic contamination. We also verified that the cell cultures treated with the contaminated medium did not show any alteration of the normal cell cycle progression. According to ISO 10993-5, a material is accepted as biocompatible if the viability is greater than 70%, and our test results demonstrate that this criterion is met by all the analyzed NW structures, core/shell SiC/$SiO_2$ NWs and bare SiC NWs.

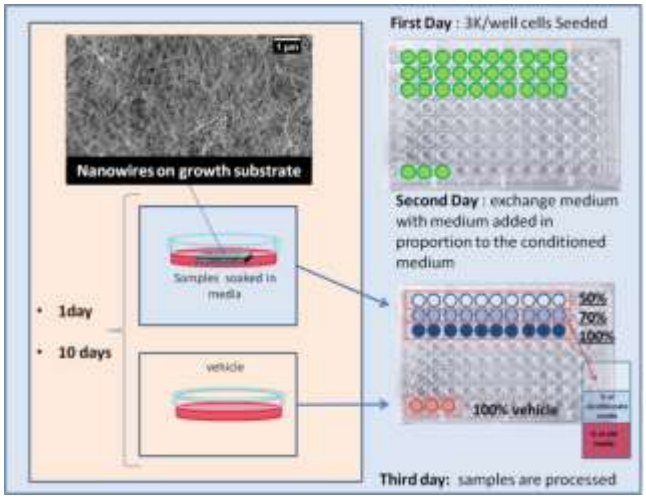


Figure 15: Schematic representation of indirect methods. In the pink box are showed the procedure to create the conditioned media after 1 day and 10 day. In the blue box(right) are showed the procedure to test this conditionate media after 1 day from seeding. The third day samples are processed with MTT and CellTiter Glo.

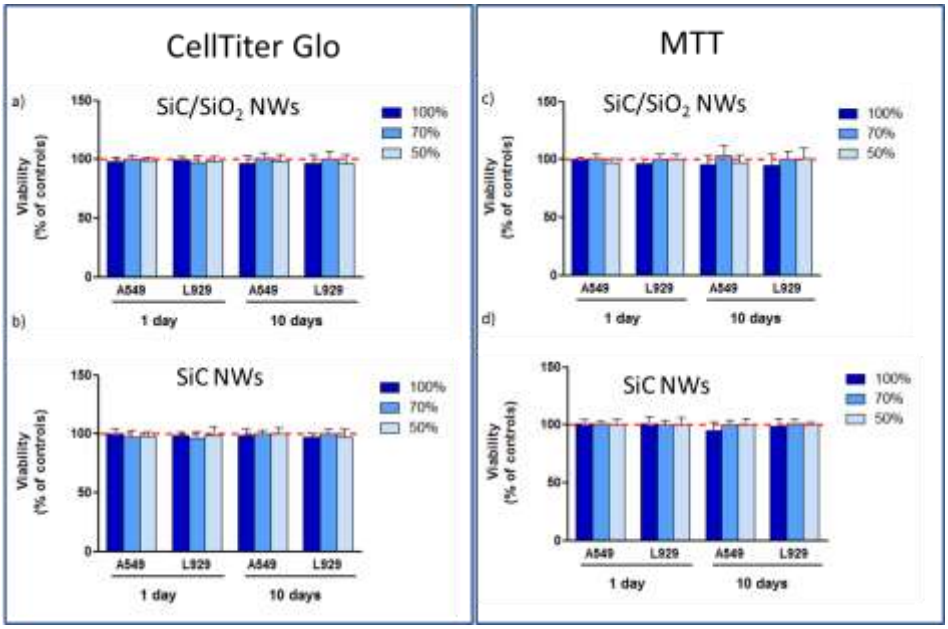


Fig. 16.: Cell viability, estimated by CellTiter-Glo (left column, a-c) and MTT (right column, d-f) assays, for A549 and L929 cells cultured according to the ISO 10993-5 protocol for indirect contact toxicity tests.

The direct contact test was then performed using the NW samples as platforms for culturing L929 and A549 cells. Twenty-thousand cells/ml were seeded on 1cm x 1 cm NW samples and cultured in DMEM. Plates were maintained at 37°C and 5% $CO_2$ in a humidified atmosphere for 24 or 48h; the cell viability was then analyzed via CellTiter-Glo assay, as preliminary studies determined that MTT assays were not feasible for the NW samples due to direct chemical interactions with the material that did not reflect the biological response.

Fig. 17 shows the cell viability (A549: panel a, L929: panel b) obtained at 24 and 48 h after cell seeding over the NW samples. In agreement with ISO 10993-5 guidelines, the cell viability related to direct contact tests over

polyethylene terephthalate (PET), as negative control, and copper (Cu), as positive control, is reported for comparison. We also tested a natively oxidized Si flat sample, as reference of the NW growth substrate. As a general remark, flat samples (PET and Si) favour indeed a higher cell viability, but NW platforms are suitable to maintain the cell culture over 48 h. To confirm the adhesion and proliferation of live cells on the NW samples after 24 or 48h, the samples were thoroughly washed with DMEM and phosphate buffer solution (PBS, Life Technologies) and then marked with calcein AM (GREEN), a fluorescent dye with excitation/emission wavelengths of 495/515 nm and propidium iodide(RED), a fluorescence dye with excitation/emission wavelengths of 493 / 636 nmFluorescence microscopy observations were performed after 30' with an epifluorescence microscope (Axioscope, Zeiss, Germany).

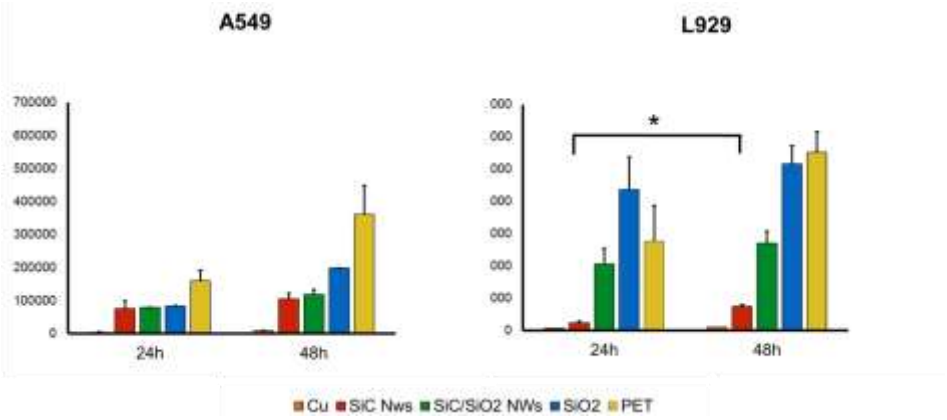


Fig. 17 Direct contact toxicity tests. CellTiter viability assay on A549 (a) and L929 (b) cells cultured for 24 and 48 h over different platforms: SiC NWs, SiC/$SiO_2$ core/shell NWs, flat $SiO_2$, and control PET and Cu surfaces. Only differences among NWs sample between 24 and 48h are indicated in the graph (*=p<0.05)

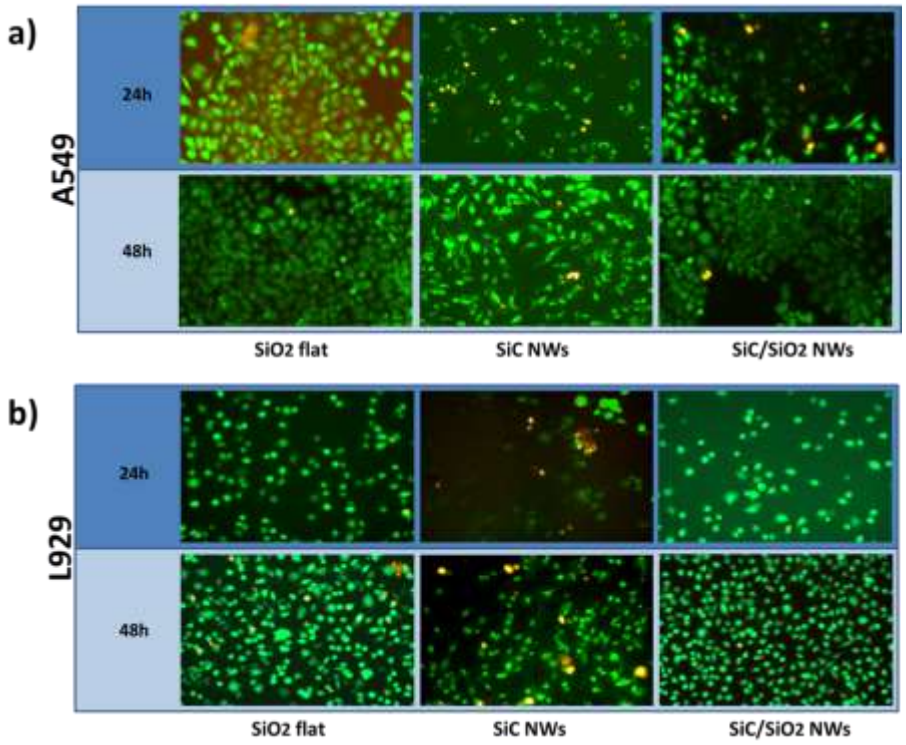


Fig. 18: Fluorescence images acquired on A549 (a) and L929 (b) cells cultured for 24 and 48 h on flat $SiO_2$, SiC NWs, and SiC/$SiO_2$ core/shell NWs. The fluorescent green cells were marked with calcein AM and indicate living cell , the fluorescent red/orange cells were marked with propidium iodide and indicate cell death.

Further, the viability of A549 cells over SiC/$SiO_2$ and SiC NWs was comparable within the error bars, indicating that the mechanisms of cellular adhesion and proliferation are mainly influenced by the surface morphology of the NW network, which is almost the same in all samples, and not by NW composition and structure. For L929 cells, the viability was slightly lower on SiC NWs compared to core/shell. In particular, a small adhesion was observed after 24h but the cell proliferation occurred at a normal rate after 48h.

To study cellular morphology and shape on NW samples and a flat Si reference samples were analysed by SEM.

For SEM observation of A549/L929 cells and platelets over the NW platforms, the samples were first washed with PBS at 37°C and then fixed in 2.5% glutaraldehyde in 0.1M sodium cacodylate buffer for 30' at room temperature. Next the samples were dehydrated with a sequence of treatments in alcohol at increasing concentrations. Finally, the samples were covered with a thin gold layer deposited by sputtering. Cell distribution and morphology on the NWs were characterized using a Field-Emission SUPRA40 Zeiss SEM equipped with a GEMINI FESEM detection column, operated at 3 keV.

Figure 19 and Figure 20 report representative SEM pictures of A549 and L929 cells, respectively, imaged at 24h (top line) and 48 h (bottom line) after seeding. For all the samples, the cellular membrane had the typical morphology of healthy living cells. No morphological alterations related to cellular suffering and programmed cell death, such as membrane blebs and rounded apoptotic bodies, were detected. Compared to the flat Si sample, a larger number of rounded cells are present on the NW platforms (see in particular the comparative images at 24h, top line in Fig. 19 and 20). However, after 48h the analysis of cellular spreading and cytoplasmic protrusions confirmed that cells adhered on the NW platform, with lamellopodia and filopodia entangled in the nanowire network.

It is known that cell adhesion plays an important role in the normal progression of cell cycle, such as the control of growth, differentiation during development and the spreading behaviour[41]. On NW platforms, a longer time is required to create an extracellular matrix, which affects the adhesion.

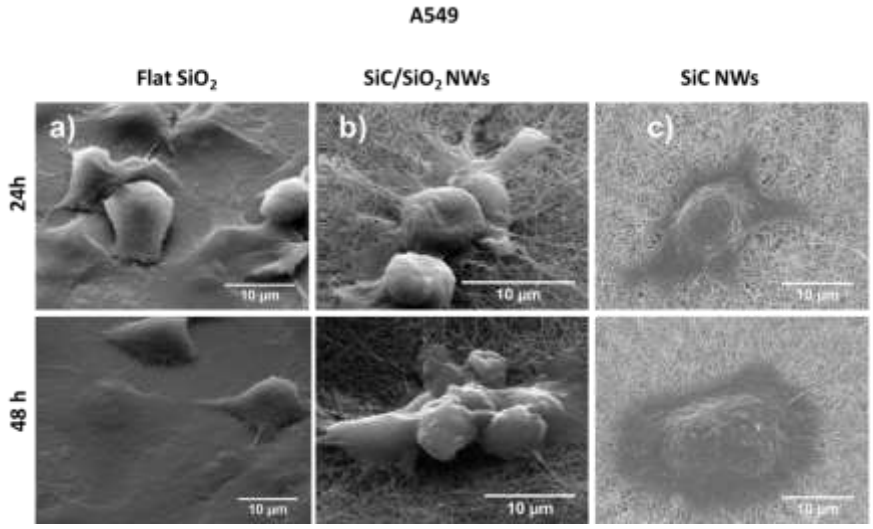


Fig.19: SEM images of A549 cells cultured 24h (top line) and 48h (bottom line) over different platforms: flat Si, $SiO_xC_y$ NWs, $SiC/SiO_2$ core/shell NWs and SiC NWs.

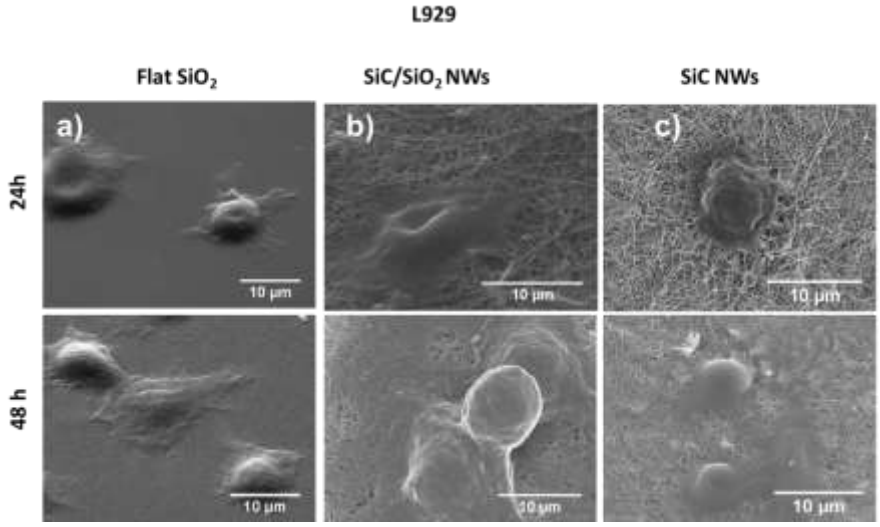


Fig. 20: SEM images of L929 cells cultured 24h (top line) and 48h (bottom line) over different platforms: flat Si, $SiO_xC_y$ NWs, $SiC/SiO_2$ core/shell NWs and SiC NWs.

The attachment and spreading of cells on biomaterials are mediated by highly complex structures called focal adhesions, which are multi-protein, microscale

assemblies involving clustering of ligated transmembrane receptor integrins on the nanoscale. It has been shown that the spacing between the integrin ligands is important to integrin clustering and focal adhesion. There is more evidence that clustering of integrins to assembly requires a spacing between ligated integrins around 50–70 nm. Nanotopographies with spacings larger than 100 nm inhibit cell adhesion.

In our case, the NW diameter ranges between 20 (for SiC NWs) and 60 (for core/shell NWs)  nm and the distances between nanowires vary from hundreds nm to several microns. Hence, although integrin clustering may occur on a single nanowire, the microscale focal adhesion assembly can be impaired because of the long distances between nanowires. The signals from the extracellular matrix transduced via focal adhesion into the cell are very important to cell functions and a less-effective process, as over NW platforms, can account for the lower cell viability observed on NWs compared to the flat Si reference and the PET control.

### 3.3.2.2 SiOxCy NWs

Tissue regeneration requires biomaterials capable to provide a scaffold for ingrowing cells and replace the missing extracellular matrix (ECM). The natural ECM is a complex structure, which creates a controlled microenvironment that coordinates cell activity by providing a vast array of biochemical and mechanical signals. Biomaterials therefore should ideally be bioactive, i.e. possess adequate physical and chemical properties to promote wound healing and regeneration, support cell function, by providing cells with direct stimuli to cell growth and differentiation and activate metabolic cascades that are conductive to tissue repair. Silicon oxycarbide ($SiO_xC_y$) has been shown to have higher elastic modulus, bending strength and hardness, and chemical durability than conventional silicate glasses in aggressive environments and high temperature stability. Furthermore, silicon oxycarbide has been demonstrated to increase platelet aggregation and activation, thereby promoting rapid clot formation and the onset of the acute inflammatory process, which is necessary for the creation of an adequate provisional matrix and the subsequent wound healing. Moreover, $SiO_xC_y$ can be easily engineered through functionalization and decoration with macro-molecules and nanoparticles, which makes it an ideal platform for several experimental approaches.

Micro- and nano-structured materials can provide specific topographical and mechanical cues, which are known to affect cell behavior through activation of focal adhesion-mediated intracellular signaling cascades. Nanowires (NWs) are one dimensional structures that can be arranged in three-dimensional (3D) bundles, which strikingly resemble the organization of the ECM fibrils and could therefore be a promising candidate for artificial matrices in different clinical situations.

The aim of the present works was to investigate whether $SiO_xC_y$ nanowires are a viable scaffold candidate for the regeneration of connective tissue by assessing the responses of a fibroblastic cell line to NWs-coated substrates and the effects of such NW coating on platelet activation.

To study the cytotoxic effect of SiOxCy NWs we followed the ISO 19003-5 protocol explained in detail in the paragraph 3.3.2

Indirect contact toxicology test is as easy method to study the contamination effect of sample, by chemical agents, in-vitro. In order to exclude whether chemical agents released in the media included cytotoxic species , samples were soaked in the DMEM for 1 day and 10 days and the cytotoxicity was studied. The viability evaluation studied by ATP-quantification(CellTiterGlo assay) and by MTT assay, is reported in Fig.23. In greater detail the Fig. 23 shows the histograms of cell viability for cells cultured with different aliquot of conditioned media , i.e. left in contact with the NW samples for 24h or 10 days. The bars are normalized to control cells.

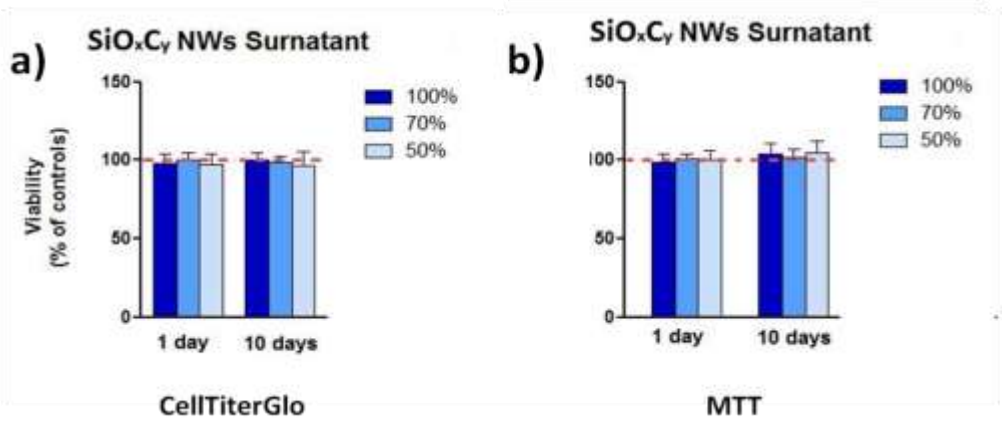


Fig.23 Cell viability, estimated by CellTiter-Glo (a) and MTT (b) assays, for L929 cells cultured according to the ISO 10993-5 protocol for indirect contact toxicity tests.

The viability assays are in very good agreement with each other and attest a viability greater than 95% not affected by any toxic contamination. We also verified that the cell cultures treated with the contaminated medium did not show any alteration of the normal cell cycle progression. According to ISO 10993-5, a material is accepted as biocompatible if the viability is greater than 70%, and our test results demonstrate that this criterion is met by all the analyzed NW structures.

The direct contact test was used to study the effect of surface morphology on the cells growth and differentiation in agreement with ISO 10993-5. The cells were seed on the NWs and the adhesion and proliferation was studied after 24-48 and 96h by fluorescence microscopy. The SEM was used to evaluated the cell spreading and the interaction between cell and NWs (Fig. 26).

Figure 24 presents the evaluation of cell viability by fluorescence microscopy images of L929 seeded for 24h(a,b,g,h), 48h(c,d,I,l) and 96h(e,f,m,n) on the SiOxCy NWs bundle(panel 1) and on the SiO2 flat (panel 2). Calcein (green)marked the living cells and propidium(orange) marked the nucleus of dead cells. The rate of cell growth was higher in the $SiO_2$ flat substrate in the first 48h, but after 96h the cells on the NWs were less affected by the contact inhibition in the 3D substrate, the growth increased respect other substrate. Even if apparently on both substrate the number of death cells are low the cells shape on NWs is typically of viable and healthy cells, otherwise on the $SiO_2$ flat the cells present the typically apoptotic body . The quantification of percentage areas covered by cells live in fluorescence images was showed in figure 25.

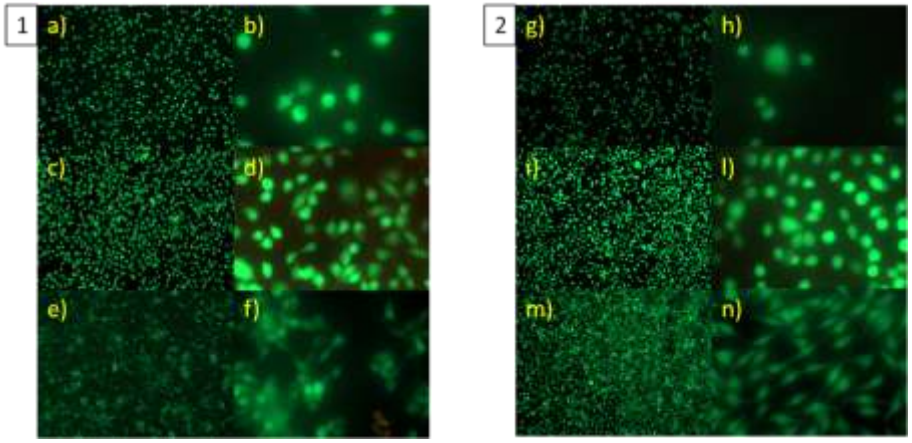


Fig. 24: Figure Reports cell viability at 24 hours, 48 hours and 96 hours after cell seeding on NW samples (left handed panel) or on a natively oxidized Si flat sample, as a reference (right handed panel). Cells were stained with calcein and propidium iodide for viable and dead cell labeling, respectively.

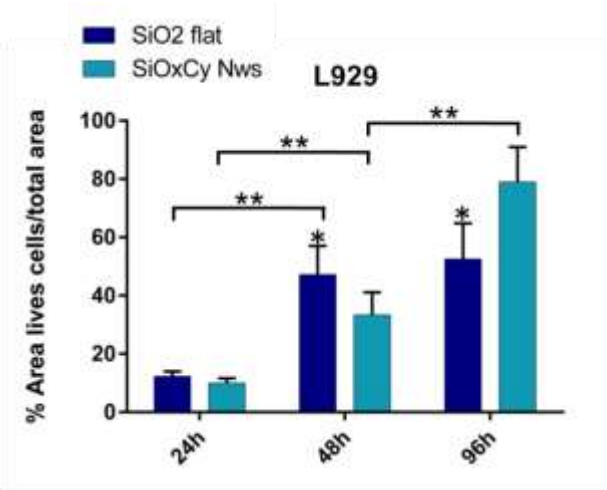


Fig. 25: Histogram quantifying the area occupied by viable cells in the samples from Fig.2. Cells on NWs are more numerous than on control samples by 96 hours. Bars represent mean ± Standard Deviation.

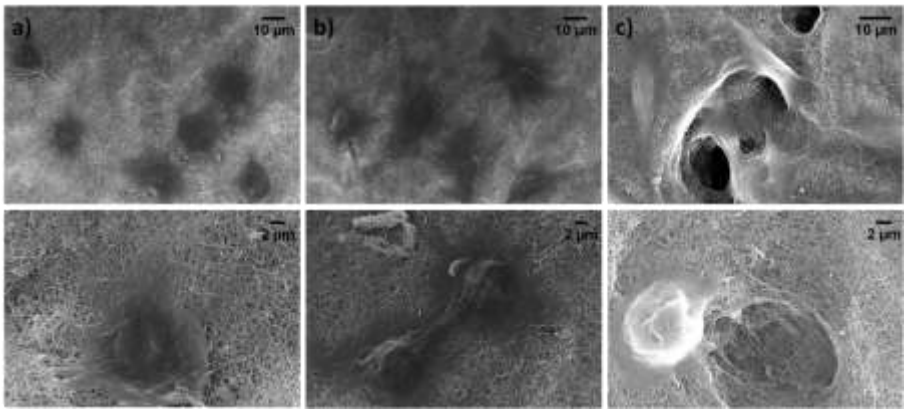


Fig.26: L929 cells on NWs after 24h, 48 and 96h of culture at Scanning Electronic Microscope. Magnification top row= 640 X, bottom row= 1250 X. By 96 hours of culture NWs appeared completely subverted and cells colonised the niches they had created.

Cell shape andspreading were evaluated by SEM images. The interaction between NWs substrate and cells increased over time. Figure 26 shows L929 cells on NWs after 24h, 48 and 96h, figure 26 up shows the overview of cells on the substrate, figure 26 down shows an significantly detail.

In the figure 26a cell shape after 24h is a typically of live and health cells, the detail confirm the overview analysis.

In the figure 26b the number of cells increase after 48h and the shape demonstrate that the cells are health and live.

The figure 26c shows how the cells shape the surface, adapting it and creating an better environment to grow and proliferate, the detail confirm the overview image.

The direct contact test was then performed using the NW samples as platforms for culturing L929 cells.

Fig. 24 shows cell viability at 24h, 48h and 96h after cell seeding on NW

samples. We tested a natively oxidized Si flat sample, as a reference. Based on viability and fluorescence assays, cells appeared more numerous on $SiO_2$ flat samples than on NWs after 24 h and 48h of culture, likely indicating that cell adhesion was more difficult on NWs, however after 96h the growth of the cell are stimulated by the 3 dimensional substrate. In the last years became known that the cells proliferation on the 3 dimensional substrate. The cell attachment and spreading on substrate are mediated by the focal adhesions, highly complex structures which are ligated integrins, transmembrane receptors assembled in clusters. To clustering and focal adhesion formation is important the space between ligated integrins, which is required approximately around of 50–70 nm . Nanotopographies with spacing larger than 100 nm inhibit cell adhesion .The SiOxCy NW diameter is around 100 nm and the distances between nanowires vary from hundreds nm to several microns. Hence, in the first 48h, although integrin clustering may occur on a single nanowire and the 3D structure enacted the proliferation, the microscale focal adhesion assembly can be impaired because of the long distances between nanowires, which can explain why cell attachment is lower on NWs. Fluorescence (Fig 24) clearly shows that cells significantly proliferated by 48 h but after 96h the number of cell rose, as confirmed also by cover area analysis(Fig.25). The SEM images shows how happen on the NW after 96h, the cells reorganized the NWs network, diminishing the space between the ligated integrins, promoting the focal adhesions and consequently increasing the cell proliferations. This proves the ability of fibroblasts to modify the substrate to make it more suitable to their proliferation.

### 3.4 Study of interaction between NWs and Blood or blood components.

To evaluate the interaction between NWs and whole Blood or/and its components we were following the ISO guideline.

The study of these interaction is very important to understand the possible NWs application. The blood response could be predictive of body responses. The platelets activation and the clotting formation are important steps of Acute Inflammatory Response. Inflammation is a physiological function; more specifically it is a healthy action when controlled. Platelets activation is useful to increase tissue regeneration. Platelets activation, by the released growth factors, regulates cell growth and division. For these reasons the materials that stimulate the activation of platelets are suitable to regenerative medicine and tissue engineering and for the same reason are not useful for implantable bioelectrical devices. The activation of platelets and clotting formation creates a capsule on the devices which isolates it the external environment preventing its operability. Consequently only the hemocompatible materials that do not activate blood clotting, are suitable for implantable bioelectrical devices.

#### 3.4.1 ISO 10993 Section 4-Blood Test

The relevant standard for this research, ISO 10993-4, defines blood/ device interaction as any interaction between blood, or blood components, and a device resulting in effects on the blood or on any organ or tissue, or on the device.

When testing a material for its hemocompatibility, several considerations, such as the duration of contact, temperature, sterility, flow conditions, sample collection/storage, enzymes, controls, surface-to-volume ratio, and fluid dynamic conditions (flow rates), among others, have to be taken into account. Tests should be performed with minimal delay, usually within 4 h of blood

withdrawal, since some properties of the blood change rapidly after collection.

table[42]

| Test Category | Method | Comments |
|---|---|---|
| Thrombosis | Adhered platelets, platelet count, leukocytes, aggregates, erythrocytes, fibrin, etc. | Light microscopy or scanning electron microscopy |
| Coagulation | PTT | |
| Hematology | Leukocyte count; hemolysis (plasma hemoglobin) | Hemolysis is performed to measure the red blood cell membrane fragility in contact with materials and devices. |
| Hematology | Leukocyte count and differential; hemolysis (plasma hemoglobin) | Hemolysis screening test is performed because of its measurement of red blood cell membrane fragility in contact with materials and devices. The method used should be one of the normative standard test methods for hemolysis. |
| Immunology | C3a, C5a, TCC, Bb, iC3b, C4d, SC5b-9 | A panel including the last four tests encompasses the various complement activation pathways. |

Table 2. A brief description of different technique recommended to ISO 10993-4. Additionally, in the case of a specific geometry, the ratio of the test parameter to the exposed surface area must be evaluated (concentration per unit volume/cm2).

The use of animal models for screening purposes is encouraged, but the interpretation of the results must be done carefully, considering that results may be different in human models, given the differences in blood reactivity between species, as well as the fact that differences between in vitro and in vivo models will most probably exist. For example in vitro hemocompatibility does not guarantee in vivo hemocompatibility.

ISO 10993-4 provides a test-selection system that is based on clinical concerns. The types of tests required by this standard depend on the blood contact

category of the device or material (external communicating devices—blood path indirect, external communicating devices—circulating blood, and implant devices). For each contact category tests are repeated.

#### 3.4.1.1 Blood interactions

Blood samples were collected from young, healthy, female farm pigs weighting approximately 45 kg, free of hepatitis or other blood borne disease, by routine phlebotomy using blood collection tubes containing 0.105M (3.2%) buffered sodium citrate for anticoagulation. Blood was provided by the University of South Florida's Center for Advanced Medical Learning and Simulation (USF-CAMLS) labs under Institutional Animal Care and Use Committee (IACUC) certification (protocol ID: T IS00000216). Platelet-rich plasma (PRP) was obtained by centrifuging whole blood at 1200 G for 10'; the NW samples were soaked in PRP for 15'. For SEM imaging, the samples were fixed in 4% paraformaldehyde for 30', dehydrated with ethanol at increasing concentrations and finally coated with a few nanometer-thick gold. Platelet shape, indicative of their activation, was examined with the SUPRA40 Zeiss SEM at 20 KeV.

#### 3.4.1.2 Kinetic blood coagulation testing

Kinetic blood coagulation tests evaluated release of hemoglobin by residual erythrocytes that remained free from entrapment during clot formation. Assays were performed by recalcification of anticoagulated whole blood. Samples were placed in 6 well plate and then warmed in waterbath at 37°C for 5 minutes. Three ml of anticoagulated whole blood was dripped onto the surface of NWs and incubated at 37°C for a further 5 minutes, after which

CaCl2 solution (0.2 mol/L) was added to initiate the coagulation cascade (time 0). The multiwells were shaken for 1 minute to mix the CaCl2 uniformly with the blood. Heating of the covered well was continued at 37°C for a predetermined time (10, 20, 30, 40 minutes). At the set time points, the wells were removed from the waterbath and shaken for 10 minutes following addition of 50 mL distilled water to lysate free erythrocytes. The absorbance of the supernatants at 540 nm was determined. Since the signal was derived from free erythrocytes, absorbance was inversely proportional to clot size. The absorbance time curve was constructed using the average values from 3 replicate experiments.

#### 3.4.1.3 P-selectin assay

The samples were pre-warmed at 37°C. PRP (400 µl) was then deposited on the samples with a micropipette and incubated at 37°C for further 60 minutes. PRP was recovered and plasma was separated by centrifugation. Soluble P-selectin was quantified by a specific immunosorbent assay (sP-Selectin ELISA kit, Cusabio, Wuhan, P.R. China) and concentrations were correlated to untreated PRP.

#### 3.4.1.4 Statistical analysis

Data were analysed using Prism 6 (GraphPad, La Jolla, CA, USA). All values are reported as the mean ± Standard Deviation of three repeated experiments. Differences between group means were evaluated with either t Test, one-way ANOVA, or two-way ANOVA statistical tests with Tukey post-test and differences were considered significant when $p<0.05$.

### 3.4.2 Results of interaction study between blood and Si(O,C)NWs

#### 3.4.2.1 SiC NWs and SiC/SiO2 NWs

Hemocompatibility encompasses a variety of events associated with the blood-biomaterial interaction, starting from interaction with platelets. To analyse this process, the NW samples were dipped in Platelet-Rich Plasma and platelets adhering at the surface were then analysed by SEM. Typical SEM images are reported in Figure 21 for core/shell NWs, compared to a flat $SiO_2$ sample, and in Figure 21 for bare SiC NWs, compared to a flat SiC sample (thin film; for both NWs and thin film the SiC polytype is cubic 3C). Platelet activation state resulted material-dependent and nanostructured and bulk materials behaved in the same way. In particular, starry features characteristic of platelets under activation are seen in all oxide-based samples (Fig. 21). On the contrary, the majority of platelets over SiC samples are resting discoid platelets, attesting that the 3C-SiC NWs are, as the bulk material, hemocompatible.

P-selectin release, evaluated by Elisa assay, confirmed these results (Fig. 22), attesting that the maximum release (approximately +80% with respect to the untreated PRP) occurred for the core/shell NWs. On the contrary, 3C-SiC NWs induced, as in the bulk material (3C-SiC film), a definitely lower P-selectin level.

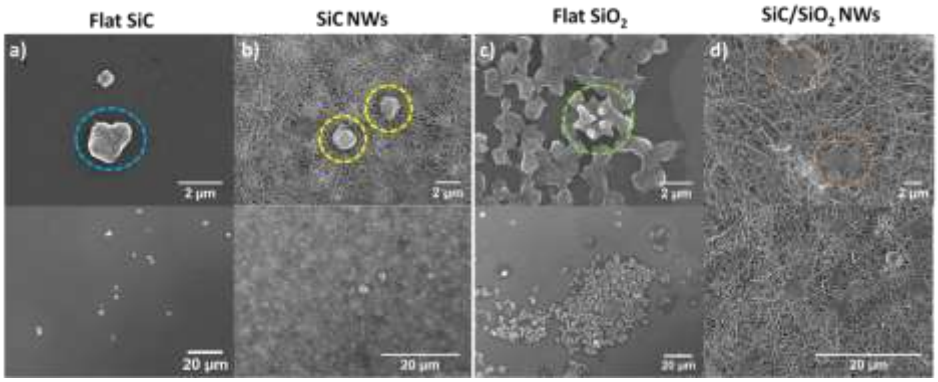


Fig.21: SEM micrographs of platelets (bottom line: overview, top line: detail) on different samples: flat 3C-SiC film (a; platelet circled in cyan), 3C-SiC NWs (b; platelets circled in yellow), flat $SiO_2$ (c; platelet circled in green), and core/shell NWs (b; platelets circled in orange). The starry shape indicates an activation of the platelets.

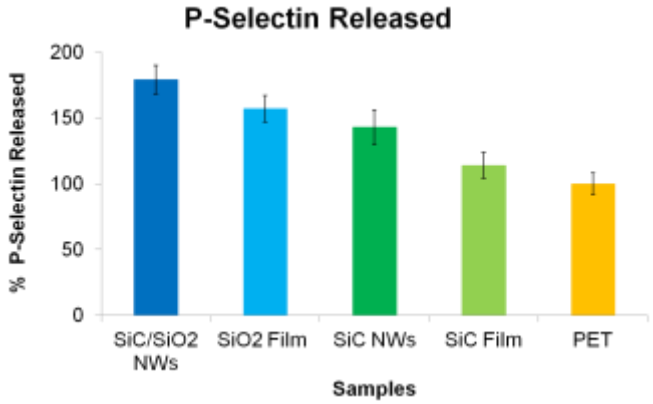


Fig. 22: Platelet activation evaluated through sP-selectin. Soluble P-selectin released by platelets over different nanostructured samples (core/shell and bare NWs), compared with flat $SiO_2$ and 3C-SiC samples. Concentrations were related to untreated PRP (sample value/untreated PRP value)x100(control PET).

### 3.4.2.2 $SiO_xC_y$ NWs

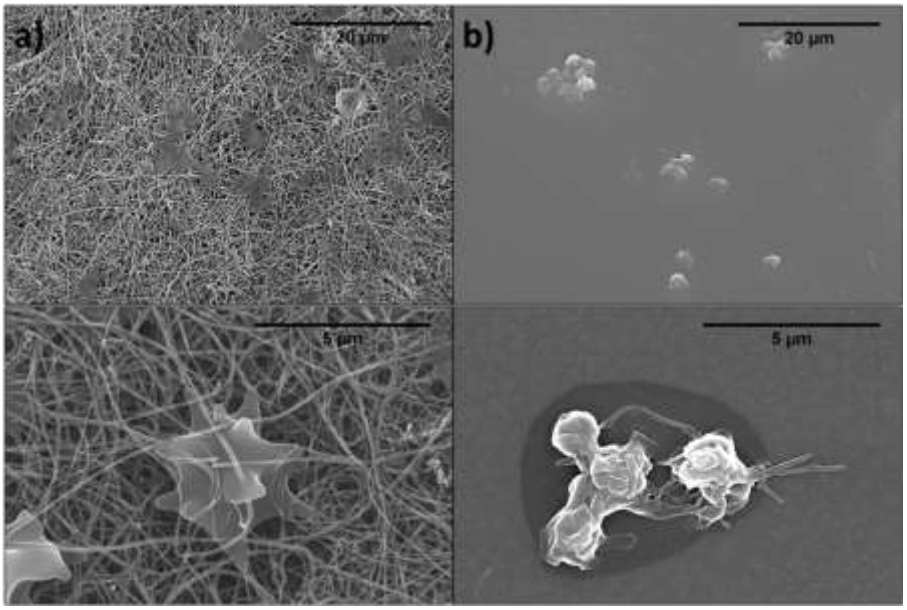


Fig 27 Figure shows SEM microphotographs of platelets on SiOxCy NWs (A) and on flat $SiO_2$ (B). The SEM observation highlighted that platelet activation was comparable on both substrates. In particular, star-like shapes, characteristic of activated platelets were observed in all samples.

The Figure 27 shows the SEM images of platelet on SiOxCy NWs in figure 5a and on $SiO_2$ flat in figure 5b.

The SEM images after platelet fixation are reported in Figure 27 for SiOxCy NWs compared to a flat SiO2 sample. Image analysis shows that platelet activation on nanostructured and bulk materials were quite similar. In particular, star-like shapes (Fig.5a down), characteristic of platelets in activation, and octopus shapes (Fig.27b down), characteristic of activated platelets were observed for both samples surface.

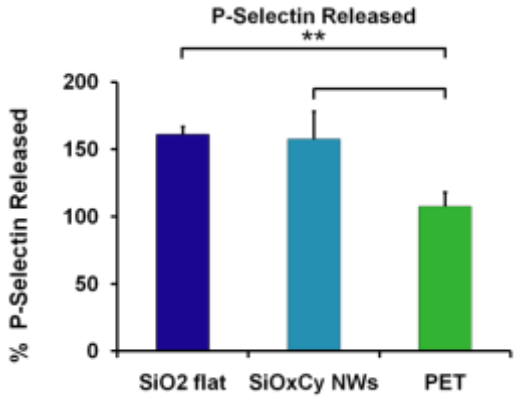


Fig. 28: Graph showing P-selectin release analysis by ELISA assay on PRP on SiOxCy NWs, flat $SiO_2$ or plastic surface. The assay confirms the SEM findings (Fig.6) and shows comparable levels of activation on silicon oxide surfaces.

P-selectin release, evaluated by Elisa assay, was consistent with these results (Fig. 28), attesting that the P-selectin release was major on the oxide materials that on the control (approximately +50% with respect to the untreated PRP).

Kinetic blood coagulation tests evaluated the release of hemoglobin by the residual erythrocytes that remained free from entrapment during clot formation. Assays were performed by recalcification of the anticoagulated whole blood. Samples were placed at the bottoms of 6 well plate and then prewarmed in waterbath at 37°C for 5 minutes.

Three ml of anticoagulated whole blood was dripped onto the surface of NWs and incubated at 37°C for a further 5 minutes, after which CaCl2 solution (0.2 mol/L) was dripped into the blood to initiate the coagulation cascade (time 0). The multiwells were shaken for 1 minute to mix the CaCl2 uniformly with the blood. Heating of the covered well was continued at 37°C for a predetermined time (10, 20, 30, 40 minutes). At the designated termination point, the wells were removed from the waterbath and shaken for 10 minutes following addition of 50 mL distilled water to lyse the free erythrocytes. The absorbance of the supernatants at 540 nm was determined. Since the signal was derived

from that proportion of erythrocytes remaining free of clot entrapment, absorbance was inversely proportional to the size of the clots. The absorbance time curve was constructed using the average values from 3 replicate experiments.

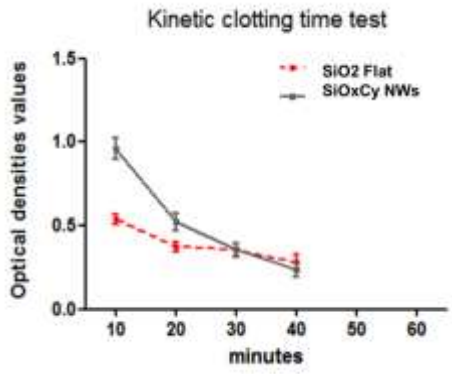


Fig.29 Kinetic clotting reactions suggest different procoagulant propensities for different morphology, flat and NWs. A proportion of the erythrocytes present during the incubation was entrapped during the coagulation.

Erythrocytes remaining in the solution phase were lysed and the absorbance of the released hemoglobin at 540 nm was determined. Absorbance-time was determined for hemoglobin release during kinetic clotting reactions in recalcified whole blood.

Kinetic blood coagulation tests confirm the results. The kinetic blood clotting test in vitro evaluated the contact activation when the sample interacts with blood, i.e. the degree of activation of intrinsic coagulation factors.

The absorbance vs time curve for release of hemoglobin from erythrocytes provided the measure of contact activation. A curve providing a drop slope usually implies high procoagulant properties in the implanted material. Figure 29 shows that the curves for $SiO_2$ flat and $SiO_xC_y$ NWs. The $SiO_2$ flat presenting slow and smooth downward inclination; the $SiO_x$ NWs slope curve is more accentuated, to demonstrate that the clot formation on Nws is favoured, confirming the results of SEM and p-selectine results. The curves converge by the 40-minute time-point.

For implantable devices, the combined cyto- and hemo-compatibility of cubic

SiC NWs makes them a biomaterial of interest for advanced application fields as the brain-machine interface, in line with very recent results demonstrated on 3C-SiC needles . Core/shell and oxycarbide NWs are instead cyto- but not hemo-compatible. They provide a cell growth platform which is biomimetic, since the NW network resembles the biological extra-cellular environment and promotes platelet activation, which is exploitable as implantable biomaterial or for tissue regeneration. Hemocompatibility encompasses a variety of events associated with the blood-biomaterial interaction, starting from interaction with platelets. To analyse this process, the NW samples were dipped in Platelet-Rich Plasma and platelets adhered at the surface were then analysed by SEM. Typical SEM images are reported in Figure 5a for oxycarbide NWs and compared with $SiO_2$ flat in Figure 5b. The SEM platelets observation underlines that the platelet activation state is comparable in both of substrate. In particular, star-like shapes, characteristic of activated platelets were observed in all samples. The P-selectin analysis confirm the SEM (Fig.6) and it shows that the on the oxide major p-selectin are released increasing the mechanism of regenerative tissue.

### 3.5 Summary and conclusive consideration

In this chapter we evaluated the biocompatibility of Si(O,C) NWs. The study were conducted in view of future developments. The NWs were evaluated with the substrate, as a platform, by indirect and direct contact tests according to ISO 10993-5 guidelines and detached to substrate, as a powder. The *in-vitro* tests using different cells lines showed that the Si(O,C) NWs do not release cytotoxic agents, are cytocompatible and suitable to biomedical applications. Hemocompatibility tests with platelet-rich plasma and kinetic blood coagulation tests showed that 3C-SiC NWs are hemocompatible, whereas core/shell and oxycarbide NWs induce platelet activation. These results indicate that the analyzed NW platform are promising as biomaterials to design implantable biomedical devices for brain-machine interface or cardiovascular field, based on bare SiC NWs, or for bone implants and tissue regeneration, based on core/shell and silicon oxycarbide NWs.

**Bibliography**


[1] S. Simovic, N. Ghouchi-Eskandar, A. M. Sinn, D. Losic, and C. A. Prestidge, “Silica materials in drug delivery applications.,” *Curr. Drug Discov. Technol.*, vol. 8, no. 3, pp. 269–276, 2011.

[2] F. PATOLSKY and C. LIEBER, “Nanowire nanosensors,” *Mater. Today*, vol. 8, no. 4, pp. 20–28, 2005.

[3] R. Marches, C. Mikoryak, R.-H. Wang, P. Pantano, R. K. Draper, and E. S. Vitetta, “The importance of cellular internalization of antibody-targeted carbon nanotubes in the photothermal ablation of breast cancer cells,” *Nanotechnology*, vol. 22, no. 9, p. 095101, Mar. 2011.

[4] K. H. Müller, J. Kulkarni, M. Motskin, A. Goode, P. Winship, J. N. Skepper, M. P. Ryan, and A. E. Porter, “pH-Dependent Toxicity of High Aspect Ratio ZnO Nanowires in Macrophages Due to Intracellular Dissolution,” *ACS Nano*, vol. 4, no. 11, pp. 6767–6779, Nov. 2010.

[5] A. Magrez, L. Horváth, R. Smajda, V. Salicio, N. Pasquier, L. Forró, and B. Schwaller, “Cellular toxicity of TiO2-based nanofilaments.,” *ACS Nano*, vol. 3, no. 8, pp. 2274–80, Aug. 2009.

[6] M. Shevach, S. Fleischer, A. Shapira, and T. Dvir, “Gold nanoparticle-decellularized matrix hybrids for cardiac tissue engineering.,” *Nano Lett.*, vol. 14, no. 10, pp. 5792–6, Oct. 2014.

[7] M.-M. Song, W.-J. Song, H. Bi, J. Wang, W.-L. Wu, J. Sun, and M. Yu, “Cytotoxicity and cellular uptake of iron nanowires.,” *Biomaterials*, vol. 31, no. 7, pp. 1509–17, Mar. 2010.

[8] A. P. Richter, J. S. Brown, B. Bharti, A. Wang, S. Gangwal, K. Houck, E. A. Cohen Hubal, V. N. Paunov, S. D. Stoyanov, and O. D. Velev, “An environmentally benign antimicrobial nanoparticle based on a silver-infused lignin core.,” *Nat. Nanotechnol.*, vol. 10, no. 9, pp. 817–823, Jul. 2015.

[9] L. Bareket-Keren and Y. Hanein, “Carbon nanotube-based multi electrode arrays for neuronal interfacing: progress and prospects.,” *Front. Neural Circuits*, vol. 6, p. 122, Jan. 2012.

[10] M. H. Kafshgari, N. H. Voelcker, and F. J. Harding, “Applications of zero-valent silicon nanostructures in biomedicine.,” *Nanomedicine (Lond).*,

vol. 10, no. 16, pp. 2553–71, Aug. 2015.

[11] T. Berthing, S. Bonde, C. B. Sørensen, P. Utko, J. Nygård, and K. L. Martinez, “Intact mammalian cell function on semiconductor nanowire arrays: new perspectives for cell-based biosensing.,” *Small*, vol. 7, no. 5, pp. 640–7, Mar. 2011.

[12] E. Nogueira, C. F. Cruz, A. Loureiro, P. Nogueira, J. Freitas, A. Moreira, A. M. Carmo, A. C. Gomes, A. Preto, and A. Cavaco-Paulo, “Assessment of liposome disruption to quantify drug delivery in vitro.,” *Biochim. Biophys. Acta*, vol. 1858, no. 2, pp. 163–167, Nov. 2015.

[13] Q. Zhou, L. Wang, Z. Cao, X. Zhou, F. Yang, P. Fu, Z. Wang, J. Hu, L. Ding, and W. Jiang, “Dispersion of atmospheric fine particulate matters in simulated lung fluid and their effects on model cell membranes.,” *Sci. Total Environ.*, vol. 542, no. Pt A, pp. 36–43, Oct. 2015.

[14] L. Wayteck, H. Dewitte, L. De Backer, K. Breckpot, J. Demeester, S. C. De Smedt, and K. Raemdonck, “Hitchhiking nanoparticles: Reversible coupling of lipid-based nanoparticles to cytotoxic T lymphocytes,” *Biomaterials*, vol. 77, pp. 243–254, Jan. 2016.

[15] T. Li, S. Murphy, B. Kiselev, K. S. Bakshi, J. Zhang, A. Eltahir, Y. Zhang, Y. Chen, J. Zhu, R. M. Davis, L. A. Madsen, J. R. Morris, D. R. Karolyi, S. M. LaConte, Z. Sheng, and H. C. Dorn, “A New Interleukin-13 Amino-Coated Gadolinium Metallofullerene Nanoparticle for Targeted MRI Detection of Glioblastoma Tumor Cells.,” *J. Am. Chem. Soc.*, vol. 137, no. 24, pp. 7881–8, Jun. 2015.

[16] C. J. Cheng, G. T. Tietjen, J. K. Saucier-Sawyer, and W. M. Saltzman, “A holistic approach to targeting disease with polymeric nanoparticles.,” *Nat. Rev. Drug Discov.*, vol. 14, no. 4, pp. 239–47, Apr. 2015.

[17] R. S. Fernandes, L. G. Mota, A. Kalbasi, M. Moghbel, T. J. Werner, A. Alavi, D. Rubello, V. N. Cardoso, and A. L. B. de Barros, “99mTc-phytate as a diagnostic probe for assessing inflammatory reaction in malignant tumors.,” *Nucl. Med. Commun.*, vol. 36, no. 10, pp. 1042–8, Oct. 2015.

[18] S. J. Soenen, W. J. Parak, J. Rejman, and B. Manshian, “(Intra)cellular stability of inorganic nanoparticles: effects on cytotoxicity, particle functionality, and biomedical applications.,” *Chem. Rev.*, vol. 115, no. 5, pp. 2109–35, Mar. 2015.

[19] G. Villaverde, A. Baeza, G. J. Melen, A. Alfranca, M. Ramirez, and M. Vallet-Regí, “A new targeting agent for the selective drug delivery of

nanocarriers for treating neuroblastoma," *J. Mater. Chem. B*, vol. 3, no. 24, pp. 4831–4842, Jun. 2015.

[20] D. An, J. Su, J. K. Weber, X. Gao, R. Zhou, and J. Li, "A Peptide-Coated Gold Nanocluster Exhibits Unique Behavior in Protein Activity Inhibition.," *J. Am. Chem. Soc.*, vol. 137, no. 26, pp. 8412–8, Jul. 2015.

[21] F. Baldassarre, M. Cacciola, and G. Ciccarella, "A predictive model of iron oxide nanoparticles flocculation tuning Z-potential in aqueous environment for biological application," *J. Nanoparticle Res.*, vol. 17, no. 9, p. 377, Sep. 2015.

[22] M. Xu, J. Qian, A. Suo, T. Liu, X. Liu, and H. Wang, "A reduction-dissociable PEG-b-PGAH-b-PEI triblock copolymer as a vehicle for targeted co-delivery of doxorubicin and P-gp siRNA," *Polym. Chem.*, vol. 6, no. 13, pp. 2445–2456, Mar. 2015.

[23] H. H. Khaligh and I. A. Goldthorpe, "A simple method of growing silver chloride nanocubes on silver nanowires.," *Nanotechnology*, vol. 26, no. 38, p. 381002, Sep. 2015.

[24] F. Wang and J. Liu, "A Stable Lipid/TiO2 Interface with Headgroup-Inversed Phosphocholine and a Comparison with SiO2.," *J. Am. Chem. Soc.*, vol. 137, no. 36, pp. 11736–42, Sep. 2015.

[25] H. M. Khanlou, B. C. Ang, S. Talebian, M. M. Barzani, M. Silakhori, and H. Fauzi, "A systematic study of maghemite/PMMA nano-fibrous composite via an electrospinning process: Synthesis and characterization," *Measurement*, vol. 70, pp. 179–187, Apr. 2015.

[26] A. N. D. Stefanovic, M. M. A. E. Claessens, C. Blum, and V. Subramaniam, "Alpha-synuclein amyloid oligomers act as multivalent nanoparticles to cause hemifusion in negatively charged vesicles.," *Small*, vol. 11, no. 19, pp. 2257–62, May 2015.

[27] X. C. He, M. Lin, F. Li, B. Y. Sha, F. Xu, Z. G. Qu, and L. Wang, "Advances in studies of nanoparticle-biomembrane interactions.," *Nanomedicine (Lond).*, vol. 10, no. 1, pp. 121–41, Jan. 2015.

[28] T. Tolaymat, A. El Badawy, R. Sequeira, and A. Genaidy, "An integrated science-based methodology to assess potential risks and implications of engineered nanomaterials.," *J. Hazard. Mater.*, vol. 298, pp. 270–281, Apr. 2015.

[29] Z. Liu, H. Zhao, L. He, Y. Yao, Y. Zhou, J. Wu, J. Liu, and J. Ding, “Aptamer density dependent cellular uptake of lipid-capped polymer nanoparticles for polyvalent targeted delivery of vinorelbine to cancer cells,” *RSC Adv.*, vol. 5, no. 22, pp. 16931–16939, Feb. 2015.

[30] G. Benedetto, C. G. Vestal, and C. Richardson, “Aptamer-Functionalized Nanoparticles as ‘Smart Bombs’: The Unrealized Potential for Personalized Medicine and Targeted Cancer Treatment.,” *Target. Oncol.*, May 2015.

[31] M. Ulusoy, R. Jonczyk, J.-G. Walter, S. Springer, A. Lavrentieva, F. Stahl, M. Green, and T. Scheper, “Aqueous Synthesis of PEGylated Quantum Dots with Increased Colloidal Stability and Reduced Cytotoxicity.,” *Bioconjug. Chem.*, Nov. 2015.

[32] T. Gao, F. Liu, D. Yang, Y. Yu, Z. Wang, and G. Li, “Assembly of selective biomimetic surface on an electrode surface: a design of nano-bio interface for biosensing.,” *Anal. Chem.*, vol. 87, no. 11, pp. 5683–9, Jun. 2015.

[33] V. Nogueira, I. Lopes, T. A. P. Rocha-Santos, M. G. Rasteiro, N. Abrantes, F. Gonçalves, A. M. V. M. Soares, A. C. Duarte, and R. Pereira, “Assessing the ecotoxicity of metal nano-oxides with potential for wastewater treatment.,” *Environ. Sci. Pollut. Res. Int.*, vol. 22, no. 17, pp. 13212–24, Sep. 2015.

[34] E. Bigaeva, F.-H. Paradis, A. Moquin, B. F. Hales, and D. Maysinger, “Assessment of the developmental toxicity of nanoparticles in an ex vivo 3D model, the murine limb bud culture system.,” *Nanotoxicology*, vol. 9, no. 6, pp. 780–91, Jan. 2015.

[35] F. Schwab, G. Zhai, M. Kern, A. Turner, J. L. Schnoor, and M. R. Wiesner, “Barriers, pathways and processes for uptake, translocation and accumulation of nanomaterials in plants - Critical review.,” *Nanotoxicology*, pp. 1–22, Jun. 2015.

[36] L. A. Ambattu and M. R. Rekha, “Betaine conjugated cationic pullulan as effective gene carrier.,” *Int. J. Biol. Macromol.*, vol. 72, pp. 819–26, Jan. 2015.

[37] G. Plascencia-Villa, D. Torrente, M. Marucho, and M. José-Yacamán, “Biodirected synthesis and nanostructural characterization of anisotropic gold nanoparticles.,” *Langmuir*, vol. 31, no. 11, pp. 3527–36, Mar. 2015.

[38] K. Yamashita, H. Nagai, Y. Kondo, N. Misawa, and S. Toyokuni, “Evaluation of two distinct methods to quantify the uptake of crocidolite fibers by mesothelial cells.,” *J. Clin. Biochem. Nutr.*, vol. 53, no. 1, pp. 27–35, Jul. 2013.

[39] R. M. Zucker, K. M. Daniel, E. J. Massaro, S. J. Karafas, L. L. Degn, and W. K. Boyes, “Detection of silver nanoparticles in cells by flow cytometry using light scatter and far-red fluorescence.,” *Cytometry. A*, vol. 83, no. 10, pp. 962–72, Oct. 2013.

[40] A. Cacchioli, F. Ravanetti, R. Alinovi, S. Pinelli, F. Rossi, M. Negri, E. Bedogni, M. Campanini, M. Galetti, M. Goldoni, P. Lagonegro, R. Alfieri, F. Bigi, and G. Salviati, “Cytocompatibility and cellular internalization mechanisms of SiC/SiO 2 nanowires,” *Nano Lett.*, vol. 14, no. 8, pp. 4368–4375, 2014.

[41] E. K. F. Yim, “Nanotopography-induced changes in focal adhesions, cytoskeletal organization, and mechanical properties of human mesenchymal stem cells,” *Biomaterials*, pp. 1299–1306, 2010.

[42] “ISO 10993-4:2002 - Biological evaluation of medical devices -- Part 4: Selection of tests for interactions with blood.” [Online]. Available: http://www.iso.org/iso/iso_catalogue/catalogue_tc/catalogue_detail.htm?csnumber=32086. [Accessed: 23-Jan-2016].

# CHAPTER 4

# Advanced Multifunctional Materials for Subretinal Implant towards a new generation of Visual Prosthesis

**4.1 Introduction**

Millions of people around the world currently suffer from devastating inherited and acquired forms of blindness, with none or limited treatment options but needing specific attention from governmental agencies, leading to high personal and public resources costs. Retinal degeneration diseases (age-related macular degeneration, retinitis pigmentosa) are mainly due to damages in retinal photoreceptor cells. The retina is composed of brain tissue with cells (rods and cones) in the subretinal part that work as photoreceptors (Fig1). They convert photons in signals, processed by the neural tissues (bipolar cells/ganglion/neuron) in the epiretinal part, then transmitted to the brain. If

photoreceptors are damaged, visual loss occurs but the neuronal circuitries for signal transmission are still efficient.(Fig2)

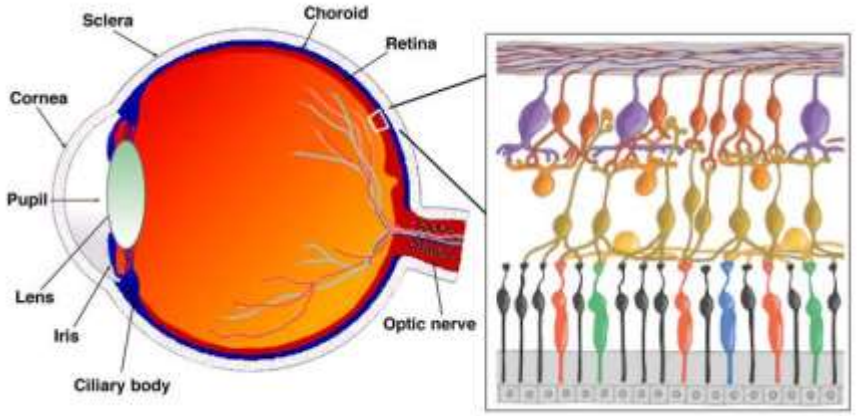


Fig.1:The eye structure, with section of the retina.

To mimic the natural retinal array, we designed a novel subretinal Micro Device (sMD). The devices is based on Si NWs and PEDOT:PSS. It is based on the well know principle of the hybrid ordered bulk heterojunction (OBHJ). The aim is to develop a device based on a well-established photovoltaic technology and to adapt this know-how to the prosthetic field. The hybrid OBHJ is based on a nanowire/organic structure to form a radial p–n junction. In addition the nanowires increase the light absorption by means of light scattering effects. In fact a nanowires based p-n junction allows to increase the light absorption up to the 80%, as previously demonstrated, overcoming the Shockley-Queisser limit of 30 % of a bulk p-n junction. As preliminary studies permissiveness of PEDOT:PSS was evaluated.

## 4.2 Action potential and Signal propagation

### 4.2.1 Phototrasduction

Phototransduction is the process through which the photoreceptors of the retina absorb electromagnetic waves and convert them in the nerve signal. In the retina there are 5 types of cells, including photoreceptors (rods and cones); these contain the photopigment, composed of a protein portion, called opsin, and a chromophore, retinal, isomerization from which to absorption of a photon part of the transduction process, with the activation of the intracellular cascade that determines the onset of a change of the membrane potential. The rods have a single type of opsin, the cones will have three instead. By combining the responses of the three different types of cones it is possible to discriminate different wavelengths and then have a color vision. The rods do not give color vision but instead are photodetector more sensitive than cones and are used in the vision with poor illumiation. Phototransduction gives rise to amplification phenomena which vary in function of the amount of available light, as the photoreceptors modify their sensitivity in relation to the amount of ambient light.

Only the electromagnetic waves with wavelengths that can be absorbed by photopigments evoke a visual sensation. The visible wavelengths goes from slightly less than 400 nm (corresponding to the violet color) to little more than 700 nm (corresponding to the color red). Although humans do not perceive as ultraviolet or infrared light, other species are sensitive to these portions of the electromagnetic spectrum e.g. the insects are sensitive to the wavelengths of ultraviolet and some flowers, which seem to us of uniform color, insects instead appear mottled with veins that link to the area containing the pollen.

### 4.2.2 Transmembrane Potential

Straddling between cell membrane there is a potential difference, called membrane potential (or transmembrane), generally most negative inside that outside of some tens of mV. This potential difference is due to a non-homogeneous distribution of the ions (mainly Na +, K + and Cl-) in the intra- and extracellular compartments, with an accumulation of positive and negative charges inside and outside, in the respect to the total electroneutrality . The excess charge (Q) can be correleted with the potential difference ($V_m$) resulting through a proportionality constant, which represents the membrane capacity ($C_m$):

$$Q = V_m \cdot C_m$$

As it will be explained shortly, the cell membrane is crossed by ionic currents both incoming and outgoing. In order to maintain $V_m$ constant it is therefore necessary to have a gradient in time of the net charge over the membrane, or to keep null the budget of all ionic currents that pass through it. Conversely, if $V_m$ varies with time it means that a charge variation of the membrane occurs, due to a net flow of ionic current.

The lipid composition of the membrane results in insulating behavior. However, the ionic transport is made possible by structures incorporated in the membrane itself: ion channels passively allow the ions transit according to their concentration gradient or electric turn of the channel.

Ion pumps, instead, actively cause the ions passage against their gradient, providing the necessary energy.

The onset of the membrane potential is due to the combined action of its own

channels and ion pumps, and it is very complicated to describe it in details. To understand its origins it may be helpful to consider a simplified, model made only of two ions: a semipermeable membrane, in which the channels are selective for type of a single ion (ion diffusible) and impermeable to the ion of opposite sign (ion indiffusible). Thus placing the membrane in the separation of two regions of the same ionic composition but of different concentration, the gradient pushes the ion diffusible, the only mobile species, to migrate in the region at lower concentration, leaving behind a charge of opposite sign. This generates the electric field at the interface, due to the accumulation of opposite charges at the turn of the membrane, that progressively is prevents the ion transfer. This situation, in the absence of ion pumps, reaches a state of electrochemical equilibrium (Donnan equilibrium) when the electric field and the gradient are balanced. The potential difference that is generated ($E_{ion}$), at constant equilibrium conditions, is solely due to the diffusion of mobile ion and it is linked to the concentrations (C1, C2) via the Nernst equation:

$$E_{ion} = \frac{RT}{zF} \ln \frac{C_1}{C_2}$$

where R is the gas constant, T the temperature, z the charge of the ion and F the Faraday constant.

Adding to the model the action of an ion pump that transports the ion diffusible against its concentration gradient, a contribution $i_{pump}$ to the transport of current towards the more concentrated solution must be considered. It reaches a state of non-equilibrium, but still stable over time (steady state), in which there is maintained a membrane potential which can differ significantly from that predicted by the Nernst equation:

$$V_m = E_{ion} + \left(-\frac{i_i}{g_{ion}}\right)$$

where $g_{ion}$ is the conductance of the membrane (given by the parallel of the

conductance of the individual ion channels) and $-i_i$ is the net ionic current that runs through $g_{ion}$, to form equal to $i_{pumo}$, towards the more concentrated solution.

A possible equivalent circuit is shown schematically in Figure 2:

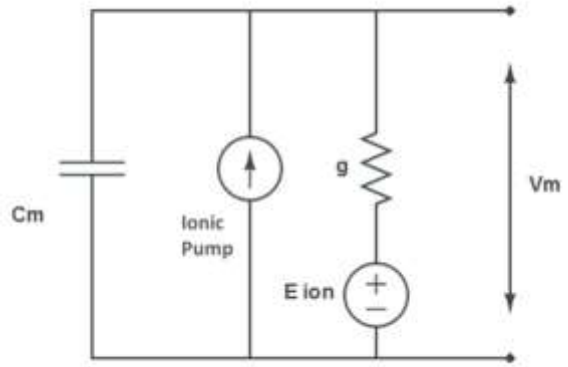


Fig. 2: Circuit board equivalent to a semipermeable cell membrane subjected to the action of an ion pump.

Actually a cell membrane deviates at least in part by this model: it is in fact differently permeable to different ions, which in turn are present in different concentrations in the horse of the membrane, and not all are subjected to the action of Ionic pumps. This simplification is however interesting, as it allows us to understand the origins of $V_m$.

### 4.2.3 The resting membrane potential

The resting potential (or resting voltage) of the cell is the membrane potential that is maintained if there are no action potentials or synaptic potentials present. The intracellular fluid of a neuron at rest is more negatively charged than the extracellular fluid, and this polarity difference is termed the resting potential. The resting membrane potential of a neuron is about ±70 millivolts (mV); this means that the inside of the neuron is 70 mV less than the outside. The disparity between voltages across the cell membrane is due to the fact that there is a higher concentration of positive ions outside the cell than inside the cell. There is approximately 10 times more sodium ($Na^+$ ) on the outside of the cell and approximately 20 times more potassium ($K^+$ ) on the inside. This is frequently called the cell's concentration gradient. The properties of the membrane and the sodium/potassium pump are each partially responsible for the distribution of electrically charged ions. As the membrane is semi-permeable, molecules like water, oxygen, urea and carbon dioxide can cross the cell membrane whereas larger or electrically charged ions and molecules generally cannot. Certain ions, like potassium ($K^+$ ), chloride ($Cl^-$ ) and sodium ($Na^+$ ), pass through the membrane at gates formed by channel proteins which are located in the membrane and regulate how fast the ions can enter. Though drawn to the negative interior of the nerve cell, the $Na^+$ gates are closed until the membrane is depolarized. As a result, there is an increased concentration of $Na^+$ ions outside the membrane. The greater concentration of $K^+$ ions inside the membrane can cross it at a regulated rate by passively diffusing out of the cell, because they are drawn to a region of lesser concentration; they remain, however, held by the negative interior of the cell. $K^+$ ions are returned to the inside of the membrane via the sodium/potassium pump which uses an active

transport system, with energy supplied by adenosine triphosphate (ATP) molecules. Other ions with negative charge, such as chloride, also cross the membrane at a controlled rate; these help in maintaining the negative interior. As a result, the resting potential is sustained by Na+ being held out of the cell, while K+ diffuses out, only to be brought back into the cell. Three Na+ ions are actively removed from the cell by the sodium/potassium pump for every two K+ ions that are allowed to enter.

### 4.2.4 The Action potential and Nerve Impulse

The membrane resting potential is present when a neuron is at rest. However, when our nervous system transmits information, an action potential or a nerve impulse occurs. An action potential is a short-term event in which the electrical membrane potential of a cell rapidly increases and falls. Positive ions flowing into the cell will reduce the negative charge and thus reduce the charge across the entire membrane; we refer to this as depolarisation. When depolarisation gets to around –55 mV (the tipping point) a neuron will give off an action potential. No action potential will fire if the neuron does not reach the threshold level. Once the threshold value is reached, an action potential of a fixed size will always fire; and for any given neuron, the size of the action potential is always the same. Often this is referred to as the all-or-nothing principle. The exchange of ions across the neuron membrane causes nerve impulses or action potentials to take place. A stimulus, for example at the touch receptors, first causes Na channels to open, and because there are many more Na ions on the outside, and the inside of the neuron is negative relative to the outside, Na enters the neuron. Thus, the neuron becomes both more positive and depolarised. Then K channels open (they take a bit more time

than Na channels) and K rushes out of the cell, reversing the depolarisation. When Na enters, the membrane potential increases, and when K exits, it drops sharply back down, giving rise to the alternative name for this potential: the spike potential. Na channels then start to go back to their normal closed state, which causes the action potential to revert towards –70 mV (a repolarisation). However, the membrane potential actually moves past –70 mV to nearly –80 mV (a hyperpolarisation) due to the K channels remaining open just a bit too long. Ion concentrations will steadily return to the resting membrane, and the cell will return to –70 mV. For a short period in the middle of the action potential, the neuron is totally resistant to additional stimulation. This is known as the absolute refractory period, where the neuron cannot make another action potential. The absolute refractory period precedes another brief period, known as the relative refractory period, during which the neuron can generate another action potential but the stimulus must be of greater intensity than normal (Figure 3).[1]

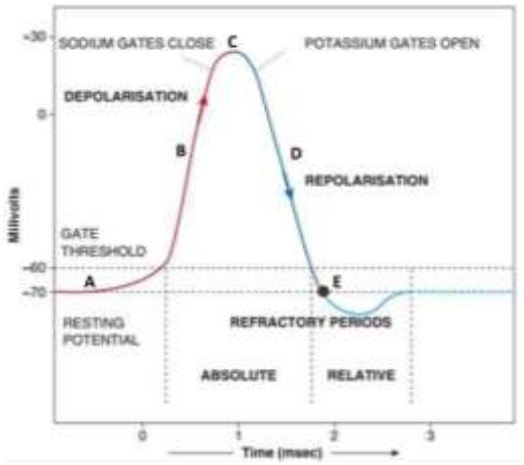


Fig. 3 The action potential A) Resting phase: the neuron is in rest and the membrane is in resting potential B) Depolarisation phase: neuron gives off an action potential, the gates are open. C) Plateaus: the $Na^+$ gates reach saturation and starting to closed, starting to open the $K^+$ gates. D) Repolarisation phase: the $K^+$ gates are open, the Trans-membrane potential decrease. E) Refractory Period: period where the neuron cannot make another action potential.

## 4.3 Retina

### 4.3.1 Retinal cells

In the retina, there are 5 types of cells: photoreceptors (rods and cones, for a total of about 125 million photoreceptors), bipolar cells, horizontal cells, amacrine cells and ganglion cells. In the direct way of transmitting information, the photoreceptors are synaptically connected with the bipolar cells, which in turn transmit the information to the ganglion cells. The horizontal cells mediate lateral inhibition of interactions between photoreceptors and amacrine cells modulate the signal transmission between bipolar cells and ganglion cells. The light, crossing through the retina, reaches the photoreceptor layer after, with the exception of the fovea. In the fovea other retinal cells are withdrawn, leaving exposed only the photoreceptors. The axons of the retinal ganglion cells converge at a point said papilla and from there come out from the eye, forming the optic nerve. The regions of the photoreceptors that contain the photopigments, ie molecules which have the function of absorbing light, are in the outer segment, cylindrical in the rods and pointed in the cones. The outer segment contains folds of the plasma membrane that increase the surface useful for the absorption of light, and that in the rods become true discs, separated by the plasma membrane and densely stacked. The molecules of photopigments are located on the membrane of these foldings / discs and are very large number (up to 109 molecules of photopigment in a single rod).

### 4.3.2 Retinal degeneration

Several patients candidates to receive implants prosthetic retina type suffer from a disease called retinitis pigmentosa (RP). Initially, this causes damage to the rods (Figure 4), which is manifested by the loss of night vision, and then progress to a gradual reduction of peripheral vision that narrows the field of view (so-called visual field tubular). In the final stage we are witnessing an almost complete degeneration of photoreceptors: for patients suffering from advanced RP, a prosthesis can directly excite the remaining retinal neurons and may be the only option available to stimulate the feeling of light.

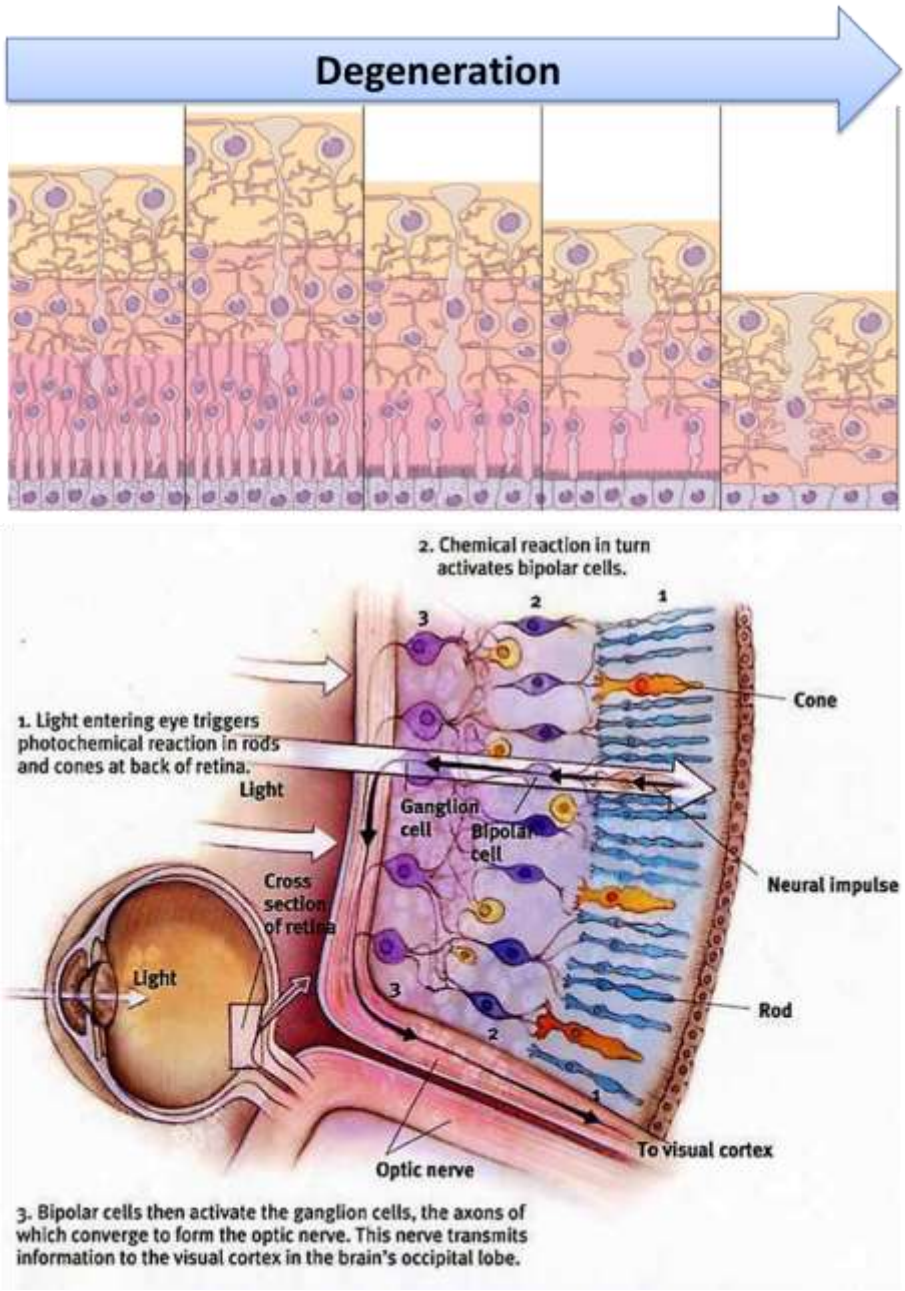


Fig. 4 Top ) The image shows, following the arrow direction, the retinal degeneration from healthy retinal to the complete degeneration of photoreceptor. Bottom) Eye structure and schematic explanation of sight mechanism.

Since this type of prosthesis may also benefit patients with macular degeneration final stadium, while for diseases involving extensive damage of the optic nerve is not necessary to resort to approaches retinal (cortical prosthesis and optic nerve) .

## 4.4 Retinal Devices

### 4.4.1 State of art

Among new therapies, gene replacement is promising [2], but requires at least some survived photoreceptors. The possibility to impart light sensitivity to retinal neurons has been proposed [3], as well as to transplant human embryonic stem cells into the subretinal space[4], but several problems are still to be solved.

The stimulation of the neuronal tissues with electrical impulses originating from epiretinal and subretinal visual prosthesis, like electronic chips, has received great attention in the last years. Taking advantage of the additional processing and cellular connections of retinal neurons, subretinal application would be expected to provide more visual detail as well as better retinotopic correspondence than epiretinal placement. Two subretinally applied chips requiring external devices and/or power supply, the ARGUS II (Second Sight) and the Alpha IMS (Retina Implant), have a fair amount of human patient experience. The stimulation of neurons by microphotodiode array with silicon photovoltaic cells has been tested[5], paving the way for the use of non-power supplied implant. Finally, the use of photoactive flexible polymers to photostimulate neurons is another promising approach[6].

All these prosthesis have detectors in the micrometric scale, at least 2-3 order of magnitude larger than in natural photoreceptors, thus reducing visual spatial resolution and acuity (highest value in patient with a retinal implant is about 0.02µm). Moreover, rigid detectors based on silicon technology lead to a limited achievable visual field, and the use of non biocompatible materials remains a significant hurdle.

This chapter shows the steps made to conceive a new generation of subretinal implant. This microdevice is based on materials properties at the nanoscale and technological knowledge for microdevices designing. The proof-of-concept is achieved by a comprehensive analysis of the organic tissue/inorganic interface, from the compatibility of the neuronal cells to the evidence of signal transmission.

<u>The main improvements with respect to other subretinal devices are:</u>

- Higher spatial density of photosensitive/stimulating elements, comparable to natural retina, leading to a good spatial resolution and acceptable visual acuity for Patients
- Higher retinal area coverage: by implanting several devices, it will be possible to cover a very large part of retina, close to the extension of the natural photosensitive eye area
- Promising long-term biocompatibility, that will be tested here with extensive assays with cellular and tissue models
- Stand-alone device, without external parts or power supply
- Grey scale vision, with possible color recognition with specific organic absorbers.

### 4.4.2 Subretinal Micro Device design

The main goal of this thesis project was to realize a subretinal implantable prototype based on a nano-on-micro technology developed on flexible polymers.

The subretinal microdevices (sMD) developed is based on a Ordered Bulk HeteroJunction (OBHJ). The sMD is developed based on a well-established photovoltaic technology [7]and adapting this know-how to the prosthetic field. Different inorganic materials are taken into account in order to grow the nanowires considering different advantages and drawbacks, and finally the choice fell on silicon NWs.

The main advantage of silicon is its wide absorption range in the visible spectra while its drawback is its short lifetime when placed in biological media.

The system works thanks to the inorganic/organic materials band alignment. In fact the highest occupied molecular orbital of organic semiconductor, i.e. poly(3,4-ethylenedioxythiophene):poly(styrene sulfonate)(PEDOT:PSS), is positioned to inject holes into the electrolyte and hence into neuronal cells. The lowest unoccupied molecular orbital of organic semiconductor is well above the Fermi level of the n-type NWs, and then electron collection occur efficiently at the silicon interface. Different organic semiconductors are used in the framework of the optimization of the sMD, on the base of the optical (absorbance) and electrical (mobility) properties of the different materials. The material used as organic semiconductor is PEDOT:PSS.

The organic semiconductor penetrates between the NWs to form the radial p–n junction which is the core of an ordered bulk heterojunction (OBHJ).

A network of NWs fixed on a 1x1 $\mu m^2$ Si base is a single active modulus, anchored to a conductive polymer that can hold a matrix of these modules (Fig.3). The final overall sMD dimensions of 200x200 $\mu m^2$ enable to implant several sMDs on a large retina's area, with improved visual resolution and vision field. The polymer will enable the grounding of all NWs.

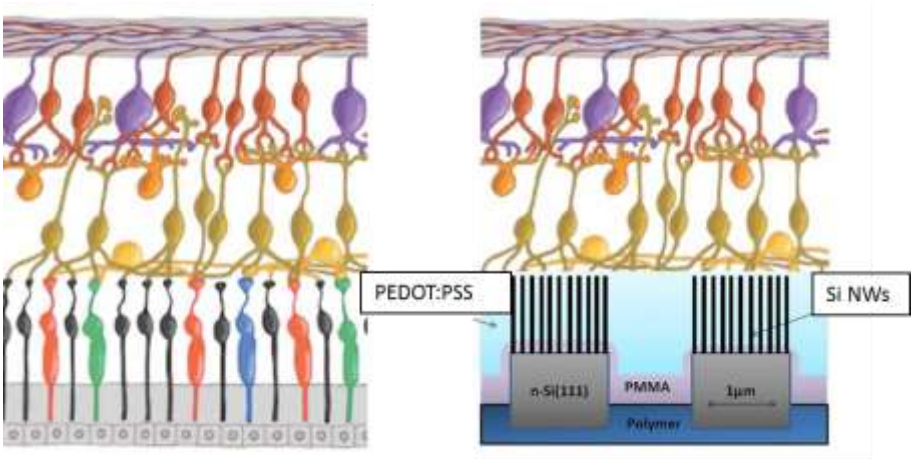


Fig 5: Comparison between the typical retina scheme and the proposed subretinal prosthetic Micro-Devices(sMD)

### 4.4.3 Ordered bulk heterojunction

The hybrid OBHJ are based on nanowire/organic structure to form radial p–n junction. In addition, the nanowires network increases the light absorption by means of light scattering effect: nanowires based p-n junction allows to increase the light absorption up to the 80%, as previously demonstrated [8]overcoming the Shockley-Quissier limits of 30 % of a bulk p-n junction.

OBHJ based solar cells differ from conventional inorganic solar cells in the carrier generation and collection mechanisms. In an excitonic solar cell, the majority of photon absorption takes place in one component, termed the donor. The second component is the acceptor, which provides the band offset

needed for charge separation and may also absorb light. Nanostructured acceptor materials (Fig. 6) allow the generation and collection processes to be orthogonalized; by absorbing light in the vertical direction and collecting carriers laterally, thick films can be used to absorb more incident light without having donor domains with dimensions larger than the depletion width.

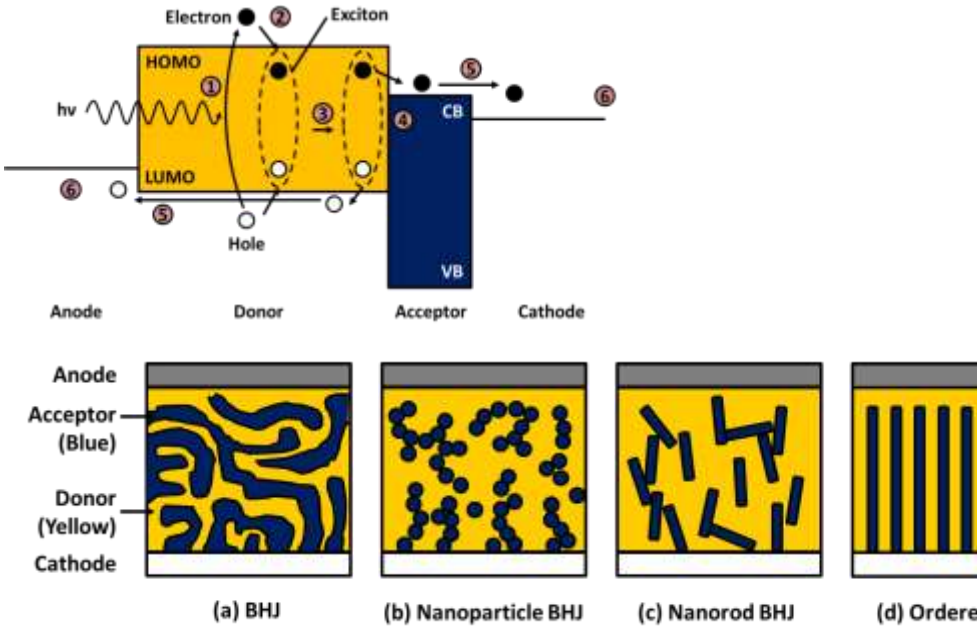


Fig.6: Schematic flat-band diagram of charge generation and extraction processes in an excitonic PV device(up), Inorganic semiconductor morphologies in BHJ architecture

The individual charge transfer processes taking place in an excitonic PV are shown in Figure 6. Following photoexcitation of an electron across the bandgap of the donor (1), the polaron pair thermalizes down to the bandgap and forms an exciton (2). The exciton diffuses (3) with a characteristic diffusion length L; it can undergo charge separation (4) if a donor-acceptor interface exists within this distance. Charge carriers are then transported (5) through the

donor/acceptor bulk and eventually transferred to the electrodes (6) for conveyance to the external load circuit. Each charge generation and extraction process has a characteristic rate and efficiency; the external quantum efficiency (EQE) is the product of all the individual process efficiencies.

The charge is collected by each single nanowires since an electrical impulse is transmitted to the neuronal network once a critical voltage threshold is reached, proportionally to the light intensity. The nanowire/organic hybrid structure discharges and transmit an impulse at a voltage threshold of about 50mV to the neuronal cells.

### 4.4.4 Fabrication methods

As explain above, the sMD is based on OBHJ with PEDOT:PSS and Si NWs. In this paragraph the sMD production methods are explained step by step (Fig.7)

The Si NWs can be grown by the Vapor-Liquid-Solid (VLS) mechanism using a induction heated Vapor Phase Epitaxy (VPE) reactor at low pressure, by using silane as precursor, hydrogen as carrier gas and gold as catalyst.

For the VPE growth, a preheating of the gold-deposited substrate was performed at 700°C in order to get catalyst dewetting, then the temperature was set to 550°C and the reagents were introduced into the growth chamber. Si NWs show a good alignment along the (111) direction due to the homoepitaxy on a silicon substrate (the details of NWs growth are explained in the chapter 2).

The NWs are coated with polymethyl methacrylate (PMMA). The polymer was deposited by spin-coating with a commercial system (WS-400-6-NPP-Lite-AS). The PMMA is a material particularly suitable for this purpose, as it is transparent in the visible and has a high electrical resistivity (1019 Ω). At room

temperature it is presented also in glassy form, with the relative transition temperature (Tg) at 105 ° C, and is generally soluble in esters, ketones, aromatic compounds and glycols ethers.[9]

Finally, the PMMA is biocompatible, finding use mainly as a bone cement in orthopedic prostheses and in the field of ophthalmology, where, in addition to its use in the manufacturing of contact lenses, it is used to produce intraocular lenses for the treatment of cataract.[10]

In particular, PMMA with an average molecular weight Mw ~ 350000 (Sigma Aldrich) was used in this work. The NWs surface were covered with PMMA 15 wt% and the spin coating process are performed at 1000 rpm for 60 seconds. Finally, the samples were heated at 60°C for 30 minutes.

The PMMA was used to isolate the Si substrate and any residue of the catalyst remaining after growth. To form the radial p–n junction the NWs's heads were coated with PEDOT:PSS. To expose the NW's heads the PMMA were etched by Reaction Ion Etching (RIE Plasmafab 340), the procedure were performed in plasma oxygen for 90 seconds at 60.4 mTorr and 50 mW.

PEDOT:PSS, type Clevios PH1000was purchased from Heraeus Conductive Polymers Division. Successively PEDOT:PSS solution was firstly doped with a 0.05 vol. of dodecyl benzene sulfonic acid (DBSA) surfactant (Sigma Aldrich) for efficient film forming, then 3% v/v concentration of EG were added to enhance electrical conductivity with respect to the pristine state[11,12]. Homogeneous PEDOT:PSS films was spinned on sMD at 1500 RPM for 30 s. The final films thickness was around 80 nm, as measured with the profilometer[13]. sMD were finally baked on a hot plate at 140°C for 60 min. The PEDOT:PSS are deposited by spin-coating.

The contacts were realized by electron beam metallizer Edwards Auto 306, obtaining a final thickness of to 375 nm, measured by the quartz microbalance

integrated in the evaporator itself.

All steps were examined by SEM

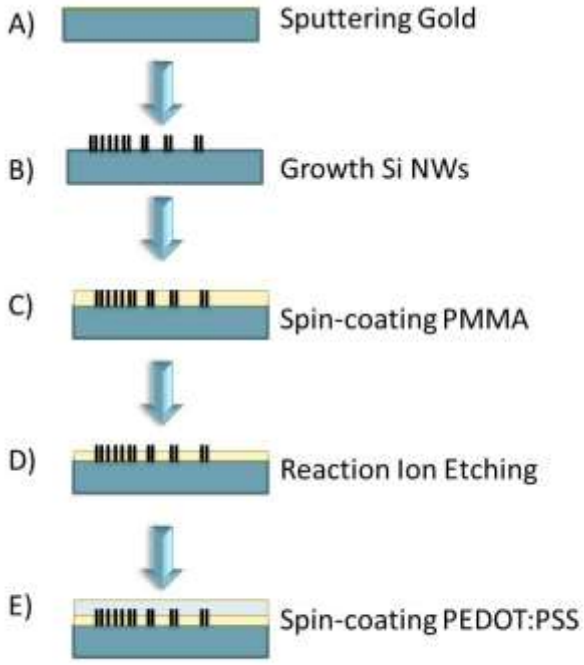


Fig. 7: represent schematically the production methods used for sMD. A) nanometric gold film was deposited by sputtering on silicon substrate, B) Si NWs are growth by CVD system. C) PMMA was deposited on NWs substrate by spin-coating D) PMMA is etched by RIE, exposing the NWs's heads. E) the PEDOT:PSS is deposited by spin coating.

### 4.4.5 Electrical characterization

The sMD operating principle is based on the photovoltaic effect of the ordered bulk heterojunction. Therefore we first tested the photovoltaic performance of the devices, performing I-V characteristics under illumination. This characterization is useful also to evaluate the photovoltaic parameters of the sMD, as the open circuit voltage and the short-circuit current, in order to compare these parameters to the neural action potential. The sMD must be designed in order to a comparable open circuit voltage to the neural action potential for not damaging the neural cells during the light transduction. In particular the photovoltaic parameters are obtained by comparing the I-V characteristics in dark and under illumination of a 1.5 suns. In addition we compare two different front Ohmic contact configurations:

1) Depositing a gold contact and measuring the I-V characteristics in air.

2) Using an electrochemical contact based on PBS (phosphate buffer saline), a ionic solution comparable with biological environment.

Figure 8 shows the schematic representation of system used and the I-V characteristics of sMD.

The I-V characteristics under illumination shows that the $V_{OC}$ is 125 mV and the short circuit current is 0.4 mA.

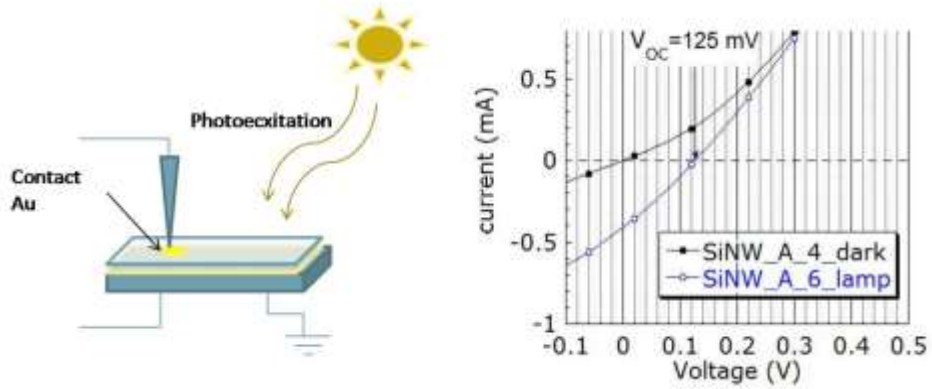


Fig. 7: Left) the image shows the schematic representation of system used and the I-V characteristics of sMD contacted thought gold contact right) I-V characteristics

Figure 8 shows the schematic representation of system used and the I-V characteristics of sMD using the electrochemical Ohmic contact with gold contact and in direct contact with PEDOT:PSS.

The I-V characteristics reveal that the $I_{sc}$ is comparable in both the analyses ($I_{sc}$=0.5 μA) but it is three orders of magnitude lower than the current measured in air. This effect is probably due to the low concentration of ions available in the PBS solution or to a lower efficiency of the electrochemical contact. It is worth noting that this $I_{sc}$ decrease is beneficial for the sMD, because the $I_{sc}$ measured in air was too high and it can damage the neurons if placed in direct contact with these cells.

In addition, the comparison of the I-V characteristics with the gold contact and in direct contact with PEDOT:PSS reveals that the $V_{oc}$ slightly changes. In fact the $V_{oc}$ is 230 mV and 190 mV in the case of PBS in direct contact with the PEDOT:PSS and with the gold contact respectively. This effect can be explained in the perspective of the high porosity of the PEDOT:PSS polymer. In fact the polymer porosity increases the efficiency of the ionic exchange with the PBS solution, increasing the sMD photovoltaic performance. However both the $V_{oc}$

are comparable with the neural acition potential, making these devices suitable for the retinal prostetics.

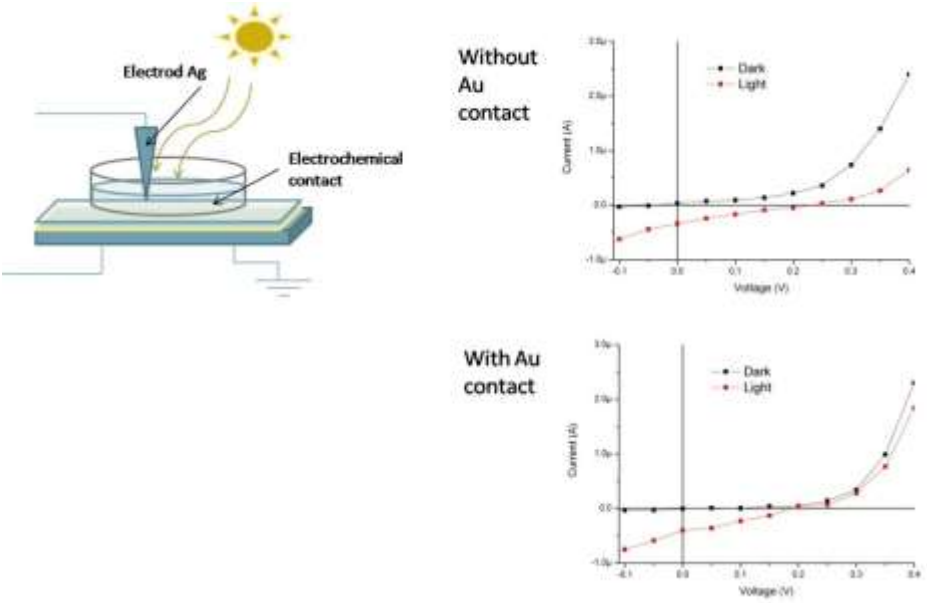


Fig. 8 Left) the image shows the schematic representation of system used and the I-V characteristics of sMD using the electrochemical Ohmic contact with gold contact and in direct contact with PEDOT:PSS. Right) I-V characteristics contact with gold contact and in direct contact with PEDOT:PSS

| | Voc | Isc |
|---|---|---|
| Gold contact in air | 125 mV | 0.5 mA |
| Gold contact in PBS | 190 mV | 0.4 ?A |
| PBS Direct contact with PEDOT:PSS | 230 mV | 0.3 ?A |

Table 1 resumes the photovoltaic parameters of the sMD test devices under different configurations of the front contact.

All sMD materials used must be biocompatible. Preliminary tests on PEDOT:PSS were performed with the collaboration with SISSA of Trieste and University of Trieste in order to evaluate the biocompatibility and the neural growth and will be shown in the next paragraph..

**4.5 Preliminary test**

The perspective of using different materials in developing a new-generation of subretinal devices interfaces urges to tune, assess and validate them in biological microenvironment. The evaluation of NWs was shown in chapter 2 and here the permissiveness of PEDOT:PSS will be evaluated

The development of conductive polymers, finely tailored in their physical-chemical properties, paves the way to the design with improved adaptability to the brain tissue and increased charge-transfer efficiency when recording/stimulating neurons. To this end we interfaced PEDOT:PSS doped with different amounts of ethylene glycol (EG) with rat hippocampal primary cultures grown for 3 weeks on the synthetic substrates. We used immunofluorescence and scanning electron microscopy combined to single cell electrophysiology to further study and show the biocompatibility of PEDOT:PSS, demonstrating their permissivity as substrates for neuronal growth as well as for synapse formation and maturation, assessed in terms of cell morphology, density and electrical activity. In the same cultures, glial cells growth was instead progressively inhibited, hinting at the ability of the material to down regulate glial reaction. Such properties make PEDOT:PSS a suitable candidate for the design of new implantable devices, depressing the glial reactivity to the presence of a foreign body without affecting neuronal viability and functionality.

In this paragraph, we further investigate the biocompatibility of PEDOT:PSS as substrates for long-term survival of hippocampal cultures, in the perspective of exploiting such materials for implantable subretinal devices. Implantable devices should be covered with highly conductive and biocompatible materials, to reduce any damage due to high voltage signal delivery,to reduce

at the minimum the glial reactions to the implants[14] and maintain their functionalities in time. For these reasons, we tested layers of PEDOT:PSS doped with different concentration of EG (0%, 1% and 3%), which has been reported to increase electrical properties of conductive polymers. [11,12]
We describe that EG not only affects the conductivity of the layers, but also improves other important factors, including wettability and roughness, and selectively reduces glial cell reaction. Remarkably, neuronal maturation, synapse formation and function are unaltered by the manufactured substrates.

### 4.5.1 Sample preparation and methods of characterization used

#### 4.5.1.1 Preparation of PEDOT:PSS layers

Poly(3,4-ethylenedioxythiophene):poly(styrene sulfonate), termed PEDOT:PSS, type Clevios PH1000was purchased from Heraeus Conductive Polymers Division.
Successively PEDOT:PSS solution was firstly doped with a 0.05 vol. of dodecyl benzene sulfonic acid (DBSA) surfactant (Sigma Aldrich) for efficient film forming, then different concentrations v/v (0%, 1% and 3%) of EG were added to enhance electrical conductivity with respect to the pristine.[11,12] One solution was prepared without EG addition and used as reference control.
Homogeneous PEDOT:PSS films at different EG concentrations were spinned on a glass slides of 1x3 cm at 1500 RPM for 30 s. The final films thickness was around 80 nm, as measured with the profilometer.[13] Slides were finally baked on a hot plate at 140°C for 60 min.

#### 4.5.1.2 Electrical Characterization of PEDOT:PSS layers

Electrical measurements of PEDOT:PSS layer were obtained by a source/measure precision unit (Agilent B2902A) and controlled by homemade LabView software. The I-V characteristics were acquired by spanning the applied voltage from -1 V to +1 V achieved in 0.1 V steps and recording the resulting current flowing in the PEDOT:PSS layer. Different measurements were realized with different EG doping levels of PEDOT:PSS.

#### 4.5.1.3 Contact angle

5 μl of water were dropped on the surfaces and the images were captured using a homemade contact angle measuring system . The contact angle was evaluated by a statistical study of several images: two layers where investigated for each EG concentration and the measurement were repeated three times for each sample.

#### 4.5.1.4 Atomic Force Microscopy (AFM)

AFM was used for studying at high-resolution the three-dimensional reconstructions of PEDOT:PSS layers at three different EG doping conditions (0%, 1% and 3%). All AFM images were acquired using a commercially available microscope (Solver Pro AFM from NT-MDT – NT-MDT Co. – Moscow – Russia) endowed with a closed-loop scanner. Measurements were carried out in air at room temperature working in dynamic mode. Cantilevers, characterized by a resonant frequency of 90 kHz and a force constant of 1.74 nN/nm (NSG03 series from NT-MDT – NT-MDT Co. – Moscow – Russia) were used working at low oscillation amplitudes with half free-amplitude set point. High-resolution

images were 512×512 pixels frames acquired at 1 lines/second scan speed working in air. All AFM data were analyzed using Gwyddion,[15] scanning probe microsopy data analysis free software. Surface roughness was computed as the root-mean-square (RMS) value of the height irregularities of AFM images. The ratio between the surface area and the projected surface area, $S_r$, was computed from AFM images by simple triangulation and correlated to roughness values.

#### 4.5.1.5 Ethical approval

All experiments were performed in accordance with the European Community Council Directive of 24 November 1986 (86/609EEC) and Italian law (decree 26/14) and were approved by local Authority Veterinary Service.
Animals were hosted by the University of Trieste Animal Facility (Life Sciences Department, Italy, authorized by the Italian Ministry of Health) and breeding conditions and procedures complied with the 2010/63/UE EU guidelines and Italian law (26/14).
Neonatal rats were sacrificed by rapid decapitation and the tissue of interest (hippocampus) harvested, all efforts were made to minimize suffering. The work was performed on explanted tissue and did not require ethical approval.

#### 4.5.1.6 Cultures and immunofluorescence

Hippocampal neurons were isolated from postnatal (P2-3) rat pups as previously reported. [16]
Cells were plated on polyornhitine covered glass (control cultures) or PEDOT:PSS (with different concentrations of EG) coverslips. Neurons were seeded on control and PEDOT:PSS layers with a standard amount of cells

(~150000 cells/coverslips). PEDOT:PSS layers were pretreated with plasma cleaning and covered with a poly-ornhitine layer to increase permissiveness of surfaces. Cultured cells were used for experiments at 8–22 days in vitro.

To quantify neuronal and glial cells density, cultures (control and PEDOT:PSS) were immunostained following the procedure previously described[17]. Briefly, cultures were fixed with 4% paraformaldehyde in PBS (20 min), then, upon washout in PBS, incubated in blocking solution and subsequently incubated with rabbit polyclonal antibody against β tubulin III (1:250 dilution; Sigma-Aldrich) and mouse monoclonal antibody against GFAP (1:200 dilution; Sigma-Aldrich). Upon washout in PBS, cultures were incubated with the secondary goat anti-rabbit Alexa Fluor 594 (1:500, Invitrogen) and goat anti-mouse Alexa Fluor 488 (1:500, Invitrogen). Two culture series (4 fields for each slide) were sampled for each condition. Samples were visualized with a Leica DM 6000 microscope at 20x magnification. Offline analysis of the images was performed with the open source image-processing package Fiji.

The content of GFAP was estimated by selecting squared areas (25 $\mu m^2$) close to the nucleus in randomly chosen glial cells. The mean intensity of fluorescence within this region was calculated using dedicated tool of Fiji software. Background fluorescence, measured in region of sample without cells, was subtracted from fluorescence values.[18] Area of single glial cells was automatically measured by the software in randomly selected cells, sufficiently isolated from neighbors, whose perimeter was manually drawn.

#### 4.5.1.7 Scanning electron microscopy (SEM)

Scanning electron microscopy (SEM) was used to investigate the morphology of cellular cultures developed on PEDOT:PSS substrates and on controls.

Images were acquired collecting secondary electrons on a Gemini SUPRA 40SEM (Carl Zeiss NTS GmbH, Oberkochen, Germany) working at an acceleration voltage of 5 keV. Before SEM characterization cellular samples were washed with 0.1 M cacodylate buffer (pH = 7.2) and fixed with a solution containing 2 % glutaraldehyde (Fluka, Italy) in 0.1 M cacodylate buffer for 1 h at RT. Cultures were then washed in a cacodylate buffer and dehydrated by dipping in water/ethanol solutions at progressively higher alcohol concentrations (50%, 75%, 90%, 95%, 98% and 100% ethanol for 10 minutes each). Afterwards the samples were left in 100% ethanol to dry at 4 °C overnight. Prior to SEM imaging samples were gold metalized in a metal sputter coater (Polaron SC7620).

#### 4.5.1.8 Electrophysiology

A patch-clamp amplifier (multiclamp 700b, Axon Instruments, Sunnyvale, CA, USA) was used to record visually identified neurons (with an upright microscope equipped with differential interference contrast optics and infrared video camera), using the patch-clamp technique in voltage and current modes. Whole-cell recordings were obtained with pipettes (4–7 MΩ, Hingelberg, Malsfeld, Germany) containing 120 mM K gluconate, 20 mM KCl, 10 mM HEPES, 10 mM EGTA, 2 mM $MgCl_2$ and 2 mM $Na_2ATP$ (pH 7.35 adding KOH). The external solution contained the following: 150 mm NaCl, 4 mm KCl, 1 mm $MgCl_2$, 2 mm $CaCl_2$, 10 mm HEPES, 10 mm glucose, pH 7.4. All experiments were performed at 18–22°C.

Liquid junction potential was 13 mV; membrane potential values were not corrected for it. All recordings were performed at -58 mV of holding potential. Cells exhibiting > 15% changes in either series resistance or holding were

excluded from the analysis. The series resistance was < 20 MΩ and it was not compensated.

#### 4.5.1.9 Data analysis

Data were transferred to a computer hard disk after digitization with an A/D converter (Digidata 1322, Molecular Devices). Data acquisition (digitized at 10 kHz and filtered at 2 kHz) was performed with pClamp 9.2 software (Molecular Devices, Sunnyvale, CA, USA).

In voltage clamp mode, cells were stimulated with a 100 ms lasting hyperpolarizing stimulus (10 mV), then, in the recording, area below the capacitative transients was measured and normalized for voltage transient amplitude to calculate cellular capacitance; input resistance was obtained through Ohm's law, by measuring the amplitude of steady state current generated by voltage transient. Spontaneous postsynaptic currents were analyzed using pClamp 9 (Molecular Devices, Sunnyvale, CA, USA). This program uses a detection algorithm based on a sliding template. The template did not induce any bias in the sampling of events because it was moved along the data trace by one point at a time and was optimally scaled to fit the data at each position. All the collected events were averaged and the amplitude of current was calculated as that of the mean trace.

Statistical significance was tested using unpaired Student t-test (Origin, Northampton, MA,USA). A **p** value < 0.05 was considered as statistically significant. Values are given as mean ± SEM.

## 4.6 Results and discussion

### 4.6.1 Material characterization

PEDOT:PSS layers doped with different amounts of EG were characterized for their physical and morphological properties before using them as substrates for neuronal cultures.

Figure 1A shows the I-V characteristics of PEDOT:PSS layer doped with different concentration of EG, varying from undoped (0 %) up to the 3%. The electrical conductance shows an increase of about one order of magnitude, increasing the concentration of EG. In fact, undoped PEDOT:PSS layer shows an electrical conductance of 2.35 x $10^{-5}$ S, meanwhile the electrical conductance increases up to 1.5 x$10^{-4}$ S in the case of the 3% doped films. The electrical conductivity of our substrates confirms a linear relationship between the conductive properties of PEDOT:PSS and the amount of EG dopant.

The analysis of the contact angle on the PEDOT:PSS layers revealed that the EG concentration controls also the hydrophilicity of the surface. In fact, we observed that the wettability of PEDOT:PSS increases by increasing the EG concentration. Figure 1B shows the digital images of water contact angle of PEDOT:PSS layer doped with different concentration of EG. The contact angle decreases from 21.96 to 12.10 with increasing EG from 0% to 3%. The contact angle analysis reveals that the wettability of the PEDOT:PSS layer increases with the same concentrations of EG used to improve conductance.

This is an interesting property, since wettability of surfaces plays an important role in cell fate, behavior and spreading [19], probably because of the amount of biological molecules absorbed by the substrate surface showing hydrophilic properties.[20]

AFM measures on 10x10 $\mu m^2$ sampled areas shows a relatively flat and smooth surface for all samples while, at higher magnifications, surfaces appears more granulose (Figure 1C). Roughness analysis reveals values of 1.73 nm, 2.38 nm and 6.69 nm for PEDOT:PSS doped with 0%, 1% and 3% EG, respectively. Surface analysis highlighted values of the ratio between the effective surface area and the projected surface area of 1.0059, 1.0018 and 1.030 for the three substrates. These values correspond to an increase of the exposed surface of about 0.6%, 0.2% and 3%, respectively for 0%, 1% and 3% EG contents, compared to a perfectly flat surface characterized by a unitary value of $S_r$.

A preliminary roughness analysis of PEDOT:PSS layers shows an increase in surface RMS values as the amount of EG increased. Compared to the control 0% EG, PEDOT:PSS 1% EG shows an increase in roughness of about 37% while PEDOT:PSS 3% EG presents a nearly three times higher roughness (287%) than controls. $S_r$ ratio between the effective surface area and the projected area presents a small decrease in PEDOT:PSS 1% EG samples than 0% EG controls, but PEDOT:PSS 3% shows a valuable increase of the exposed area (about 3% larger than controls, see Results). This fact may reflect in a better charge exchange efficacy of the PEDOT:PSS 3% EG surface than the 1% EG one.

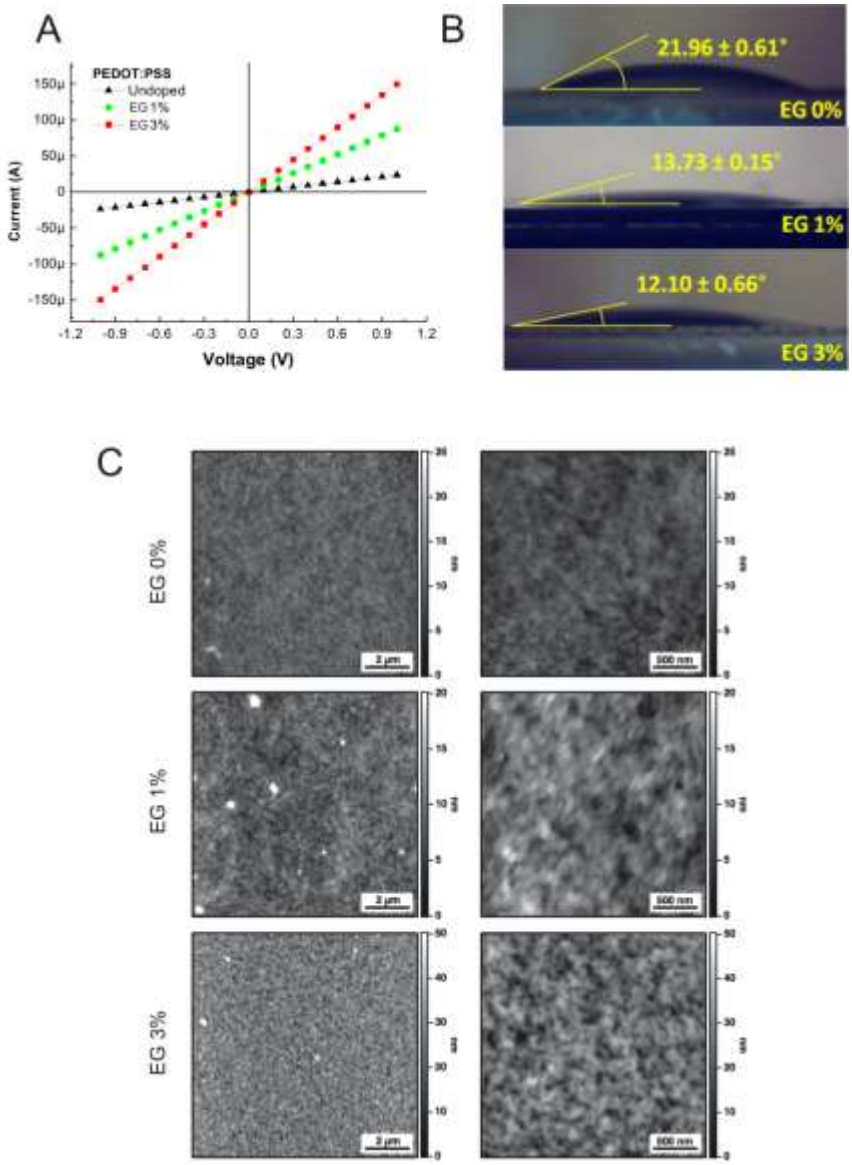


Fig. 9 A. Current-Voltage characteristics of the PEDOT:PSS layer doped with different concentration of EG. B. Water contact angles of the PEDOT:PSS layer doped with different concentration of EG. C. 10x10 $\mu m^2$ AFM images (left column) and the corresponding 2.5x2.5 $\mu m^2$ magnifications (right column) of PEDOT:PSS layers doped with increasing amounts of EG (0%, 1% and 3%). Brighter color areas in the image correspond to higher portions of the sample.

### 4.6.2 PEDOT:PSS layers for hippocampal cultures

After physical and morphological characterization, PEDOT:PSS layers doped with different amounts of EG were used as substrates for hippocampal cultures. Neuronal and glial cells were analyzed at different times of their growth.

### 4.6.3 Undoped PEDOT:PSS and PEDOT:PSS 1% EG are permissive substrates for neuronal cultures

In a first set of experiments, we investigate whether the EG dopant addition in PEDOT:PSS layers affects the viability and/or the activity of short term hippocampal cultures.

Hippocampal cells obtained from postnatal rats were seeded on undoped PEDOT:PSS, PEDOT:PSS 1% EG and control substrates. Cells attached to all the substrates and began extending neurites and contacting other neurons within 24 hours. After 8 DIV, cells formed a complex neuronal network in all the conditions of growth.

At this time, hippocampal cultures on PEDOT:PSS and control substrates were fixed and immunostained in order to investigate culture composition and to measure the cell density. Neurons were identified through the specific antibody against the neuronal marker β-tubulin III, while for glial cells antibody against glial fibrillary acidic protein (GFAP) was used. [21]Nuclei were labeled with DAPI (Figure 10A). Neuronal cell density is similar between control and PEDOT:PSS layers (388±40, 434±29 and 366±20 cells, respectively control, undoped PEDOT:PSS and PEDOT:PSS 1%EG, n= 8 fields each). On the contrary, glial cell density appears reduced on PEDOT:PSS layers with respect to the

control (217±10 cells in control, 140±8 cells on undoped PEDOT:PSS and 185±15 cells on PEDOT:PSS 1%), although the difference was statistically significant only between undoped PEDOT:PSS and control ($p<0.005$, T-test; Figure 10B).

We further quantify the intensity of GFAP fluorescence and the dimension (area size) of single glial cells in the different groups, despite the decreased number of GFAP positive cells, no differences were observed in these parameters (GFAP fluorescence: control 42±1.4 arbitrary units, undoped PEDOT 46±1.7 arbitrary units and PEDOT 1%EG 40±1.7 arbitrary units; glial cells area: control 2483±202 $\mu m^2$, undoped PEDOT 2345±168 $\mu m^2$ and PEDOT 1% EG 2143±165 $\mu m^2$, n=43, n=40, n=44 respectively; Figure 10B).

The viability of neurons grown on PEDOT:PSS layers was assessed by means of patch clamp technique at 8 DIV. Firstly, some passive properties of neurons, such as resting membrane potential, membrane capacitance and input resistance, were measured. These parameters are commonly considered as indicators of neuronal health.[22,23] Neurons grown on PEDOT:PSS layers did not show any statistically significant difference with respect to the control in these values (resting membrane potential: -45±4, -47±3 and -46±3 mV; capacitance: 71±19 pF, 63±26 pF and 59±6 pF; input resistance: 740±98 MΩ, 857± 98 MΩ, 855±119 MΩ, respectively control n=16, undoped PEDOT:PSS n=18, PEDOT:PSS 1% EG n=15; Figure 10C). This indicates that neurons grown on PEDOT:PSS layers are as healthy as in control at 8 DIV.

Neurons grown on PEDOT:PSS layers showed spontaneous synaptic activity made up by a mixed population of inhibitory and excitatory post synaptic currents (both detected as inward currents in our recording conditions; Figure 10D;[24]). The presence of such spontaneous post synaptic currents (sPSCs) indicates that PEDOT:PSS layers support the growth of neurons that formed

functionally active synapses. Moreover, the amplitude and the frequency of sPSCs recorded on PEDOT:PSS layers were fully comparable with those of cells in control (sPSCs amplitude: 50±5 pA, 49±8 pA and 50±7 pA; sPSCs frequency: 1.4±0.2 Hz, 1.8±0.5 Hz and 1.9±0.4 Hz for control n=17, undoped PEDOT:PSS n=18 and PEDOT:PSS 1% EG n=16; Figure 10D). These results, together with the comparable neuronal density, indicates that the size of the neuronal network developed on PEDOT:PSS layers and its functionality are fully comparable with those of controls after a week of maturation and growth in vitro. The presence of the dopant EG appears not to change the properties of the layers in terms of neuronal network, except for a reduction in the amount of glial cells on undoped layer respect to the doped one.

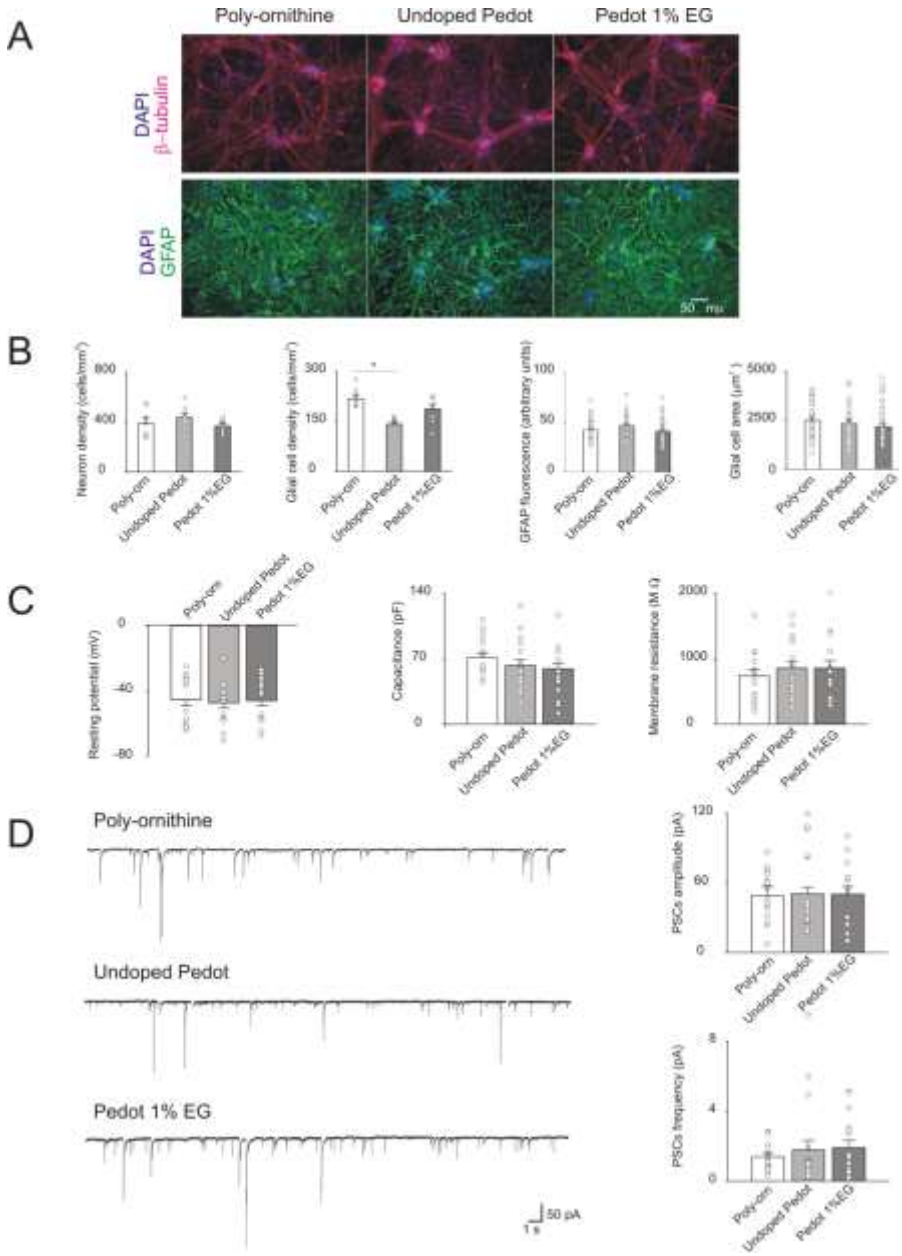


Fig. 10: A. Immunofluorescence images of cultures grown on poly-ornhitine, undoped PEDOT:PSS and PEDOT:PSS 1%EG. Cells were stained with antibodies anti-βtubulin (red), -GFAP (green) and nuclei were marked with DAPI (blue) B. Bar plots show mean values of neuronal and glial cells density, GFAP fluorescence intensity and glial cells areas in the different conditions of

growth. Superimposed dots to the bars are values from single fields (for cell density) or from single cells (for GFAP intensity and glial cell areas). Note that the glial cell density is significantly decreased on undoped PEDOT:PSS respect to the poly-ornhitine control (*p<0.05, T test). C. Bar plots are mean values of resting membrane potentials, capacitance and membrane resistance. Superimposed dots to the bars are values from single experiments. D. On the left, exemplificative recordings from neurons grown on poly-ornhitine, undoped PEDOT:PSS and PEDOT:PSS 1%EG respectively. On the right, bar plots show the means values of spontaneous PSCs amplitude and frequency in the different conditions of growth. Superimposed dots to the bar are values from single experiments.

### 4.6.4 Long term hippocampal cultures on PEDOT:PSS 1% EG and 3% EG are functionally healthy, although the amount of glial cells is reduced.

Considering that for prosthetic applications PEDOT:PSS containing EG has improved charge transport properties than EG free one, and the addition of EG is necessary to enhance the electrical conductivity[11,12], in the next series of experiments hippocampal cells were seeded on PEDOT:PSS 1% and 3% EG. This was made in order to verify the viability of long term cultures on PEDOT:PSS layers, mimicking what could happen in in vivo long term implants.

After 21 DIV, hippocampal cultures on PEDOT:PSS layers and in control were fixed and immunostained with antibodies against β-tubulin III and GFAP. DAPI was used to mark nuclei (Figure 11A). The quantification of neuronal density showed no differences between PEDOT:PSS layers and control ones (249±33 cells, 256±34 cells and 234±20 cells, respectively for control, PEDOT:PSS 1% EG and PEDOT:PSS 3%EG, n= 8 fields each).On the contrary, PEDOT:PSS layers inhibit the growth of glial cells, as shown by the reduction in cell density found on these substrates (65±4 cells in control, 42±4 cells on PEDOT:PSS 1% EG and 45±6 cells on PEDOT:PSS 3% EG). The difference was statistically significant for both PEDOT:PSS 1% EG and PEDOT:PSS 3% EG respect to the control (p<0.05,

T-Test, Figure 11B).

In addition, although the intensity of GFAP fluorescence was found to be similar among the various conditions of growth (GFAP fluorescence: control 69±3.2 arbitrary units, PEDOT:PSS 1% EG 73±3.7 arbitrary units and PEDOT:PSS 3% EG 78±4 arbitrary units), glial cells grown on PEDOT:PSS layers showed a reduction in their areas with respect to those in control (glial cells area: control 11882±758 $\mu m^2$, PEDOT:PSS 1% EG 9018±1209 $\mu m^2$ and PEDOT:PSS 3% EG 7053±633 $\mu m^2$, n=56, n=37, n=37 respectively). The difference was statistically significant ($p<0.05$, T-Test, Figure 11B).

Some membrane passive properties of neurons grown in control and on PEDOT:PSS layers were measured in order to assess the health of cells after 3 weeks in culture. Similar values of membrane properties were found with resting membrane potential: -48±2 mV, -46±2 mV and -45±2 mV; capacitance: 70±8 pF, 68±6 pF and 59±6 pF; input resistance: 414±55 MΩ, 302±34 MΩ, 464±90 MΩ, respectively control n=25, PEDOT:PSS 0% EG n=25, PEDOT:PSS 1% EG n=24; Figure 11C).

The spontaneous activity of the network developed on PEDOT:PSS layers was monitored at 3 weeks in culture. Neurons grown on both PEDOT:PSS 1% EG and PEDOT:PSS 3% layers showed spontaneous activity. In addition, the frequency and the amplitude of sPSCs appeared not to be changed on PEDOT:PSS layers with respect to the control ones after 21-22 DIV in vitro (sPSCs amplitude: 71±9 pA, 81±12 pA and 69±10 pA; sPSCs frequency: 5.6±1.3 Hz, 5.3±1.4 Hz and 4.6±1.3 Hz for control n=25, PEDOT:PSS 1% EG n=25 and PEDOT:PSS 3% EG n=24; Figure 11D).

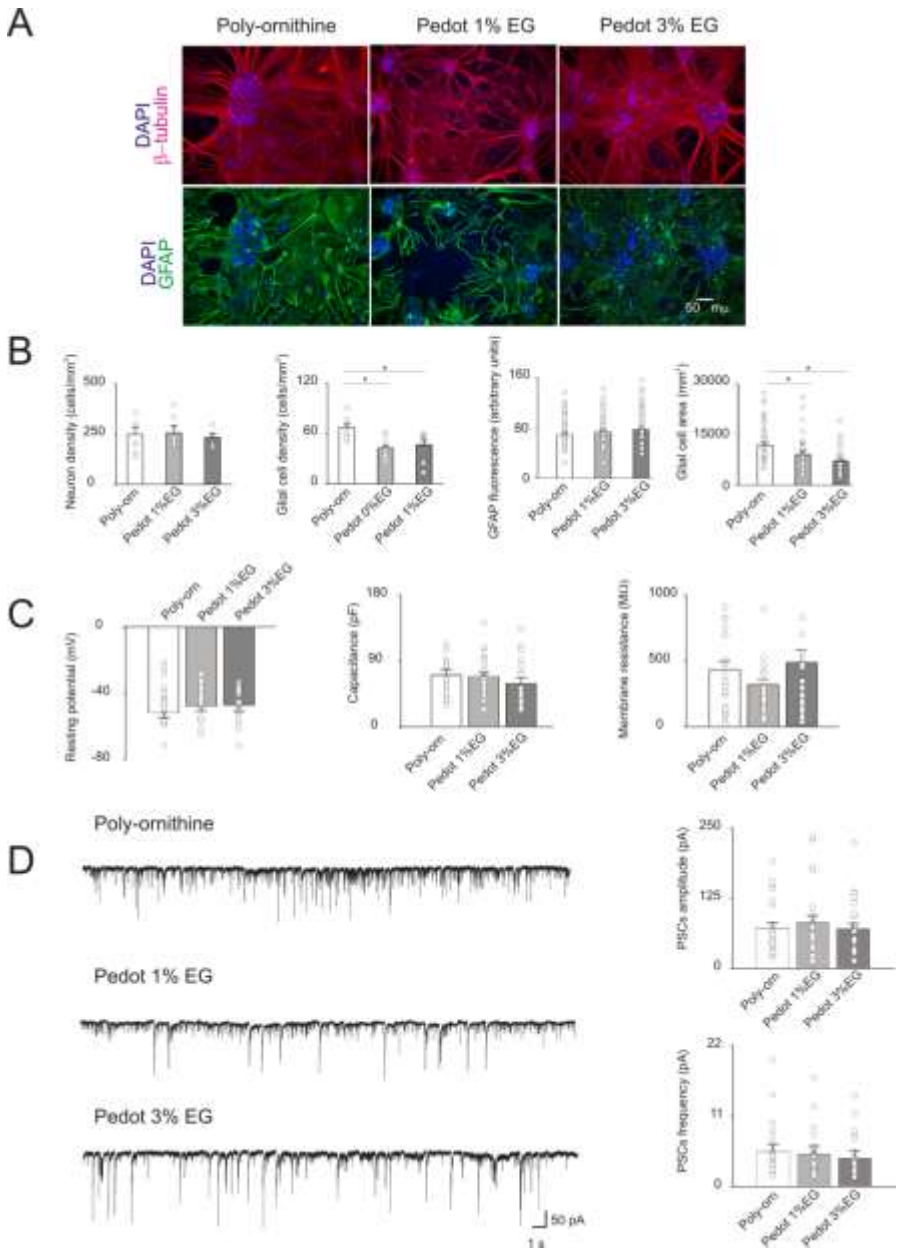


Fig. 11: A. Immunofluorescence images of cultures grown on poly-ornithine, PEDOT:PSS 1%EG and PEDOT:PSS 3%EG. Cells were stained with antibodies anti-βtubulin (red), -GFAP (green) and nuclei were marked with DAPI (blue) B. Bar plots show mean values of neuronal and glial cells density, GFAP fluorescence intensity and glial cells areas in the different conditions of growth. Superimposed dots to the bars are values from single fields (for cell density) or from single cells

(for GFAP intensity and glial cell areas). Note that the glial cell density and area are significantly decreased on both PEDOT:PSS 1%EG and 3%EG respect to the poly-ornithine control (*p<0.05, T test). C. Bar plots are mean values of resting membrane potentials, capacitance and membrane resistance. Superimposed dots to the bars are values from single experiments. D. On the left, exemplificative recordings from neurons grown on poly-ornithine, PEDOT:PSS 1%EG and PEDOT:PSS 3%EG respectively. On the right, bar plots show the means values of spontaneous PSCs amplitude and frequency in the different conditions of growth. Superimposed dots to the bar are values from single experiments.

### 4.6.5 SEM images show healthy morphology of neurons grown on PEDOT:PSS layers

The morphology of neurons was visualized by scanning electron microscope. Cultures grown on control and PEDOT:PSS layers doped with different amount of EG were fixed at 8 DIV and processed for SEM. Figure 12A shows that neuronal network appears similarly dense in terms of number of cells and comparably connected between control and PEDOT:PSS 3% EG. Darker areas correspond to glial cells. Higher magnification of micrographs (Figure 12B) shows the healthy morphology of single neurons developed on PEDOT:PSS layers, similar to that of control neuron. In all the conditions of growth, many neurites emerge from the soma and extend centrifugally on the substrates, forming intricate arborizations.

By scanning electron microscopy, we observed that neurons grown for a week on PEDOT:PSS layers show a healthy morphology, with many neurites extending from the soma and forming arborizations, similarly to cells on control substrates. Also the size of the network was comparable, as immunofluorescence experiments show, where the density of neurons that attached and developed on PEDOT:PSS substrates is similar to that of control, both at 1 and 3 weeks in vitro.

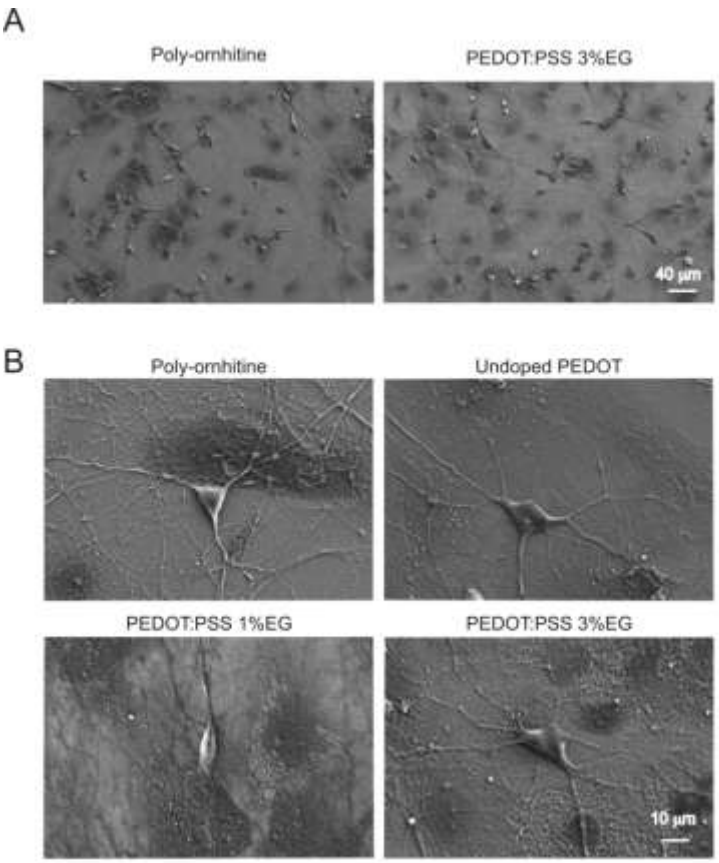


Fig. 12**:** Scanning electron microscopy micrographs showing hippocampal cultures grown on PEDOT:PSS layers. A. Lower magnification micrographs display that qualitatively the size of neuronal network is comparable between undoped PEDOT:PSS and PEDOT:PSS 3%EG. B. Higher magnification micrographs show the healthy morphology of single neurons grown on the different substrates.

**4.7 Discussions and conclusions**

The biocompatibility of PEDOT:PSS was tested by culturing dissociated postnatal hippocampal cells obtained from neonatal rats. This is a widely adopted and well characterized model for neuronal network in vitro. Neurons, in fact, after a few hours from seeding are able to attach to the substrates, if permissive, and begin to extend neurites. In the following days, neurites elongate, take contact with those of other neurons, forming synapses that are functionally active after a week in vitro. Spontaneous activity of the network shows both excitatory and inhibitory postsynaptic currents as observed in vivo.[25]

We further characterized neurons developed on PEDOT:PSS from a functional point of view via electrophysiological recordings[16,24]. Although electrical activity from neuronal populations grown on conductive polymers has been partially characterized previously by multi-electrode arrays, by using patch clamp technique we obtained single cell electrical properties and synaptic network activity in detail.

Our experiments revealed that single cell membrane passive properties, known indicators of neuronal health[22,23], and the spontaneous activity of the network, measured in terms of amplitude and frequency of sPSCs, were fully comparable between cultures grown on PEDOT:PSS and controls. This was observed for neurons after a week in culture (undoped and 1%EG), but also in long-term cultures (3 weeks in vitro) with even higher concentrations of dopant (up to 3%EG). Thus, on PEDOT:PSS interfaces we develop healthy neurons and functionally active synaptic networks, comparable to those grown on traditional peptide-layared substrates (controls).

Intriguingly, PEDOT:PSS down-regulated glial cells, with the GFAP-positive

neuroglia showing reduced density and smaller cell-area after being interfaced for 3 weeks on PEDOT:PSS, with respect to control. Notably, the intensity of GFAP fluorescence signal appeared similar among all tested groups. A partial reduction in glial cell density was already observed after 1 week of in vitro growth, although the difference with respect to the control was statistically significant only for undoped PEDOT:PSS.

An increased number of glial cells and an enhanced glial cellular size are usually associated with pathological states, thus PEDOT:PSS apparently reduces glial response, a relevant feature for exploiting implantable electrodes able to induce low glial reactions [14]

Other conductive polymers, such as PEDOP and P3MT, but not PEDOT, been already reported to reduce astrocyte responses in in vivo implants.[26] The layers evaluated by Forcelli were produced under very different conditions (was not used PSS as counterion dopant and the deposition process was different), for this reason that results must be evaluated in the context of conditions employed for that deposition. It is likely that different procedures in preparation of layers could be responsible for such diversity .

However, it is interesting to note that the reduced glial response observed on PEDOT:PSS layers in our long term cultures seems not to influence the functional properties of neuronal network, as our experiments detected similar neuronal density and comparable electrical activity between PEDOT:PSS and control.

Thus, PEDOT:PSS materials could be exploited in the development of new implantable devices, that depress the glial reactivity induced by the presence of an external object in the nervous tissue, but without affecting neuronal viability and functionality.

**4.8 Future works**

Detection and analysis of the bioelectricity will be used to analyze the sMD/neurons system. Calcium imaging generates versatile intracellular signals that control neuronal activity. Biophysical properties (single ion channels, synaptic cell activity) will be measured by electrophysiology. Patch-clamp and/or other techniques will be selected on the base of cell prep specificity.

Single tissue cells and reduced preparations of parts of vertebrate/invertebrate central nervous system will be tested for sMD interactions. In vitro retina preparations will be used to measure activity of retinal ganglion cells (RGCs) during electrical stimulation.

Explants of RGCs (“Stripe assay”) interacting directly with sMD will be used. Reduced preps of isolated ganglia and photoreceptors from invertebrates will be used, with a reliable cross-talk with the sMD and a modulatory electrical behavior exerted by a sensory input. Retina's response to electrical stimulation will be analyzed in real time using genetically encoded calcium indicators.[27]

**Bibliography**


[1] Outline C Neurons, neurotransmission and communication 1–25

[2] Smith A J, Bainbridge J W and Ali R R 2009 Prospects for retinal gene replacement therapy. *Trends Genet.* **25** 156–65

[3] Polosukhina A, Litt J, Tochitsky I, Nemargut J, Sychev Y, De Kouchkovsky I, Huang T, Borges K, Trauner D, Van Gelder R N and Kramer R H 2012 Photochemical restoration of visual responses in blind mice. *Neuron* **75** 271–82

[4] Ong J M and da Cruz L 2012 A review and update on the current status of stem cell therapy and the retina. *Br. Med. Bull.* **102** 133–46

[5] Yang Y-T, Lin P-K, Wan C, Yang W-C, Lin L-J, Wu C-Y and Chiao C-C 2011 Responses of rabbit retinal ganglion cells to subretinal electrical stimulation using a silicon-based microphotodiode array. *Invest. Ophthalmol. Vis. Sci.* **52** 9353–61

[6] Martino N, Ghezzi D, Benfenati F, Lanzani G and Antognazza M R 2013 Organic semiconductors for artificial vision *J. Mater. Chem. B* **1** 3768

[7] Nanditha D M, Dissanayake M, Hatton R A, Curry R J and Silva S R P 2007 Operation of a reversed pentacene-fullerene discrete heterojunction photovoltaic device *Appl. Phys. Lett.* **90** 113505

[8] Garnett E and Yang P 2010 Light Trapping in Silicon Nanowire Solar Cells *Nano Lett.* **10** 1082–7

[9] Lee D C and Jang L W 1996 Preparation and characterization of PMMA-clay hybrid composite by emulsion polymerization *J. Appl. Polym. Sci.* **61** 1117–22

[10] Panahi-Bazaz M-R, Zamani M and Abazar B 2009 Hydrophilic Acrylic versus PMMA Intraocular Lens Implantation in Pediatric Cataract Surgery. *J. Ophthalmic Vis. Res.* **4** 201–7

[11] Ouyang J, Chu C-W, Chen F-C, Xu Q and Yang Y 2005 High-Conductivity Poly(3,4-ethylenedioxythiophene):Poly(styrene sulfonate) Film and Its Application in Polymer Optoelectronic Devices *Adv. Funct. Mater.* **15** 203–8

[12] Crispin X, Marciniak S, Osikowicz W, Zotti G, van der Gon A W D, Louwet F, Fahlman M, Groenendaal L, De Schryver F and Salaneck W R 2003 Conductivity, morphology, interfacial chemistry, and stability of

poly(3,4-ethylene dioxythiophene)-poly(styrene sulfonate): A photoelectron spectroscopy study *J. Polym. Sci. Part B Polym. Phys.* **41** 2561–83

[13] Tarabella G, Mahvash Mohammadi F, Coppedè N, Barbero F, Iannotta S, Santato C and Cicoira F 2013 New opportunities for organic electronics and bioelectronics: ions in action *Chem. Sci.* **4** 1395

[14] Lempka S F, Miocinovic S, Johnson M D, Vitek J L and McIntyre C C 2009 In vivo impedance spectroscopy of deep brain stimulation electrodes. *J. Neural Eng.* **6** 046001

[15] Nečas D and Klapetek P 2013 One-dimensional autocorrelation and power spectrum density functions of irregular regions. *Ultramicroscopy* **124** 13–9

[16] Lovat V, Pantarotto D, Lagostena L, Cacciari B, Grandolfo M, Righi M, Spalluto G, Prato M and Ballerini L 2005 Carbon nanotube substrates boost neuronal electrical signaling. *Nano Lett.* **5** 1107–10

[17] Avossa D, Rosato-Siri M ., Mazzarol F and Ballerini L 2003 Spinal circuits formation: a study of developmentally regulated markers in organotypic cultures of embryonic mouse spinal cord *Neuroscience* **122** 391–405

[18] Abrashkin V, Alexandrov V, Arakcheev Y, Cotzomi J, Diaz A, Finger M, Garipov G, Grebenyuk V, Kalmykov N, Khrenov B, Kim S H, Klimov P, Koval V, Martinez O, Nam S W, Naumov D, Olshevsky A, Panasyuk M, Park I H, Park J H, Ponce E, Puchkov A, Robledo C, Rosado A, Rubinshtein I, Sharakin S, Silaev A, Tkatchev L, Tulupov V, Sabirov B, Salazar H, Saprykin O, Villasenor L, Yashin I and Zaikin N 2008 Updated TUS space fluorescence detector for study of UHECR *Adv. Sp. Res.* **41** 2079–88

[19] van Kooten T G, Schakenraad J M, van der Mei H C and Busscher H J 1992 Influence of substratum wettability on the strength of adhesion of human fibroblasts *Biomaterials* **13** 897–904

[20] Dekker A, Reitsma K, Beugeling T, Bantjes A, Feijen J and van Aken W G 1991 Adhesion of endothelial cells and adsorption of serum proteins on gas plasma-treated polytetrafluoroethylene *Biomaterials* **12** 130–8

[21] Fabbro A, Villari A, Laishram J, Scaini D, Toma F M, Turco A, Prato M and Ballerini L 2012 Spinal cord explants use carbon nanotube interfaces to enhance neurite outgrowth and to fortify synaptic inputs. *ACS Nano* **6** 2041–55

[22] Beier K T, Steinberg E E, DeLoach K E, Xie S, Miyamichi K, Schwarz L, Gao X J, Kremer E J, Malenka R C and Luo L 2015 Circuit Architecture of VTA Dopamine Neurons Revealed by Systematic Input-Output Mapping *Cell* **162** 622–34

[23] Carp J S and Wolpaw J R 1994 Motoneuron plasticity underlying operantly conditioned decrease in primate H-reflex *J Neurophysiol* **72** 431–42

[24] Cellot G, Toma F M, Varley Z K, Laishram J, Villari A, Quintana M, Cipollone S, Prato M and Ballerini L 2011 Carbon nanotube scaffolds tune synaptic strength in cultured neural circuits: novel frontiers in nanomaterial-tissue interactions. *J. Neurosci.* **31** 12945–53

[25] Anon 1993 Spontaneous activity and recurrent inhibition in cultured hippocampal networks. *Synapse* **14** 206–13

[26] Forcelli P A, Janssen M J, Vicini S and Gale K 2012 Neonatal exposure to antiepileptic drugs disrupts striatal synaptic development. *Ann. Neurol.* **72** 363–72

[27] Wang X, Reisberg S, Serradji N, Anquetin G, Pham M-C, Wu W, Dong C-Z and Piro B 2014 E-assay concept: detection of bisphenol A with a label-free electrochemical competitive immunoassay. *Biosens. Bioelectron.* **53** 214–9

# Chapter 5

# Epicardial-interacting patch SiC NWs Based

Several patients suffer from cardiac disease, including myocardial infarction. The occurrence of arrhythmias as a consequence of myocardial infarction can be reduced by introducing an electrical bypass across the infarcted region.

As presented in the previous chapter, nanotechnology and nanomaterials can provide a new generation of biomedical devices, with dimensions that can bio-mime the extracellular matrix and increase the process of “acceptance” from biological system. The SiC NWs, as shown in the chapter 2, are cytocompatible and hemocompatible, therefore suitable to cardiac devices.

In this Chapter we propose a new nanodevice that allows to re- establish electrical conduction across infarct area. The device is based on silicon-carbide conductive nanowires embedded in an epicardial-interacting patch.

## 5.1 Introduction

Millions of patients around the world suffer from cardiac disease and it is the leading cause of death worldwide.

There are many risk factors associated with cardiac disease as myocardial infarction. Some risk factors connect to the person as family history, ethnicity and age. Other risk factors that can be connected to life style include tobacco exposure, high blood pressure (hypertension), high cholesterol, obesity, physical inactivity, diabetes, unhealthy diets, and harmful use of alcohol.

Of particular significance in developing countries is the fact that while they are grappling with increasing rates of cardiovascular disease, they still face the scourges of poor nutrition and infectious disease. Nevertheless, with the exception of sub-Saharan Africa, cardiovascular disease is the leading cause of death in the developing world.[1](Figure 1).

Today there are 7.3 million of deaths worldwide for myocardial infarction: the figure is increased during the last years increase, and the problem is one of new scourges.

The death as a results of myocardial infarction can be caused by different factors, which we will be explained in detail in this chapter.

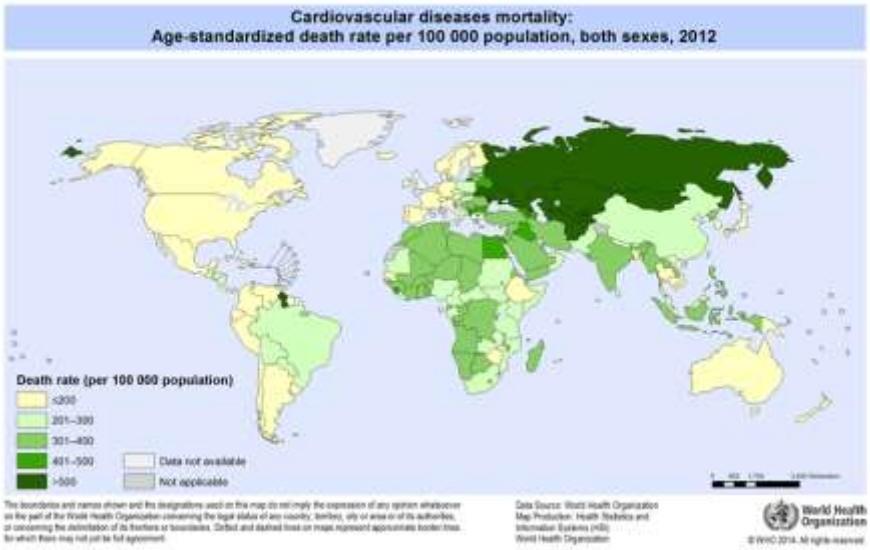


Fig. 1 Map of cardiac disease in the worldwide. The map shows the number of people affected in relationship with country in 2012 (WHO data source)

### 5.1.1 The myocardial infarction

The heart is an exquisitely electromechanical organ, which modify is pump function every single beat in relation to the pumped blood required from the body. The main actor parenchymal cell is the cardiomyocyte (CMs, 30% of the total cardiac cells) which contract synchronous together with the adjacent coupled CMs and the stromal cardiac fibroblast (65-70% of the total cardiac cells) which provide the scaffold for the normal pump function. The life of cardiac cells is supported by the coronary arteries network which supplies blood for maintaining the normal structure and functionality. When the blood stops flowing properly to a part of a cardiac tissue, the muscle become injured because it is not receiving enough oxygen. This is due to a blockage of the upstream coronary made by blood clot, atherosclerosis plaques, stenosis or rupture. Such event is called myocardial infarction (MI) which cause.

Although the clinical presentation of a patient is an important component in

the overall evaluation of MI, many events are either "silent" or are clinically unrecognized, evidencing that patients, families, and health care providers often do not recognize symptoms. The main approach to determine the MI are electrocardiograms (ECG) that trace the electrical signals (sinus propagation) during the heartbeat. ECG recognized two types of MI, where the trace between the two ECG's waves 'S' and 'T' is elevated (ST-elevation MI, STEMI) or not (NSTEMI). Both conditions are immediately treated for re-establishing the blood flow or the oxygen to the (ischemic area) using reperfusion protocols coadjutant by aspirin, nitroglycerine, or if necessary angioplasty and bypass surgery (CABG). A secondary prevention is focused on preserving the survived cardiac tissue which has now the role to maintain the reduced pump-function of the heart. Prevention focuses on changing the lifestyle associate with several long-term medication (beta-blockers, aspirin, ACE inhibitors and statins), depending on the type of MI, on the damaged area and on the heart performance. Despite the efforts and the achievements made in the past years the prognosis is still unfavorable: in STEMI patients between 5 to 6 percent die before leaving hospital and 7 to 18 percent die within a year (USA)[2]. This is because the infarcted heart (including damaged and not-damaged areas) comes into a re-adaptation process which includes structural and functional remodeling (see follow paragraph) that is frequently accompanied by multiple complications such as re-infarction and infarct extension, cardiac rupture and failure and cardiac arrhythmias.

### 5.1.2 Structural remodeling of post-myocardial infarction

It is well recognized that multiple pathological conditions including pressure overload, volume overload and infarction induces structural remodeling of the heart which can lead to heart failure and cardiac arrhythmias. [3,4]Histopathologically, remodeling typically involves cardiomyocyte hypertrophy, activation and proliferation of (myo)fibroblasts (MFBs, Fig.2), increased extracellular matrix deposition and cell death.[5] Functionally, structural remodeling induces mechanical dysfunction and is accompanied by an increased likelihood of occurrence of life-threatening cardiac arrhythmias.[3] These modifications are based on complex cellular reactions to injury and involve both cardiomyocytes and non-cardiomyocytes leading to changing in the shape, size and the normal function of the organ. Mechanistically, arrhythmias in structurally remodeled hearts can be divided into (i) mechanisms related to altered cellular electrophysiological properties of the cardiomyocytes ('electrical remodeling') and (ii) mechanisms related to the remodeling of the extracellular matrix ('fibrosis'). Electrical remodeling affects a large number of ion channels, exchangers and calcium handling proteins and ultimately predisposes the heart to arrhythmias by, e.g., inducing calcium overload related triggered activity or by causing dispersion of repolarization and thereby enabling reentrant electrical activity.[3–6] Moreover, connexins redistribution as observed in remodeled tissue following myocardial infarction (MI) affects impulse propagation and predisposes the heart to arrhythmias.[7]Fibrosis within the infarct scar, favors the initiation and perpetuation of arrhythmias by overproducing collagenous septa without control which separate bundles of cardiomyocytes over distances up to several millimeters, resulting as structural discontinuities at the cellular level.[8] Based on the principle that fibrotic laminae and collagenous septa act as electrical

insulators which induce interstitial resistive discontinuities, the normal wavefront electrical propagation, under these conditions, collapse and result in non-uniform conduction[9] or zig-zag activation of the myocardium.[10] Both of these conditions result in slow conduction and unidirectional or multidirectional conduction blocks which are harbinger of re-entrant arrhythmias.

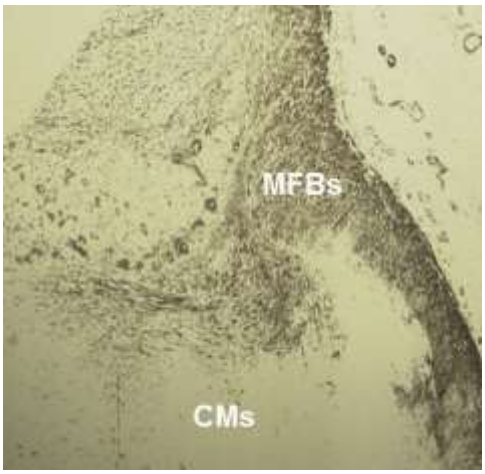


Fig. 2: Ventricular slice of infarcted human heart. Alpha smooth muscle actin as hallmark of myofibroblasts are displayed by immunoperoxidase reaction.
CMs: cardiomyocytes.
MFBs myofibroblasts.
Bar: 1 mm

### 5.1.3 Myofibroblasts in the infarct scar

In normal human hearts, fibroblasts outnumber cardiomyocytes by a factor of ~ 2-3 while occupying ~20 % of the volume of the working myocardium[11]. Fibroblasts produce a network of collagen fibers which acts as a scaffold for cardiomyocytes and integrates the mechanical forces as to result in an efficient pump function of the entire organ. This fibrillar network is subjected to substantial turnover which can amount up to ~5% per day[12]. Under physiological conditions, tight control of formation and degradation of collagen is therefore necessary to maintain the structural and functional integrity of the myocardium over time. Under pathological conditions like, e.g., hypertensive heart disease and MI, the delicate balance between formation and

degradation of collagen tips towards an accumulation of extracellular matrix (ECM) which is caused by increased secretory activity and proliferation of fibroblasts. Importantly, both reactive fibrosis as well as reparative fibrosis occurring in the context of infarction are typically accompanied by the appearance of so-called myofibroblasts (MFBs), which is considered to be an essential step in the establishment of fibrosis[13].

### 5.1.4 Myocardial infarction and arrhythmias

About 90% of patients who have an acute MI show arrhythmia symptoms. Electrolyte imbalance (e.ghypokalemia)[14] and hypoxia further contribute to the development of cardiac arrhythmia in the first 24-48 hours (25% of cases). Several categories of arrhythmias are associated with MI, ranging from supraventricular tachyarrhythmias, accelerated junctional rhythms, atrioventricular blocks, intraventricular blocks, ventricular tachycardia and fibrillation. Such circumstances are almost no-compatible with life and they can also be accompanied with myocardial rupture (ventricular free wall, septum or papillary muscle ruptures). Myocardial rupture may also occur iatrogenically during percutaneous cardiac procedures (including device implantation) or open heart surgery (particularly valve replacement)[14]. Although does not exist possibility to prevent post MI arrhythmias except for electrolyte supplementation such as potassium and magnesium, we have to notice that the conventional post-MI antiarrhythmic therapy is '*cardiomyocyte*the sarcolemma of the CMs. But what about (myo)fibroblast? The infarct scar persists for many years after MI exerting an indirect mechanisms of ventricular arrhythmias by deviating the normal impulse propagation as the sinus wavefront cannot propagated across MI. Such morphological substrate, together with a decrease of conduction velocity in

the neighbour infarct region (as it also suffer for the low oxygen presence) may, in turn, favour the initiation of an electrical rotor anchored to the infarct area (Fig.3).

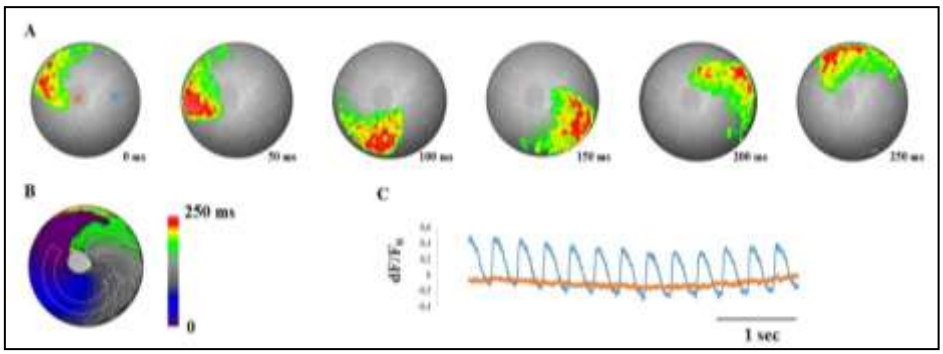


**Fig.3**. Re-entrant impulse propagation in-vitro: role of myofibroblast's area. A. Time-sequence of optical recording of action potential reentry (complete rotation in 250 ms) anchored on myofibroblast's region (trans-lucid in the center of the monolayer). Scale bar: 10 mm B. Color-coded isochrones map image of the entire sequence (interdistance between isochonres: 5 ms). C. Action potential traces recording in the blue and orange squares in A. o note myofibroblast's region is not active in terms of action potential propagation.

### 5.1.5 Nanotechnology and nanomaterials in the context of cardiac infarct propagation

The 21$^{st}$ century has seen major advances in nanotechnology, which can be applied to a wide array of scientific disciplines. In (nano)medicine the utilization of nanomaterials is certainly a growing field which seems to be beneficial in facing up life-threatening diseases (cancer[15], [16]etc.) or for providing biosensors[17], medical imaging[18] or drug delivery[15]. In regards of restoring the aberrant impulse propagation via nanomaterials in the context cardiac diseases only few papers are currently investigating the problem. This lack of information is probably due to complications in matching diverse know-how ranging from cardiac pathophysiology, electrophysiology and biophysics, material matters, nanotoxicology and nanomedicine. Several groups are aware that a proper conductive patch may be beneficial in assisting impulse

propagation when blocks or delays occurred but, up to now, the efforts have mainly focused in manufacturing 'biological' conductive patches, by implanting nanomaterials within a biological substrate, such as magnetical scaffolds including cardiac cells [19], decellularized matrix including gold-nanoparticles[20] or paramagnetic beads-antibody conjugated[21]. From the clinical point of view such approach may require a considerable amount of time spent in: i) extraction, generation and manipulation of the biological material from the patient, ii) integration with nanoparticles or nanowires and iii) implantation of the cardiac patches. Unfortunately, post-MI arrhythmia is an unpredictable event and occur rapidly in the context of unidirectional conduction block, zig-zagpropogation or ectopic activity; thus the request is to act as well in a fast and resolute manner.

## 5.2 Conductive epicardial patch (CEP)design

The final endpoint of this thesis is to provide synthetic biocompatible conductive epicardial patch (CEP) for fast, direct and functional application onto MI damaged area with the aim to reinstate rapidly impulse propagation.

The specific hypothesis behind this device is to shape a conductive epicardialpatch based on Teflon(polytetrafluoroethylene), already used in cardiovascular field(as stent or graft) that include functionalized SiC nanowires (see Figure 4). Such contact patch can bridge the conduction across the cardiac infarct as nanowires can 'sense' the direction of the wavefront propagation on the survival cardiac tissue and transmit it to the downstream surivivedregions without discontinuity. The idea is to develop a new conductive patch that permits to cardiac surgeons to insert and fix it on top of the scarred epicardium once they perform cardiovascular surgery. While this appears to be easy to say in few words it requires an interdisciplinary know-how ranging from nanomaterials and nanotechnology, cardiac electrophysiology, biophysics, computational modeling, toxicology and cardiac surgery.

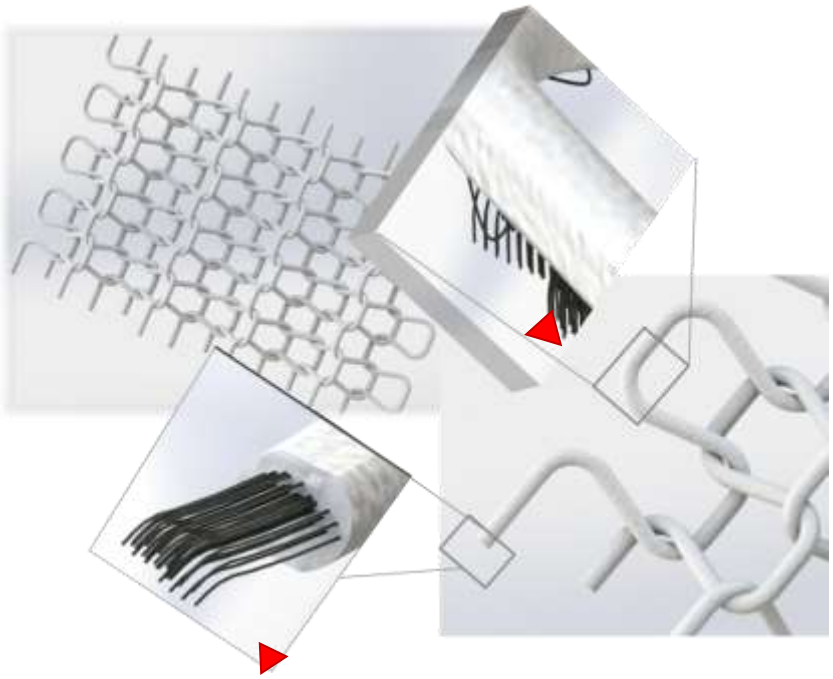

Fig.4 Model of cardiac patch based of SiC NWs(red arrowhead) embedded in Teflon wires

### 5.2.1 Fabrication methods

As explain above, the CEP is based on SiCNWs and Teflon. To study the effect of NWs embedded in Teflon as cardiac patch, actually we designed a prototypal device. In this paragraph the prototipal CEP(pCEP) production methods are explained step by step (Fig.5). The SiC NWs are grown by Vapor-Liquid-Solid (VLS) mechanism by CVD system, using carbon monoxide as precursor, nitrogen as carrier gas and iron as catalyst.

To obtain pure 3C-SiC NWs we etched the SiC/$SiO_2$ core/shell NWs: the NWs growth with a shell of $SiO_2$ that was removed with a chemical etching(the details of NWs growth are explained in the 2nd chapter).

The NWs are coated with polymethyl methacrylate(PMMA). The polymer was dropped on the surface. The PMMA is a material particularly suitable for this purpose because, as explained in the chapter 4, has a high electrical resistivity

(1019 Ω) and biocompatible.

In this work, PMMA with an average molecular weight Mw ~ 350000 (Sigma Aldrich) was used. The NWs surface were covered with PMMA 15 wt% and the NWs are embedded to the polymer. A GORE-TEX® Vascular Grafts, used in cardiovascular surgery for 30 years, was cut following the median line to avoid compromising the texture. It was used in the radial direction to conserve the materials stretchability and to avoid the myocardial increase during the pump.

The graft, appropriately prepared, was used as support: it was placed on the PMMA and the NWs and they were removed from silicon surface by peeling.

To expose the NW's heads the PMMA was etched by Plasma Oxygen: the procedure was performed in plasma oxygen for 90 seconds at 60.4 mTorr and 50 mW. The plasma etching steps were examined by SEM (figure 5 down).

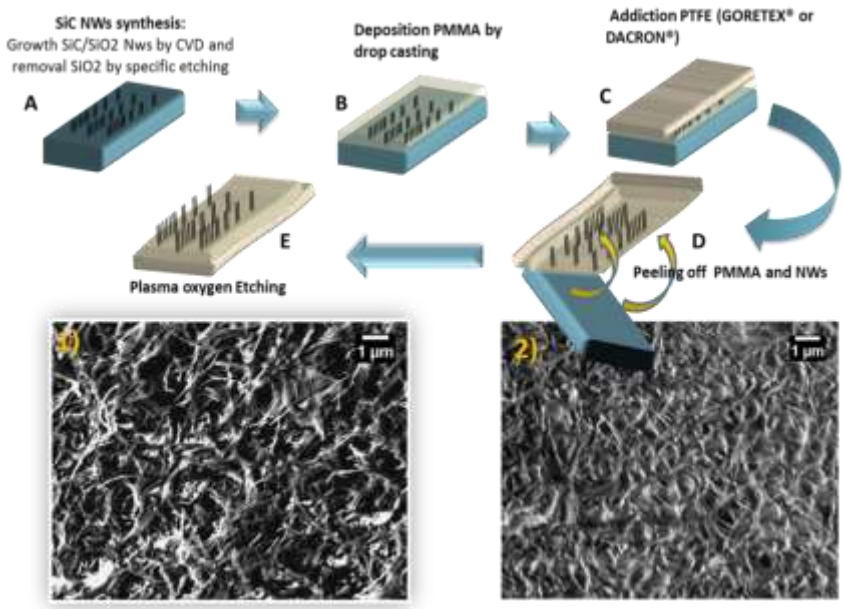


Fig. 5 up )schematic representation the production methods used for pCEP. A) SiC NWs are growth by CVD system. B) PMMA was deposited on NWs substrate by drop casting C) the graft was placed on PMMA D)The patch was removed from silicon by peeling E)PMMA is etched by Plasma Oxygen, exposing the NWs's heads. Fig 5 Down) SEM images 1) after and 2) before the plasma etching.

## 5.3 Preliminary studies

### 5.3.1 Heterocellular electrical impulse propagation between coupled cardiac cells

We recently start to define the biophysic and dynamism properties of the coupling between CM and MFBs since those data will be crucial for the functionalization of the SiC-NWs. We optogenetically transfected MFBs with halorhodopsin hyperpolarizing Chloride pump (Halo) for hyperpolarizing MFB membrane potential by light excitation (please see methodological section for details). By changing the (photo) potential MFB alone, or coupled with a CM we can extract central parameters such as resting membrane potential (Vm) and current-voltage relationship (I-V), both important characteristics in the context of cell-to-cell conductance (Fig.6). The optogenetic intervention mimicked the presence of SiC nanowires that may affect the conductance when coupled two separate cardiac cells. We found that MFBs membrane potential switches from -26 mV to – 72 mV when Halo channels are opened returning the maximal hyperpolarization that MFBs can encountered. The change in photopotential was caused by the inwardly directed chloride current initiated by the pump, which had a very rapid on and off time constant of 9.5 ms and 11 ms respectively. When MFBs is directly coupled with a CMs the Vm switches from -49 to -69 mV, resulting in an upper-shift of the IV relationship. Those results are crucial for understanding the range by which the conductive patch might sustain bioelectricity. We then measured the gap junctional conductance (GJ) in i) non transfected MFB-CM in ii) transfected (Halo)MFB-CM when the light is off and iii) transfected (Halo)MFB-CM when the light is on, via double patch-clamp technique. Apart for the changing in resting Vm as above mentioned we did not find any significant difference in GJ at different

length of cell-to-cell contact measured by SICM, suggesting that such intervention does not modify (as expected) an AP independent parameters like GJ.

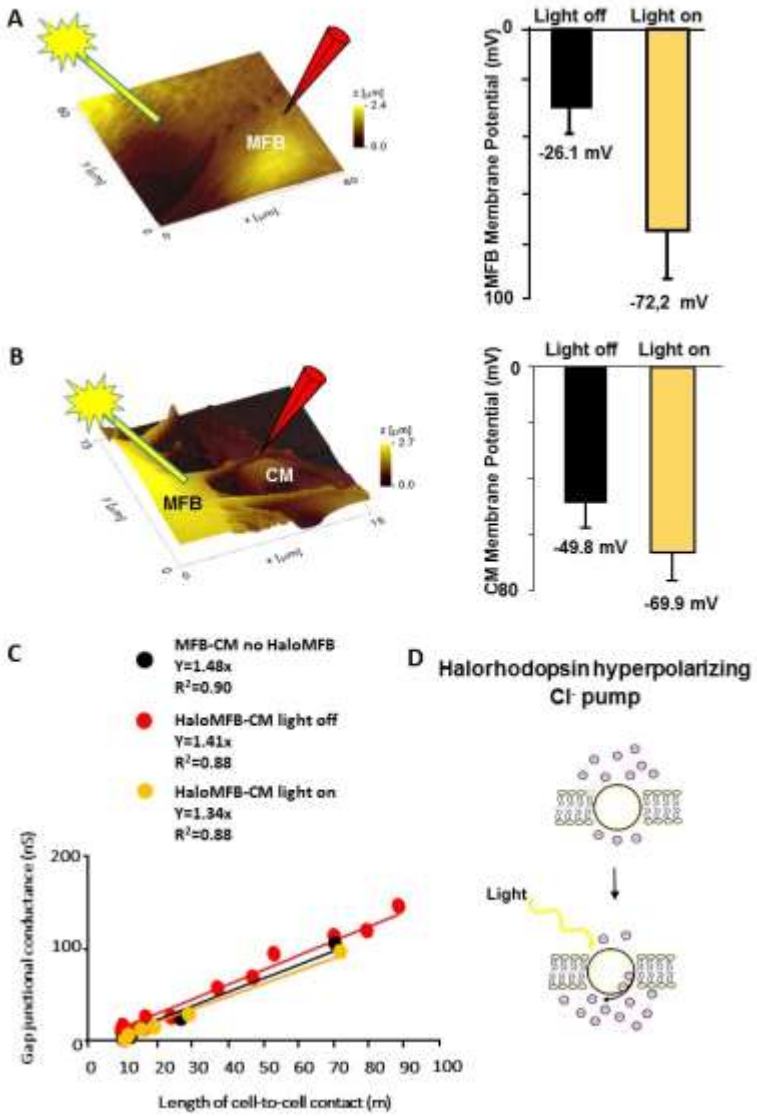


**Fig.6**. Optogenetic control of CM-MFB coupling. A: SICM topographical images of transfected MFB, expressing HalorhodopsinCl$^-$ channels and correspondent MFB membrane potential w/wo illumination; B: coupling between CM and transfected MFB and correspondent membrane potential measured in the CM with/without illumination. C. Gap junctional conductance

measured by double-patch clamp technique in the three conditions: no transfection – transfection light off and transfection light on. D: Schematic representation of halorhodopsin$Cl^-$ pump function.

### 5.3.2 Transmitted impulse propagation between two separate cardiomyocytes via SiC nanowires

We then perform the crucial preliminary test in order to recognise the possibility to transmit bioelectricity from one excitable cell to another via SiC nanowires. We synthetized 300 µg of SiC nanowires as described above and mixed with 100 µl solution containing 0.5 µg of collagen (Human Placenta IV). We prepared 22 mm coverslips with a 4 mm central area coated with collagen-SIC solution and $1.5x10^3$ $mm^2$ HL-1cells were seeded. After 48 hours we stained the cells with voltage sensitive dye (Di-8-ANEPPS) and measured impulse propagation optically at high temporal resolution (2 KHz) at 36 ºC (Fig.7). We found that several separated cells in the field of view were beating synchronously with a minimal delay (~1.2 ms) for an action potential propagated over a distance of 410 µm resulting in a conduction velocity of ~330 mm/sec, higher than a physiological conduction velocity measured in this cell line (~80 mm/sec). This experiment indicates that SiC nanowires, once engulfed in the cell, are capable to conduct and propagate the impulse over a distance higher than the 320 µm (maximal distance for the passive electrotonus sustained by MFBs), resolving any conduction block occurring beyond this limit.

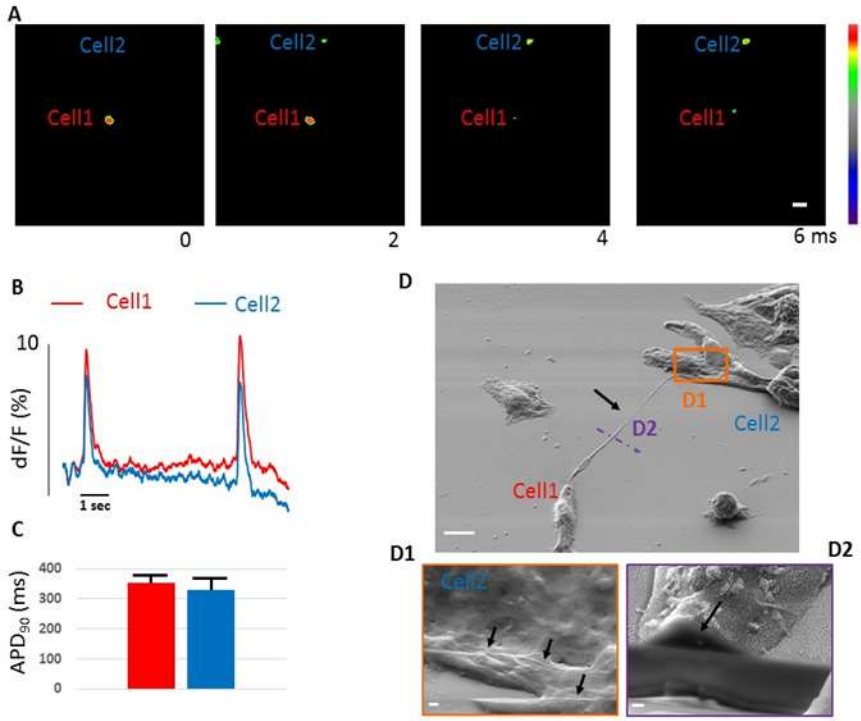


**Fig.7**. Transmission of cardiac bioelectricity over distance by SiC nanowires. A. Optical fluorescence recording of a spontaneous action potential activated from Cell 1 (center of the field of view) and propagated to Cell 2 (upper-center of the fielf of view) with a delay of 1.2 ms. Bar 100 µm. B. Optical action potential traces recorded in Cell 1 and in Cell 2. To note both traces including two action potentials are superimposed indicating a real transmission of bioelectricty from Cell 1 to Cell 2. C. Action potential duration calculate at 90% of repolarization time for ten propagated action potentials between the two cells. D. Scanning electron microscopy (SEM) images of the nanowire that puts in communication the two cell. Arrow indicate the nanowire coated by cell membrane. Bar: 50 µm. D1. SEM zoom image of the orange rectangular area in D showing the presence of nanowires engulfed from the cell2 (arrows). Lilac dashed bar indicate a section (fig. D2) made by focused ion beam technology. Bar: 200 nm. D2. Focused ion beam microscopy show here the sagittal section of the tubule where the edge of a nanowire is visible (arrow). Bar: 100 nm.

### 5.3.3 Resolving conduction block in in-vitro engineered infarcted cardiac tissue

Previous studies in heart transplanted patients have shown that electrical activity between recipient and donor tissue can undergo synchronization even though they are separated by scar tissue[22]. This raised the question whether MFBs in the scar might possibly serve as electrical conductors between donor and recipient cardiac tissue. We have answered this question by constructing a simplified model of the situation of the transplanted heart which consisted of strands of cardiomyocytes being interrupted over defined distances by fibroblasts[23]. These preparations were obtained using a modification of previously developed photolithographic techniques[24]. Impulse propagation characteristics in these model preparations were assessed using voltage sensitive dyes in conjunction with a custom developed optical recording setup. Using this experimental system, we showed that fibroblasts of cardiac origin are able to synchronize electrical activity between remote areas of cardiac tissue for distances up to 320 µm[23]. With increasing distance, synchronization along fibroblasts was increasingly delayed by up to ~ 70 ms, thus resulting in extremely slow local 'conduction velocities' and, accordingly, in highly discontinuous conduction. To note, electrical synchronization was also supported by Cx43 transfected HeLa cells (but not by communication deficient HeLa wild-type cells) indicating that not the cell type per se but its ability to establish heterocellular gap junctional coupling was essential for non-excitable cells to support impulse transmission.

Based on this premises and by keeping in mind our final aim, i.e. resolving conduction block and arrhythmias, we tested the hypothesis if a simple injection of well-polarized cells (HL-1) onto the MFBs area may be beneficial in terms of resolving conduction block and ectopic activity. We employed preparations consisting of 4250 x 1200 µm neonatal CMs monolayer strands

interrupted by a gap filled by cardiac MFBs mixed with 30% of HL-1 cardiomyocytes cell line. The total length of the gap was bigger than 320 µm (~ 2 mm) in order to be sure that the propagation encountered in the gap can be sustained by the HL-1-MFB coupling (Fig.8). We paid attention in controlling that HL-1 cells interact only with MFBs and not with CMs. As expected MFB gaps block the conduction in 90-100% of cases when origin of electrical activity is elicited (by stimulation) at the left edges of the strands (Fig.8C, red bar). Moreover, the coupling between CMs and MFBs elicit spontaneous ectopic activity at the borderzones level (75% of cases, Fig. 7C, black bar). Intriguingly, the conduction block is drastically reduced (40% of cases, Fig 8F red bar) when MFBs are 'contaminated' with HL-1 with a significant delay (124 ms in this example). Such delays can increase the chance of the activation started from the borderzone, which is still in the range of 60-70% of cases (Fig. 8F, black bar). Once again, these results proposed that a given cell therapy (using well-polarized cells) designed to covering or injecting cells in the MI can be beneficial in reduction the occurrence of conduction block but, because does not completely overcome the depolarization exerted by MFBs, the propagation can be drammaticallyslowered and cannot limit the likelihood of the ectopic activity exerted by the borderzones. To note, we measured a delay in the range of few milliseconds (not hundreds) when the propagation are sustained by the SiC-NWs over 410 µm distance (cf. Fig.7).

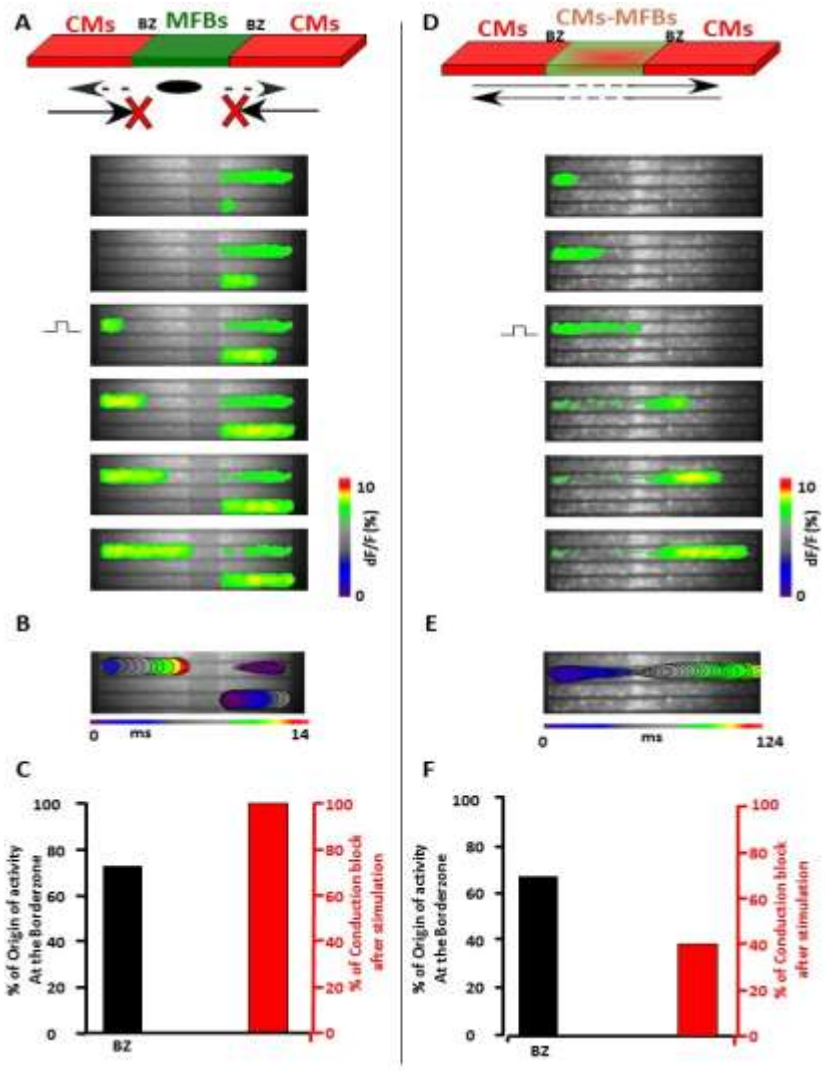


**Fig.6** Cardiac impulse conduction in engineered defnied strands. A. Top. Schematic representation of the engineered strands of CMs interrupted by a MFBs insertion. L: lateral end; C: central end. Bottom. Stimulated optical impulse propagation starting from lateral ends collides and block on MFBs area (translucent). B. Color-coded isochrones maps (2 ms inter-distance) of spontaneous activated strands of CMs showing conduction block (blue to red) in proximity of MFBs area. C. Percent of origin of activity and conduction block at the three impulse initiation sites. D. Same as A for a gap of MFBs with 30% density of HL-1 cells seeded on top. E. Resolved conduction block propagated from a lateral end (blue to yellow) with a sensible delay. F. Same as C showing the reduction in percentage of conduction blocks.

## 5.4 Summary

In this chapter we showed the second application of our NWs, the Conductive epicardial Patch(CEP). The device allows to re- establish electrical conduction across infarct area. CEP is based on silicon-carbide conductive nanowires embedded in an epicardial-interacting patch.

As “proof of concept” we demonstrated to be able to re-established impulse propagation using SiC nanowires, in in-vitro in engineered infarcted cardiac tissue, made by neonatal rat ventricular cardiomyocytes and myofibroblasts.

In the near future we will test, in-vivo, SiC nanowire in infarcted rat with the aim to re-establish the conduction in the myocardial infarcted tissue.

Bybliography


[1] Anon WHO | World Health Organization

[2] O'Gara P T, Kushner F G, Ascheim D D, Casey D E, Chung M K, de Lemos J A, Ettinger S M, Fang J C, Fesmire F M, Franklin B A, Granger C B, Krumholz H M, Linderbaum J A, Morrow D A, Newby L K, Ornato J P, Ou N, Radford M J, Tamis-Holland J E, Tommaso C L, Tracy C M, Woo Y J and Zhao D X 2013 2013 ACCF/AHA Guideline for the Management of ST-Elevation Myocardial Infarction: A Report of the American College of Cardiology Foundation/American Heart Association Task Force on Practice Guidelines *Circulation***127** e362–425

[3] Rich M W and Shen W-K 2012 *Cardiac Rhythm Disorders in Older Adults, An Issue of Clinics in Geriatric Medicine* vol 14 (Elsevier Health Sciences)

[4] Cohn J N, Ferrari R and Sharpe N 2000 Cardiac remodeling--concepts and clinical implications: a consensus paper from an international forum on cardiac remodeling. Behalf of an International Forum on Cardiac Remodeling. *J. Am. Coll. Cardiol.***35** 569–82

[5] Swynghedauw B 1999 Molecular mechanisms of myocardial remodeling. *Physiol. Rev.***79** 215–62

[6] Wasson S, Reddy H K and Dohrmann M L 2004 Current perspectives of electrical remodeling and its therapeutic implications. *J. Cardiovasc. Pharmacol. Ther.***9** 129–44

[7] Peters N S and Wit A L 1998 Myocardial architecture and ventricular arrhythmogenesis. *Circulation***97** 1746–54

[8] LeGrice I J, Smaill B H, Chai L Z, Edgar S G, Gavin J B and Hunter P J 1995 Laminar structure of the heart: ventricular myocyte arrangement and connective tissue architecture in the dog. *Am. J. Physiol.***269** H571–82

[9] Spach M S and Dolber P C 1986 Relating extracellular potentials and their derivatives to anisotropic propagation at a microscopic level in human cardiac muscle. Evidence for electrical uncoupling of side-to-side fiber connections with increasing age. *Circ. Res.***58** 356–71

[10] de Bakker J M, van Capelle F J, Janse M J, Tasseron S, Vermeulen J T, de Jonge N and Lahpor J R 1993 Slow conduction in the infarcted human heart. "Zigzag" course of activation. *Circulation***88** 915–26

[11] Adler C P, Ringlage W P and Böhm N 1981 [DNA content and cell number in heart and liver of children. Comparable biochemical,

cytophotometric and histological investigations (author's transl)]. *Pathol. Res. Pract.***172** 25–41

[12] McAnulty R J and Laurent G J 1987 Collagen synthesis and degradation in vivo. Evidence for rapid rates of collagen turnover with extensive degradation of newly synthesized collagen in tissues of the adult rat. *Coll. Relat. Res.***7** 93–104

[13] Weber K T 1997 Extracellular matrix remodeling in heart failure: a role for de novo angiotensin II generation. *Circulation***96** 4065–82

[14] Mundth E D 1972 Rupture of the heart complicating myocardial infarction. *Circulation***46** 427–9

[15] Sanna V, Pala N and Sechi M 2014 Targeted therapy using nanotechnology: focus on cancer. *Int. J. Nanomedicine***9** 467–83

[16] Ferrari M 2005 Cancer nanotechnology: opportunities and challenges. *Nat. Rev. Cancer***5** 161–71

[17] Oliveros A, Guiseppi-Elie A and Saddow S E 2013 Silicon carbide: a versatile material for biosensor applications. *Biomed. Microdevices***15** 353–68

[18] Bogart L K, Pourroy G, Murphy C J, Puntes V, Pellegrino T, Rosenblum D, Peer D and Lévy R 2014 Nanoparticles for imaging, sensing, and therapeutic intervention. *ACS Nano***8** 3107–22

[19] Sapir Y, Polyak B and Cohen S 2014 Cardiac tissue engineering in magnetically actuated scaffolds. *Nanotechnology***25** 014009

[20] Shevach M, Fleischer S, Shapira A and Dvir T 2014 Gold nanoparticle-decellularized matrix hybrids for cardiac tissue engineering. *Nano Lett.***14** 5792–6

[21] Cingolani E, Ionta V, Cheng K, Giacomello A, Cho H C and Marbán E 2014 Engineered electrical conduction tract restores conduction in complete heart block: from in vitro to in vivo proof of concept. *J. Am. Coll. Cardiol.***64** 2575–85

[22] Lefroy D C, Fang J C, Stevenson L W, Hartley L H, Friedman P L and Stevenson W G 1998 Recipient-to-donor atrioatrial conduction after orthotopic heart transplantation: surface electrocardiographic features and estimated prevalence. *Am. J. Cardiol.***82** 444–50

[23] Gaudesius G, Miragoli M, Thomas S P and Rohr S 2003 Coupling of cardiac electrical activity over extended distances by fibroblasts of cardiac origin. *Circ. Res.***93** 421–8

[24] Jacobs A K, Antman E M, Faxon D P, Gregory T and Solis P 2007

Development of systems of care for ST-elevation myocardial infarction patients: executive summary. *Circulation***116** 217–30

# CHAPTER

# 6

# Summary and Conclusive Considerations

Nanomedicine is a new branch of medicine that offers new opportunities in field as imaging, drug delivery, therapy technic, tissue repair and bioengineering [1],[2]. In this thesis we examined the concept of nanomedicine, starting with its definition up to applications. The main aim was to evaluate the potentiality of Si(O,C) NWs and to open the way to new and promising applications in biomedical field.

In the first part we showed the potentiality of nanomedicine, focusing on 1D nanostructures with particular emphasis on Si(O,C)NWs.[3] The Si(O,C) NWs are biocompatible and suitable to be embedded in nano and micro biomedical and electromedical device. Combining Silicon with Oxygen and Carbon we obtained different characteristics and properties, which make the materials suitable to different applications, as tissue regeneration or electromedical implantable devices. Furthermore, the dimensions of NWs, comparable with extracellular matrix, can biomime the biological systems and promote the integration with the body.

We evaluated the cytocompatibility and the effect of interaction between blood and NWs in view of future applications. The SiC/$SiO_2$ NWs, grown by

CVD system, were evaluated both on substrate, as a platform, and detached from substrate, as a "powder". We demonstrated that the NWs (detached) are not cytotoxic below to 50μg/ml, the viability, at short (24h) and long time (10 days) were not compromised and the cell cycle of life was maintained. The Up-Take was evaluated by side scattering and confirmed by TEM, and it demonstrated that the NWs were internalized by micro-pinocytosis and compartmentalized in vacuoles. [4]

The cytocompatibility evaluation of $SiC/SiO_2$ NWs platform was performed following the ISO 10993-5 and the blood-materials interaction was conducted following the ISO 10993-4. The experiments demonstrated that the NWs were not cytotoxic, but the kinetic adhesion and proliferation was slowed. Indeed the focal adhesion, essential for cells adhesion and proliferation, is dependent on the dimension of nanostructure and on the gaps between two nanostructures.

We obtained analogous cytotoxic results with $SiO_xC_y$ NWs platform. The $SiO_xC_y$NWs are not cytotoxic and the kinetics adhesion and proliferation were slowed in the first 48h, but increased after 96 h. After this time, the SEM showed that the cells colonize the platform and reorganize the substrate to create a better environment to grow, promoting the focal adhesion.

The blood compounds interaction were evaluated by platelets activation, following the ISO 10993-4. Both $SiC/SiO_2$NWs and $SiO_xC_y$ NWs triggered the platelets activation and the inflammatory cascade. These characteristic are very interesting because can demonstrate that these NWs are suitable to scaffold for tissue engineering and regenerative medicine.

Instead, SiC NWs were studied in view to use they as materials for electromedical devices. Similarly as $SiC/SiO_2$ NWs, we evaluated the NWs with and without substrate. The NWs, detached, are cytocompatible at concentrations below 50μg/ml. The cells lifecycle was maintained and damage

from oxidative stress were not detected. The study of Up-Take showed that the NWs were not internalized. The NWs platform were not cytotoxic, in according to ISO 10993-5. The blood compounds interaction, in according to ISO 10993-4, showed an interesting results: SiC NWs are hemocompatible and therefore suitable to electromedical devices, both for cardiac and for neuronal fields.

In the second part of this thesis we focuses on applications, and we showed two different applications of the Si-based NWs and SiC based NWs.

Several patients suffer from retinal degeneration diseases as age-related macular degeneration and retinitis pigmentosa. These diseases have limited treatment options but need specific attention from governmental agencies, leading to high personal and public resources costs. We proposed a subretinal device to partially restore the sight to these patients.[5]

The subretinal implants (sMD) are silicon NWs based. The sMD were developed based on a well-established photovoltaic technology[6] and adapting this know-how to the prosthetic field.The system works thanks to the inorganic/organic materials band alignment: the highest occupied molecular orbital of organic semiconductor, i.e. poly(3,4-ethylenedioxythiophene):poly(styrene sulfonate)(PEDOT:PSS), is positioned to inject holes into the electrolyte and hence into neuronal cells. The lowest unoccupied molecular orbital of organic semiconductor is well above the Fermi level of the n-type NWs, and then electron collection occurs efficiently at the silicon interface.

In the chapter 4 we showed the feasibility and the concepts on which is based the subretinal device. The idea is supported by preliminary results. Only the permissiveness of hippocampal neurons on PEDOT:PSS was evaluated, because only this material will be in contact with the neurons.

The results demonstrated that the PEDOT:PSS are neurocompatible. To

evaluated the permissiveness, different compounds of PEDPT:PSS solution were varied. We demonstrated that the percentage of ethylene glycol (EG) change both the characteristic of polymer that the permissiveness. Long term hippocampal cultures on PEDOT:PSS 3% EG were functionally healthy, although the amount of glial cells was reduced.[7]

We showed the potentiality of sMD and we demonstrated that it is an promising devices to solve the degenerative retinal diseases retinitis pigmentosa.

The chapter 5 was focused on SiC based cardiac electrical patches suitable to myocardic infarction. The myocardial infarction is a disease that kills 7.3 million of persons worldwide. To solve this problem we propose a new nanodevice that allows to re-establish electrical conduction across infarct area. The device is based on silicon-carbide conductive nanowires embedded in an epicardial-interacting patch. The chapter showed the feasibility and the concepts on which is based the patch. The idea behind this device is to shape a conductive epicardial patch based on Teflon (polytetrafluoroethylene), already used in cardiovascular field (as stent or graft) that include SiC nanowires. This patch will be positioned on infarcted area, by-passing this zone and re-establishing the electrical conduction. Preliminary results showed the patch feasibility. We showed that several separated cells in the field of view were beating synchronously with a minimal delay (~1.2 ms) for an action potential propagated over a distance of 410 µm, resulting in a conduction velocity of ~330 mm/sec. This experiment indicates that SiC nanowires, once engulfed in the cell, are capable to conduct and propagate the impulse over a distance higher than the 320 µm, resolving any conduction block occurring beyond.

**Bibliography**


[1] H. Liu and T. J. Webster, “Nanomedicine for implants: A review of studies and necessary experimental tools.,” *Biomaterials*, vol. 28, no. 2, pp. 354–369, Oct. 2006.

[2] J. He, X. Qi, Y. Miao, H.-L. Wu, N. He, and J.-J. Zhu, “Application of smart nanostructures in medicine.,” *Nanomedicine (Lond).*, vol. 5, no. 7, pp. 1129–38, Sep. 2010.

[3] Y. Piao, A. Burns, J. Kim, U. Wiesner, and T. Hyeon, “Designed Fabrication of Silica-Based Nanostructured Particle Systems for Nanomedicine Applications,” *Adv. Funct. Mater.*, vol. 18, no. 23, pp. 3745–3758, 2008.

[4] A. Cacchioli, F. Ravanetti, R. Alinovi, S. Pinelli, F. Rossi, M. Negri, E. Bedogni, M. Campanini, M. Galetti, M. Goldoni, P. Lagonegro, R. Alfieri, F. Bigi, and G. Salviati, “Cytocompatibility and cellular internalization mechanisms of SiC/SiO 2 nanowires,” *Nano Lett.*, vol. 14, no. 8, pp. 4368–4375, 2014.

[5] J. M. Ong and L. da Cruz, “A review and update on the current status of stem cell therapy and the retina.,” *Br. Med. Bull.*, vol. 102, pp. 133–46, Jun. 2012.

[6] D. M. Nanditha, M. Dissanayake, R. A. Hatton, R. J. Curry, and S. R. P. Silva, “Operation of a reversed pentacene-fullerene discrete heterojunction photovoltaic device,” *Appl. Phys. Lett.*, vol. 90, no. 11, p. 113505, Mar. 2007.

[7] G. S. and L. B. Giada Cellot, Paola Lagonegro, Giuseppe Tarabella, Denis Scaini, Filippo Fabbri, Salvatore Iannotta, Maurizio Prato, “PEDOT:PSS interfaces support the development of neuronal synaptic networks with reduced neuroglia response in vitro,” *Front. Neurosci.*, 2016.